

Time-fractional Analysis of Flow Patterns during Refrigerant Condensation



Eugene van Rooyen

Department of Mechanical and Aeronautical Engineering

University of Pretoria

Supervised by Prof. Dr L. Liebenberg

Co-supervised by Prof. Dr J.P. Meyer

A dissertation submitted in partial fulfilment for the degree of

Masters in Engineering

March 2007

”Men are nearly always willing to believe what they wish.”
Julius Caesar

Abstract

The conceptual design and basic layout of a modular refrigerant test system capable of flow condensation and evaporation were performed. The purpose of this study was the investigation of flow patterns during refrigerant condensation in intermittent flow in order to improve the prediction models. An objective flow pattern descriptor was developed to identify and describe transitions in flow regimes. The methods developed and utilised in this study were used to develop a time-fractional map of the intermittent flow regime. The time-fractions are statistical averages of gravity dominated and shear dominated flows occurring in intermittent flow.

Acknowledgements

And I would like to acknowledge the contribution of my supervisors

Professor Leon Liebenberg and
Professor Josua Meyer,

as well as,

Juan Kotze
Marcel Christians
Jonathan Olivier
Dewald Pieterse
Robbie Arrow
Philip de Vos
Danie Gouws

The Department of Mechanical and Aeronautical Engineering and all other members of staff for the years of mentorship that led me this far.

Contents

Abstract	ii
Acknowledgements	iii
List of Figures	ix
List of Tables	xiii
Nomenclature	xiv
1 Introduction	1
1.1 Background	1
1.2 Justification for the study	3
1.3 Goal of study	4
1.4 Structure of this dissertation	5
2 Literature study	6
2.1 Introduction	6
2.2 Refrigerant properties	6
2.3 Flow condensation	7
2.3.1 Modes of condensation	8
2.4 Condensate flow in tubes	9
2.4.1 Flow regimes during condensation	9
2.4.2 Methods of observation	15
2.4.3 Flow map history	18
2.4.4 Contemporary flow condensation maps	20
2.4.4.1 Baker map, 1954	20
2.4.4.2 Mandhane map, 1974	21
2.4.4.3 Breber map, 1980	22
2.4.4.4 Taitel and Dukler map, 1976	24

2.4.4.5	Soliman map, 1982	25
2.4.4.6	Weisman et al. map, 1979	28
2.4.4.7	Dobson and Chato map	28
2.4.4.8	Sardesai et al. map, 1981	30
2.4.4.9	Cavallini et al. map, 2002	31
2.4.4.10	Cavallini et al. map, 2006	31
2.4.4.11	Time-fraction methods	32
2.4.5	El Hajal et al. map, 2003	34
2.4.6	Comparison of maps	38
2.4.6.1	Conclusion	43
2.5	Transitions	44
2.5.1	Effect of variables on transitions	45
2.6	Time-Frequency analysis	47
2.7	Mathematical background	49
2.8	Conclusion	51
3	Experimental Set-up	52
3.1	Introduction	52
3.2	Test Facility	53
3.2.1	Refrigerant cycle	53
3.2.2	Water cycle	58
3.2.3	Instrumentation and data acquisition	60
3.3	Labview and the Labview program	64
3.4	Matlab script	70
3.4.1	Thermodynamic properties	70
3.4.2	Energy balance	74
3.4.3	Thome flow map	75
3.5	Control methodology	75
3.5.1	Mass flux control	76
3.5.2	Test line pressure control	76
3.5.3	Test inlet and outlet vapour quality control	78
3.6	Sensotec FP2000 ratiometric measurements	78
3.7	Experimental Procedure	79

3.8	Test section design	82
3.9	Conclusion	87
4	Smooth tube air-water flow patterns	88
4.1	Analysis methodology	88
4.1.1	Introduction	88
4.1.2	Classical heat transfer modes	88
4.1.3	The intermittent flow regime and the prevailing heat transfer mode	89
4.1.4	Time-fraction and probability	90
4.1.5	Analysis	92
4.2	The analysis procedure	94
4.3	Classification of flow regimes	95
4.4	Preliminary air-water testing	97
4.4.1	Experimental facility	97
4.4.2	Results	99
4.4.2.1	Time-frequency	99
4.4.2.2	Time-fraction map	100
4.4.3	Pressure and void fraction	107
4.5	Conclusion	107
5	Smooth tube refrigerant flow patterns	108
5.1	Refrigerant experimental test matrix	108
5.2	Refrigerant in smooth tubes	110
5.2.1	Vision	111
5.2.2	Experimental data capture and data reduction	111
5.2.3	Vision results	113
5.2.4	Time-fractional results	122
5.3	Pressure signal and void fraction	127
5.3.1	Pressure signal	127
5.3.2	Void fraction	130
5.3.3	Conclusion	132
5.4	Results on correlations	133
5.5	Conclusion of this chapter	135

6	Conclusions	137
6.1	Introduction	137
6.2	Consolidation of work done	137
6.3	Final conclusion and future suggestions	139
	References	149
A	Uncertainty analysis	150
A.1	Introduction	150
A.2	Generalized uncertainty analysis methods	150
A.3	Uncertainty in temperature measurements	152
A.4	Refrigerant mass flow rate uncertainty	153
A.4.1	Mass flux uncertainty	153
A.5	Water mass flow rates uncertainty	154
A.6	Pressure measurement uncertainty	154
A.7	REFPROP uncertainty analysis	154
A.8	Temperature difference uncertainty	156
A.9	Uncertainty in measurement of tube diameters	156
A.10	Uncertainty in measurement of heat exchanger length	156
A.11	Uncertainty in measurement of surface area	156
A.12	Uncertainty in the value of thermal conductivity of the copper tubing	157
A.13	Heat balance, Refrigerant side	157
A.14	Heat balance uncertainty, water side	158
A.15	Average heat transfer uncertainty	159
A.16	Log mean temperature difference uncertainty analysis	159
A.17	Inlet and outlet vapor quality uncertainty analysis	160
A.17.1	Inlet vapor quality uncertainty	160
A.18	Overall heat transfer coefficient uncertainty analysis	161
A.19	Inner tube heat transfer coefficient	162
A.20	Frequency detection via high-speed camera	162
A.21	Uncertainty Results	162
A.22	Conclusion	165

B Programs	166
B.1 Main system control	166
B.2 LabView videos capture program	169
B.3 Video analysis	170
C Raw data	172

List of Figures

1.1	Results presented on the state of ozone depleting substances in the atmosphere with predictions of future levels (GAW, 2006)	3
2.1	Flow regimes for condensation at high and low mass fluxes, adapted from Collier and Thome (1994). Flow direction from left to right	11
2.2	Baker flow map for air-water at standard conditions	21
2.3	Mandhane map with Dobson (1994) modifications	22
2.4	Breber <i>et al.</i> (1980) map	23
2.5	Taitel and Dukler map (1976) used by Dobson (1994)	26
2.6	Taitel and Dukler map on combined axes (Bukasa <i>et al.</i> , 2004)	26
2.7	Soliman (1982) map	27
2.8	Comparison of observations by Weisman <i>et al.</i> (1979) flow regime map to Mandhane <i>et al.</i> (1974)	29
2.9	Sardesai <i>et al.</i> (1981) heat transfer guide	30
2.10	ΔT -dependent and ΔT -independent transition	31
2.11	Time-fractional data for several mass flows (Niño <i>et al.</i> , 2002)	32
2.12	The El Hajal <i>et al.</i> (2003) condensation flow map	38
2.13	Void fraction geometry for stratified flow (El Hajal <i>et al.</i> , 2003)	38
2.14	Other void fraction geometries (Thome <i>et al.</i> , 2003)	39
2.15	Principle of wavelet analysis	50
3.1	Top view of the two-phase flow experimental setup	53
3.2	Physical refrigerant pipe connection schematic	54
3.3	Rear view of the refrigerant bench	55
3.4	Control equipment on the water control bench	59

3.5	Control bench water pipe layout	61
3.6	Water cycle layout on the refrigerant test bench	62
3.7	Diagram of void fraction sensor provided by UGent	64
3.8	Front panel of the LabView program	67
3.9	Refrigerant pre-condenser outlet possibilities	72
3.10	Schematic of the system cycle	77
3.11	Pressure sensor and thermocouple placement at the inlet and outlet of the test section (1.: Top position, 2.: Side position, 3.: Bottom position)	80
3.12	Test Section model	84
3.13	Cutaway view of the sight glass assembly	85
3.14	Inlet and outlet exchanger construction	86
4.1	Stratified Flow?	90
4.2	Slug Flow?	90
4.3	Intermittent flow - between slugs	91
4.4	Schematic of air-water test loop	98
4.5	Baker map with test region	99
4.6	Vision based PSD of air-water flow for $G_{air} = 5 kg/m^2s$ and a total mass flux of $250 kg/m^2s$	101
4.7	Vision based time-frequency analysis of air-water flow for $G_{air} =$ $5 kg/m^2s$ and a total mass flux of $250 kg/m^2s$	101
4.8	Vision based PSD of air-water flow for $G_{air} = 12 kg/m^2s$ and a total mass flux of $250 kg/m^2s$	102
4.9	Vision based time-frequency analysis of air-water flow for $G_{air} =$ $12 kg/m^2s$ and a total mass flux of $250 kg/m^2s$	102
4.10	Vision based PSD of air-water flow for $G_{air} = 17 kg/m^2s$ and a total mass flux of $250 kg/m^2s$	103
4.11	Vision based time-frequency analysis of air-water flow for $G_{air} =$ $17 kg/m^2s$ and a total mass flux of $250 kg/m^2s$	103
4.12	Separate plots of test points per air mass flux with time-fraction functions	105

4.13	Function predicting the fractional time of annular flow at various total mass flows, for air-water flow	106
4.14	Time-fraction of gravity-dominated flow found during testing of air-water flow	106
5.1	Experimental test points for R-22 condensing at 40°C	109
5.2	Intermittent flow at $G = 250 \text{ kg/m}^2\text{s}$	114
5.3	Intermittent flow at $G = 250 \text{ kg/m}^2\text{s}$ with a periodic wave passing	114
5.4	Intermittent flow at $G = 250 \text{ kg/m}^2\text{s}$ with a slug and entrained bubbles	114
5.5	Intermittent flow at $G = 400 \text{ kg/m}^2\text{s}$	115
5.6	Intensity PSD during condensation at a mass flux of $250 \text{ kg/m}^2\text{s}$ and a vapour quality of 0.15	116
5.7	Time-frequency analysis of condensing refrigerant at $G = 250 \text{ kg/m}^2\text{s}$ and $x = 0.15$	116
5.8	Intensity PSD during condensation at a mass flux of $300 \text{ kg/m}^2\text{s}$ and a vapour quality of 0.28	117
5.9	Time-frequency analysis of condensing refrigerant at $G = 300 \text{ kg/m}^2\text{s}$ and $x = 0.28$	117
5.10	Intensity PSD during condensation at a mass flux of $300 \text{ kg/m}^2\text{s}$ and a vapour quality of 0.40	119
5.11	Time-frequency analysis of condensing refrigerant at $G = 300 \text{ kg/m}^2\text{s}$ and $x = 0.40$	119
5.12	Intensity PSD during condensation at a mass flux of $300 \text{ kg/m}^2\text{s}$ and a vapour quality of 0.45	120
5.13	Time-frequency analysis of condensing refrigerant at $G = 300 \text{ kg/m}^2\text{s}$ and $x = 0.45$	120
5.14	Intensity PSD during condensation at a mass flux of $300 \text{ kg/m}^2\text{s}$ and a vapour quality of 0.69	121
5.15	Time-frequency analysis of condensing refrigerant at $G = 300 \text{ kg/m}^2\text{s}$ and $x = 0.69$	121
5.16	The analysis results for all mass fluxes tested with R-22	124
5.17	Combined time-fractional results for condensing R-22 at 40°C	125

5.18	Time-fractional map superimposed on a El Hajal <i>et al.</i> (2003) flow pattern map for condensing refrigerant	126
5.19	Annular flow pressure PSD during condensation at a vapour quality of 0.65	128
5.20	Intermittent flow pressure PSD during condensation at a vapour quality of 0.45	128
5.21	Intermittent flow pressure PSD during condensation at a vapour quality of 0.25	129
5.22	Slug flow pressure PSD during condensation at a vapour quality of 0.13	129
5.23	Intermittent flow void fraction PSD during condensation at a vapour quality of 0.20	131
5.24	Intermittent flow void fraction PSD during condensation at a vapour quality of 0.34	131
5.25	Intermittent flow void fraction PSD during condensation at a vapour quality of 0.65	132
5.26	Comparison of experimental heat transfer measurements and the Thome <i>et al.</i> (2003) correlations	133
5.27	Heat transfer measurements after time-fractional correction	134
5.28	The heat transfer correlations used in the time-fractional correction at $G = 350 \text{ kg/m}^2\text{s}$	135
5.29	Results of time-fraction on pressure drop prediction at $G = 400 \text{ kg/m}^2\text{s}$ (Christians-Lupi, 2007)	136
A.1	Comparison of frequencies detected and emitted	163
B.1	Diagram of the processes during every cycle of the control program	167
B.2	Diagram with the sequence of events during a video capture	170
B.3	Diagram of the sequence of programming during a video analysis run	171

List of Tables

2.1	R-22 properties (National Institute of Standards and Technology, 2002)	7
2.2	R-134a properties (National Institute of Standards and Technology, 2002)	8
2.3	Flow regimes during in-tube condensation in horizontal tubes adapted from Dobson and Chato (1998)	12
2.4	Flow pattern criteria	23
2.5	Flow pattern criteria of Taitel and Dukler (1976)	25
2.6	Soliman transition criteria	27
2.7	Weisman transition criteria	28
2.8	Parameter needed for flow pattern determination Kattan <i>et al.</i> (1998a)	35
2.9	Transition criteria by various authors	44
3.1	Equipment utilized by the Labview software backbone in the two-phase experimental setup	65
5.1	Experimental testing criteria	108
5.2	Mean testing point information	109
5.3	Mean testing point information	110
5.4	The time-fraction results for R-22 condensing at 40 °C	123
5.5	Binomial function coefficients for all mass fluxes of condensing refrigerant tested	125
A.1	Experimental uncertainties for condensation heat transfer	163

Nomenclature

Roman Symbols

A Cross sectional area, [m^2]

B_i Bias of i^{th} measurement

c_p Specific heat capacity at constant pressure, [$\frac{J}{kgK}$]

D Diameter, [m]

d Diameter, [m]

Fr Froude number, $= \frac{G^2}{gD_i\rho^2} = \frac{G}{gD_i}$, [-]

F_{td} Modified Froude number of Taitel and Dukler, $= \sqrt{\frac{\rho_g}{\rho_l - \rho_g} \frac{Gx}{\rho_l}} \frac{1}{\sqrt{Dg \cos \varepsilon}}$, [-]

G Mass velocity (flux), [$\frac{kg}{m^2s}$]

g Gravitational acceleration, [$\frac{m}{s^2}$]

Ga Galileo number, $\frac{D^3g}{\nu^2}$ or $\frac{\rho_l(\rho_l - \rho_v g D^3)}{\mu_l^2}$, [-]

H Vertical height, [m]

h Heat transfer coefficient, [$\frac{W}{m^2K}$]

h Specific enthalpy, [$\frac{J}{kg}$]

h_l Height of liquid level, [m]

\tilde{h}_l Dimensionless liquid level height, [$\frac{h_l}{D}$]

h_{lg}	Isobaric latent heat of condensation, [$\frac{J}{kg}$]
h_t	Window function, [-]
j	Phase specific velocity, [$\frac{m}{s}$]
Ja	Refrigerant Jakob number $\frac{h_{fg}}{c_{pl}\Delta T_s}$, [-]
j^*	Dimensionless vapour mass velocity, [m/s]
k	Thermal conductivity, [$\frac{W}{mK}$]
K_{td}	Stratified-to-wavy parameter of Taitel and Dukler
L	Length, [m]
\dot{m}	Mass flow-rate, [$\frac{kg}{s}$]
Nu	Local Nusselt number, $\frac{hD}{k_l}$, [-]
P	Time-frequency matrix, [-]
p	Pressure, [Pa]
p_r	Reduced pressure, $\frac{p}{p_{cr}}$, [-]
Pr	Prandtl number, $\frac{\mu c_p}{k}$, [-]
P_i	Precision of i^{th} measurement
Q	Heat rate, heat transfer, [W]
\dot{q}	Heat flux, [$\frac{W}{m^2}$]
R	Radius, [m]
r	Radial coordinate measured from the tube centerline, [m]
Re	Reynolds number, $\frac{\rho u D}{\mu} = \frac{GD}{\mu}$, [-]
Re_l	Superficial liquid Reynolds Number, $\frac{G(1-x)D}{\mu_l}$, [-]
Re_{lo}	Liquid-only Reynolds numbers, $\frac{GD}{\mu_l}$, [-]

Re_v	Superficial vapour Reynolds Number, $\frac{GxD}{\mu_v}$, [-]
Re_{vo}	Vapour-only Reynolds numbers, $\frac{GD}{\mu_v}$, [-]
R_f	Thermal resistance, [K/W]
s	Time domain signal, [-]
S_i	Dimensionless interfacial area / Unit length in stratified flow, $\frac{S_l}{D}$, [-]
S_i	Interfacial area / Unit length in stratified flow, [m]
S_t	Windowed Fourier transform, [-]
s_t	Non-windowed Fourier transform, [-]
Su_v	Suratnam number = $\frac{\rho_l D_i \sigma}{\mu_l^2}$
T	Temperature, $^{\circ}$
t	Time, [s]
tf	Probabilistic time-fraction, [%]
T_{td}	Intermittent-to-Dispersed Bubble parameter of Taitel and Dukler
U	Overall heat transfer coefficient, $[\frac{W}{m^2 K}]$
u	Liquid velocity, $[\frac{m}{s}]$
v	Specific volume, $[\frac{m^3}{kg}]$
We	Weber number, $\frac{G^2 D_i}{\rho_v \sigma}$, [-]
X	$[(\frac{dp}{dz})_L / (\frac{dp}{dz})_G]^{\frac{1}{2}}$, [-]
x	Vapour quality (or coordinate), [-]
x_{ia}	Transition from annular to intermittent flow, [-]
X_{tt}	Lockhart-Martinelli parameter, = $[\frac{1-x}{x}]^{0.9} [\frac{\rho_g}{\rho_l}]^{0.5} [\frac{\mu_l}{\mu_g}]^{0.1}$, [-]
y	Coordinate normal to tube wall

z Coordinate along tube length (axial)

Greek Symbols

δ Film thickness, [m]

Δ Difference

Δp Pressure drop, [Pa]

ε Void fraction of vapour, [-]

ω Frequency, [Hz]

γ Apex angle, $^{\circ}$

μ Dynamic viscosity, [$kg/m \cdot s$]

ρ Density, $\frac{kg}{m^3}$

ϕ Inclination angle; angle subtended from the top of the tube to the liquid level, $^{\circ}$

Φ Power spectral density transform

σ Surface tension, [$\frac{Ns}{m}$]

θ Stratified angle, $^{\circ}$

ΔT_{lmtd} Log-mean temperature difference, $= \frac{(T_{w,in} - T_{r,sat}) - (T_{w,out} - T_{r,sat})}{\ln \left[\frac{(T_{w,in} - T_{r,sat})}{(T_{w,out} - T_{r,sat})} \right]}$, [-]

ν Kinematic viscosity, [m^2/s]

Subscripts

a average, air

avg average

b bulk condition

$cond$ condensation

<i>cr</i>	critical
δ	edge of condensate layer, partial
<i>f</i>	frictional
<i>g</i>	gas phase, gravity component
<i>h</i>	hydraulic, homogenous
<i>i</i>	inside, interfacial, inlet, inner
<i>in</i>	inlet
<i>l</i>	liquid phase
<i>o</i>	outside
<i>out</i>	outlet
<i>pc in</i>	precondenser inlet
<i>r</i>	at the fin root, reduced, refrigerant
<i>ra</i>	Rouhani-Axelsson
<i>sat, s</i>	saturation
<i>so</i>	Soliman definition
<i>strat</i>	stratified
<i>tot, t</i>	total
<i>v</i>	corresponding to the entire flow as a vapour
<i>w</i>	tube wall or water

Acronyms

<i>A</i>	Annular flow
<i>B</i>	Bubbly flow

<i>CFC</i>	chlorofluorocarbon
<i>EEV</i>	Electronic expansion valve
EF	Enhancement factor (h_m/h_s)
<i>GWP</i>	Global Warming Potential
<i>HCFC</i>	hydrochlorofluorocarbons
<i>I</i>	Intermittent flow
<i>M</i>	Mist flow
NI	National Instruments
<i>ODP</i>	Ozone Depletion Potential
<i>ODS</i>	Ozone Depleting Substance
<i>R134a</i>	1.1.1.2-tetrafluoroethane
<i>R22</i>	chlorodifluoromethane
<i>R407C</i>	23% of R32, 25% of R125 and 52% of R134a
<i>R410A</i>	50% of R32 and 50% of R125
ROI	Region of interest
RTD	Resistance temperature detector
<i>S</i>	Stratified flow
SCXI	Signal Conditioning Extensions for Instrumentation
<i>SW</i>	Stratified-wavy flow
VI	Virtual Instrument

Chapter 1

Introduction

1.1 Background

Energy is one of the most valuable resources on the planet earth. Research on the improvement in the use of energy and energy conversion have become important in many fields of application. In the future conscientious use of energy resources will become more vital for a sustainable existence and thus research in the field of energy utilising systems is invaluable.

From a broad perspective the objective of this dissertation is to investigate the phenomena during refrigerant flow condensation, and thereby to contribute to the knowledge base and improvement in design of energy converting and energy consuming devices like heat exchangers, heat pumps and refrigeration cycles.

Refrigeration devices using a vapour-compression cycle are common in the modern industrial world and include large commercial cooling facilities, building air conditioning, refrigeration of food and fresh produce and industrial processes. The use of air conditioning and refrigeration in the household environment amounts to a large energy demand. Fractional improvements in refrigeration technology will have a beneficial effect on the environment and energy demands. This research is however not only applicable to this field and can be applied in any two-phase flow and heat exchange application. The methods developed can also find application elsewhere in science and engineering.

The protection of the stratospheric ozone layer began in 1985 with the negotiation of the Vienna Convention. The details of this convention is contained in the

Montreal Protocol (UNEP, 2000) which became effective in 1989 and makes provision for the regular review of control measures based on information from the scientific, environmental, technical and economic sectors. According to this agreement a time frame was set up for the phasing out of chlorofluorocarbons (CFC's) and then hydrochlorofluorocarbons HCFC's in both developed and developing countries (AFEAS, 2002). In the years since the protocol became effective various amendments have been made at meetings in London (1990), Copenhagen (1992), Vienna (1995), and Montreal (1997). In general the amendments are set on tightening control of the substances in question and to speed up the phase out thereof (UNEP, 2000). Not all parties to the main Montreal Protocol are parties to these amendments.

The tropospheric abundances of most ozone-depleting substances (ODS), as well as stratospheric chlorine, were stable or decreasing due to actions taken under the Montreal Protocol (Figure 1.1), with the stratospheric abundances showing a time lag due to the time for surface emissions to reach the stratosphere (GAW, 2006). Based on these facts, it was stated that The Montreal Protocol is working, and the ozone-layer depletion from the Protocols controlled substances is expected to begin to ameliorate within the next decade or so.

The Kyoto protocol is another international treaty which calls for the reduction of greenhouse gasses that results in global warming. In 2001 the United States, responsible for a quarter of the global CO_2 emissions, announced that it would abandon the Kyoto Protocol. Despite this other nations continued in order to make the agreement a binding international treaty that came into effect in 2005 after ratification by more than 125 nations.

Due to the phase out of these refrigerants, alternative refrigerants and heat transfer enhancing mechanisms have to be investigated. A parallel development with the above-mentioned issues is the improvement of models and correlations which can be used for the design of refrigerant applications. The challenge is to develop a unified, accurate, flow regime-based heat transfer model. A method of determining the flow regime and additional information on two-phase flows and transition boundaries is necessary for improved models.

1.2 Justification for the study

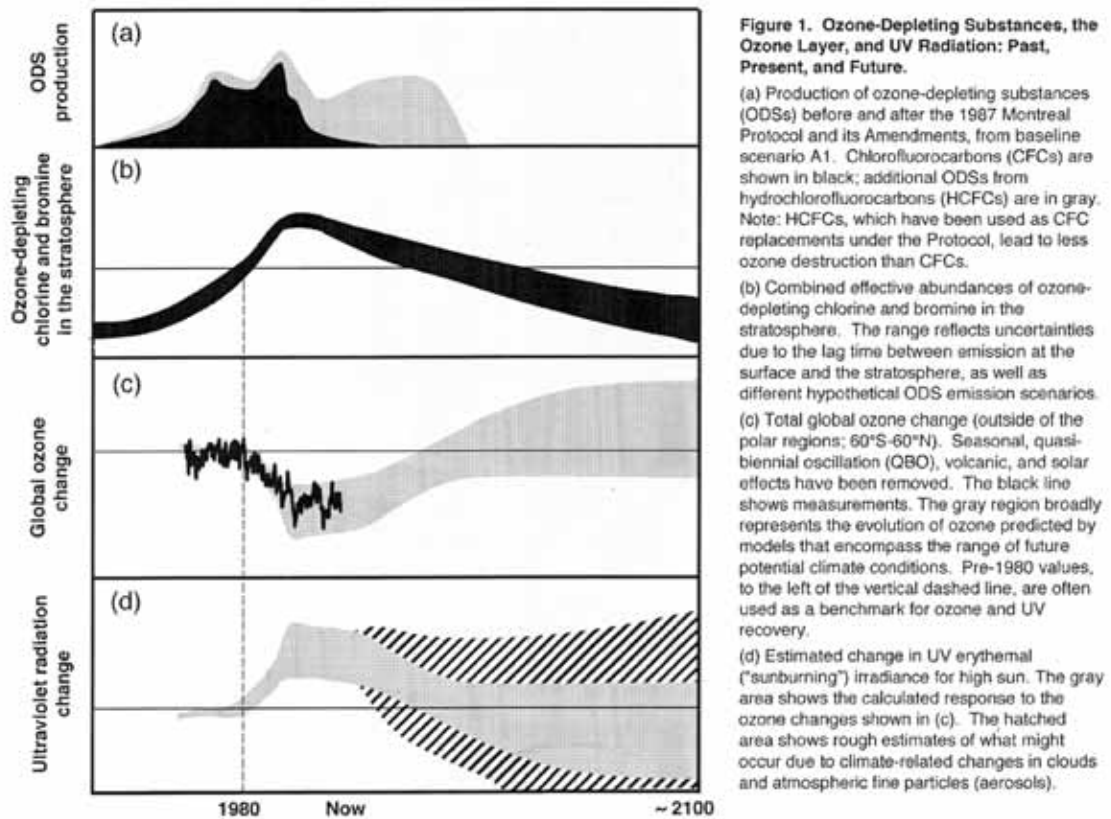


Figure 1.1: Results presented on the state of ozone depleting substances in the atmosphere with predictions of future levels (GAW, 2006)

1.2 Justification for the study

Most modern researchers are in agreement that only heat transfer and pressure drop correlations based on flow regimes are accurate enough for modern design purposes (Cavallini *et al.*, 2006; El Hajal *et al.*, 2003; Liebenberg, 2002).

However, most currently used heat transfer and pressure drop correlations are empirical or semi-empirical in nature and describe reality with relatively poor accuracy. Over the past decade more accurate models based on flow regimes were developed but it is believed that further research is necessary to improve the accuracy and relevance of these correlations. The result would be an improvement in the design and thus the energy efficiency and refrigerant use of many future heat pump and heat transfer applications.

1.3 Goal of study

The aim of this dissertation is the identification of flow patterns (possibly with concomitant and non-invasive methods), to predict flow transition criteria in an objective manner and to add accurate data to the data set available to researchers. This dissertation will result in a new technique of investigating two-phase flow and apply it to the intermittent flow regime. Finally the Thome heat transfer model (Thome *et al.*, 2003) and flow pattern map can be critically evaluated for amendments in the intermittent flow regime by further researchers.

Although a large number of possible mass flux and vapour quality combinations exist, the focus of this study is on low mass fluxes, less than $650 \text{ kg/m}^2\text{s}$. This allows for an extensive investigation in this region and particularly the transitions between stratified-wavy and also the Annular to intermittent flow transition. There is also a general lack of data at low vapour qualities between 5% and 50%, (Thome, 2005).

The methods used to discriminate between flow regimes include using power spectral density (PSD) measurements of the pressure inside the tube, visual observations of the flow through a sight glass, capacitive void fraction signals, and analysis of the video images for a possible objective discriminator. An evaluation of signal analysis techniques, statistical and probabilistic analysis of the signal including the use of neural networks and genetic algorithms.

The El Hajal *et al.* (2003) flow pattern map has been compared to various older and recent versions. This map proved to be a good model for predicting flow regimes and transitions (El Hajal *et al.*, 2003; Liebenberg, 2002). This is true for flow condensation and evaporation and the map has been validated against many data points from various laboratories.

The analysis techniques defined for this study and used for intermittent flow can be used to investigate the transitions of flow patterns in smooth tubes. Further work can include comparisons between smooth tubes and enhanced tubes and complete investigation of the transitions in enhanced tubes. More accurate flow pattern transitions in any type of tube will lead to more accurate models and improved designs.

1.4 Structure of this dissertation

An objective visual method of flow regime description was developed and tested on an air-water system. The system was equipped with a mixing section, pressure transducer, clear perspex or glass tube and a camera. The Baker (1954); Taitel and Dukler (1976); Weisman *et al.* (1979) flow map was used for a description of the flow regime present in air-water. Pressure transducer readings, void fraction reading, visual inspection and analysis of the images were performed.

The visual method of flow pattern analysis was tested in refrigerant flow as method of objective flow regime classification. In particular the subclassification of intermittent flow into two dominant conditions is proposed. The primary goal of this study is investigating the hypothesis stating that the intermittent flow regime constituted of two sub regimes and that the heat transfer and pressure drop model can be improved by taking the sub regimes into account.

Another possible effect that could be investigated by the test setup in use is the hysteresis in the flow pattern occurrence as the vapour quality varies from zero to one and back. Hysteresis in the variation of refrigerant mass flow is difficult and would destabilize the system even though the mass flux control is very accurate. The detection of these effects will be left for future studies.

1.4 Structure of this dissertation

The rest of this document describes the flow of work from the beginning of the study. This includes a literature study of the state-of-the-art in condensation research focussing particularly on flow patterns in Chapter 2. The experimental system used during the study is described and discussed in Chapter 3. The system was conceptualized, instrumented, programmed, tested and validated in cooperation with a fellow master's degree student (Christians-Lupi, 2007). This latter section describes the details and background of the system and its workings.

The experiments done to obtain data and validate the methods are described in Chapter 4. This includes a test matrix, experimental observations, data reduction and flow visualization of air-water experiments. Chapter 5 deals with the data analysis and discussion of refrigerant work, similar to Chapter 4. The difference in results from the methods applied and the final results of the analysis on heat transfer and pressure drop is given. Chapter 6 concludes the study.

Chapter 2

Literature study

2.1 Introduction

This chapter contains relevant information that is available on flow pattern detection and discrimination. A basic description of two-phase flow regimes is given as defined by past research. Methods of flow regime detection and discrimination are discussed. Flow pattern maps from past research to the latest diabatic refrigerant condensation map are discussed and compared.

2.2 Refrigerant properties

The experimental refrigerant that was used during testing and commissioning of the system was R-22. R-22 is currently being phased out but remains an extensively used refrigerant in heat pumps and has been tested by a wide range of facilities. The chemical formula for R-22 is $CHClF_2$, chlorodifluoromethane and its physical properties are given in Table 2.1.

The evaporating temperature range for R-22 is $-40\text{ }^{\circ}\text{C}$ to $5\text{ }^{\circ}\text{C}$ and it is used in applications such as upright freezers, air conditioning, food displays, freezers, cold rooms transport-, commercial- and industrial refrigeration and heat pumps. R-22 is non-flammable and non-toxic but it has an Ozone Depletion Potential (ODP) of 0.05 and a modest Global Warming Potential (GWP) of 1700 (www.engineeringtoolbox.com, 2006). ODP is stated as a percentage of the de-

Table 2.1: R-22 properties (National Institute of Standards and Technology, 2002)

Property	Quantity
Molar mass	86.47 g/mol
Triple point temperature	-157.42 °C
Normal boiling point	-40.81°C
Critical temperature	96.15°C
Critical pressure	4.990 MPa
Critical density	523.8 kg/m ³

pletion potential of R-12 Due to this it is classified as dangerous for the ozone layer and R-22 is currently being phased out.

The replacement refrigerant for R-22 is R-134a and this refrigerant is summarized here for comparison with R-22. The result of using R-134a in a R-22 cycle is a slight loss in efficiency but the environmental benefits are substantial. The chemical formula for R-134a is 1,1,1,2-tetrafluoroethane: CH_2FCF_3 , and the physical properties are given in Table 2.2. R-134a is a long term alternative for the CFC, R-12. R-134a compares well with R-12 in terms of physical and refrigeration properties. The refrigeration effect per swept volume of R-134a is equal to or greater than R-12 down to an evaporating temperature of $-25^\circ C$ and the coefficient of performance is equal or better down to evaporating temperatures of $-20^\circ C$ (Olivier, 2003). R-134a has an ODP of 0 and a GWP of 1300 (www.engineeringtoolbox.com, 2006).

2.3 Flow condensation

Flow condensation occurs when vapour and sub-cooled liquid come into direct contact and mass and heat transfer take place. The most common type of condensation occurs when saturated vapour comes into contact with a cooled surface at a lower temperature. Vapour molecules that come into contact with the surface can condense on it and form a liquid.

Table 2.2: R-134a properties (National Institute of Standards and Technology, 2002)

Property	Quantity
Molar mass	102.03 g/mol
Triple point temperature	-103.3 °C
Normal boiling point	-26.07°C
Critical temperature	101.06°C
Critical pressure	4.059 MPa
Critical density	511.9 kg/m ³

2.3.1 Modes of condensation

There are two types of condensation depending on the condition of the surface, i.e. the temperature or the surface finish. The dominant form of condensation is filmwise condensation, in which a liquid layer covers a surface. This condensation occurs when a thin liquid film (100 – 150 μm thick) continuously collects on the surface (Lienhard and Lienhard, 2005).

If a liquid does not wet the entire surface it forms as discrete droplets on the surface. This is known as dropwise condensation. Drops form in cracks, pits, cavities and irregularities on the surface and may grow and coalesce. Drops may cover up to 90% of the surface and range in size from micrometers to clearly visible droplets. When these drops become large enough for gravity or vapour shear to overcome the adhesive force due to surface tension, a drop can depart from the surface and sweep condensate along allowing for new droplets to form.

During filmwise condensation the heat transfer resistance increases with the film thickness. During dropwise condensation heat transfer occurs through drops of less than 100 μm in diameter and therefore resistance is much lower. Dropwise condensation is therefore preferred and methods are used to stimulate dropwise condensation rather than film condensation. Teflon, waxes and silicones have been used to this effect but after some time the coatings become fouled and oxidized and lose their effect (Lienhard and Lienhard, 2005).

2.4 Condensate flow in tubes

The condensation flow processes inside tubes are complex because of the interaction between the liquid and vapour phases, and the simultaneous occurrence of heat and mass transfer. This interaction involves fluid motion interactions and condensation or mass transfer processes. During condensation flow, various flow regimes can occur. These flow regimes are a function of the type of tube, diameter, orientation (inclination), mass flux, vapour quality and type of fluid. These factors influence the flow regime that occurs at any local point along a tube. In order to accurately (better than 20%) predict the heat transfer coefficient and pressure drops (momentum transfer) the flow pattern must be known locally, (Dobson and Chato, 1998). It has also been stated by Thome and Hajal (2003) that only heat transfer and pressure drop correlations based on flow regimes can be considered as accurate for predictions in two-phase flow. It is therefore important to know and improve the ability to predict the flow pattern that prevails in a tube in order to make use of state of the art flow pattern based correlations.

2.4.1 Flow regimes during condensation

The first step in identifying the correlation to be used is to identify the flow regimes that will dominate in the condenser. The following section briefly describes the condensation process inside horizontal tubes and the flow regimes that can be expected. Saturated refrigerant vapour begins to condense on the side walls of a cooled tube. This even happens during the superheated phase when superheated vapour enters a condenser heat exchanger section followed by evaporation of the condensed film, (Thome, 2005). This could affect conclusions made on flow observations at this point. The flow regimes will be defined and named according to the flow regimes use by Kattan *et al.* (1998a) in his work on flow pattern maps. The regimes that are distinguished include: stratified (S), stratified-wavy (SW) (sometimes also wavy), annular (A), intermittent (I), misty (M) and bubbly (B). Kattan *et al.* (1998a) combines slug flow and plug flow into the intermittent flow regime. This study will focus on the intermittent flow regime and identify sub regimes within intermittent flow in order to set up time-fractional correlations between the sub regimes. An attempt will be made to

2.4 Condensate flow in tubes

classify the sub regimes as existing flow regimes that have existing heat transfer correlations in order to match the time-fractional relations to the heat transfer correlation for a more accurate model. For this reason particular interest will be given to the classification of intermittent flow and it will be attempted to maintain subjective criteria.

Two cases can be separated in order to describe all the flow regimes in condensation, high and low mass flux, (Figure 2.1). High mass fluxes of saturated refrigerant enters the condenser and condensates in an annular ring around the perimeter of the tube. The high mass flux shears tiny liquid droplets from the liquid wall and carries them along as a mist flow. The condensing refrigerant forms a liquid film on the side of the tube. As the vapour quality decreases the misty flow becomes pure annular and stratification of the large liquid mass begins. The stratification of liquid forms a pool at the bottom of the tube (Figure 2.1). The stratified flow begins to reach the top of the tube and slug flow resumes. This flow regime consists of vapour slugs encapsulated between liquid partitions and develops into longer bubbles that eventually fully condense and liquid flow continues from there on. For the low mass flux case the saturated vapour enters the condenser and a misty, annular flow occurs followed by a pure annular flow. From this point the low mass flux cannot maintain a liquid entrainment and gravity causes the liquid film to drain to the bottom of the tube, causing stratification. A stratified-wavy flow or at very low mass fluxes, pure stratified flow with no waves is possible.

During condensation the liquid pool offers the largest thermal resistance to heat transfer and the heat transferred through to liquid pool is often neglected. The majority of heat is transferred through the liquid film. The flow may be subjected to two flow mechanisms: laminar film condensation and forced convective condensation. Forced convective condensation for horizontal tube flow refers to the flow of condensed liquid along the tube and film condensation refers to the flow from top to bottom of the tube in the direction of gravity.

Flow can also be classified as either gravity controlled or vapour shear controlled. In gravity controlled flow the forces that tend to pull the fluid along the tube are dominated by gravity that pulls the fluid to the bottom of the tube and *vice versa* for shear flow. At low mass fluxes the liquid film that condenses on the

2.4 Condensate flow in tubes

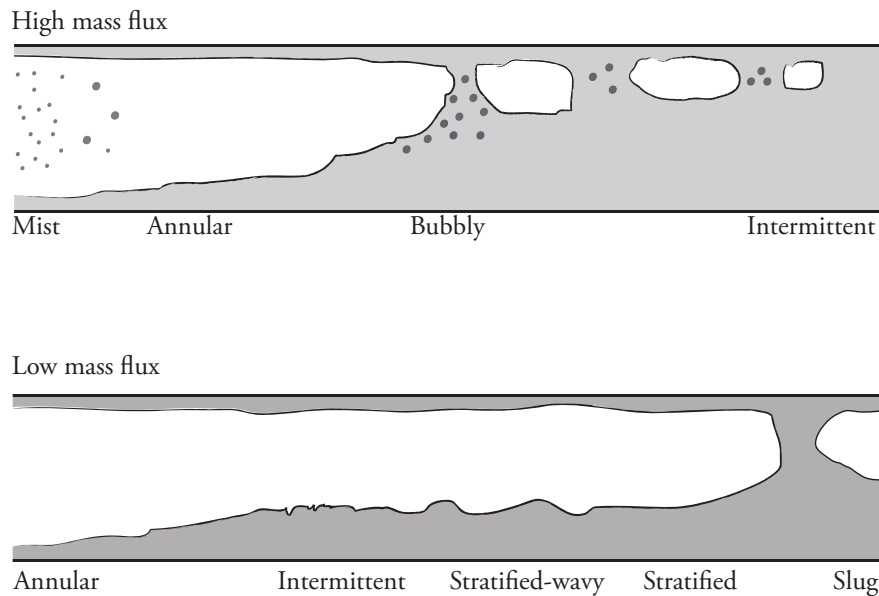


Figure 2.1: Flow regimes for condensation at high and low mass fluxes, adapted from Collier and Thome (1994). Flow direction from left to right

side walls accumulates at the bottom of the tube. This is called stratified flow and Nusselt film condensation occurs around the top of the tube (Thome *et al.*, 2003). Flow is stratified-wavy until pure stratified flow is reached at low vapour qualities or at very low mass fluxes. Gravity controlled flow regimes include stratified, wavy and slug flow. These regimes are lumped together primarily because the heat transfer is dominated by conduction across the film at the top of the tube and it is not a strong function of mass flux. The large thermal resistance of the liquid pool controls the overall heat transfer and most heat is transferred through the film. The heat transfer through the liquid pool is generally neglected. This type of condensation is called film condensation and was first modeled and studied by Nusselt in 1916.

Shear flow is represented in the annular flow regime. This flow regime has a near symmetric cross section with a liquid film and a high speed vapour core. Shear flows have a high dependence of mass flux and quality.


At high mass fluxes the vapour shear force overcomes gravity and the liquid film redistributes into an annular film. This typically occurs at void fractions $\varepsilon > 0.5$ and some liquid could be entrained in the high velocity vapour core. The

2.4 Condensate flow in tubes


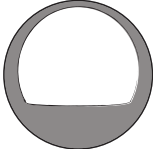
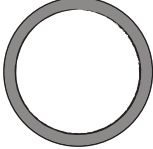
entrainment of liquid is thought to improve heat transfer because the resulting liquid film has to be thinner (Dobson, 1994). This regime is followed by slug flow, then plug flow and complete condensation. If considered together, slug, plug and bubbly flow typically occupies 10% to 12% of the quality range. Plug and bubbly flow occupy only 1% to 2% of the quality range (Dobson, 1994). The forced convective condensation mechanism is dominant in these flow regimes (Thome *et al.*, 2003) and the mass flux and heat transfer are therefore directly proportional.

In Table 2.3 the salient flow regimes are indicated on a cross sectional basis and the basic descriptors of these regimes are given.

Table 2.3: Flow regimes during in-tube condensation in horizontal tubes adapted from Dobson and Chato (1998)


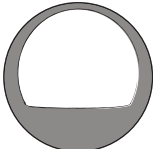
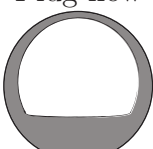
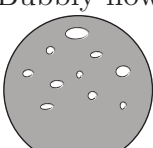
Flow regime	Description
Increasing vapour velocity	Forced convection condensation, void fraction > 0.5
Stratified flow 	<ul style="list-style-type: none"> • Very low vapour velocities • Condensate that forms on the top of the tube flows downward due to gravity • Condensate collects in a liquid pool at the bottom of the tube. This flow moves along due to vapour shear or a gravitational head (Kosky and Staub, 1971) • The velocity in the top of the tube is primarily downward • The velocity in the pool at the bottom of the tube is primarily in the mean flow direction • Very low vapour velocities result in smooth liquid-vapour interface (Dobson 1994)
<i>continued on next page</i>	

2.4 Condensate flow in tubes

Flow regime	Description
Wavy flow 	<ul style="list-style-type: none"> • Vapour velocity increases; Liquid-vapour interface becomes Helmholtz-unstable giving rise to surface waves (Dobson, 1994) • Condensation process in top of tube is similar to that in stratified flow, with gradual thickening of liquid layer feeding into pool at bottom of the tube • Condensation process at liquid-vapour interface is affected by waves as it is alternately exposed to a thin condensate film flowing downward or the crest of the wave that moves in the mean flow direction (Dobson, 1994)
Wavy-annular flow 	<ul style="list-style-type: none"> • Vapour velocity increases further • Wavy flow becomes unstable and can result in transitions to either slug flow at high liquid fractions, or wavy-annular flow at lower liquid fractions where the waves begin to wash up and around the circumference of the tube leading to an asymmetric annular film
Annular film flow 	<ul style="list-style-type: none"> • Further increase in vapour velocity • Liquid migration from the pool at the bottom of the tube to the top continues until the film thickness becomes nearly uniform • Visual appearance of this type of flow is one of an annular film of liquid against the wall and a high-speed vapour core in the centre • Liquid-vapour interface is nearly always characterized by surface waves due to the high-speed vapour flowing over it (Dobson, 1994)

continued on next page

2.4 Condensate flow in tubes

Flow regime	Description
Annular mist flow 	<ul style="list-style-type: none"> • Further increase in vapour velocity • Wave crests of liquid film are sheared off by the vapour flow and entrained in the core in the form of liquid droplets, giving rise to an annular film with a mixture of vapour and mist in the core flow
Decreasing void fraction	Laminar film condensation, void fraction < 0.5
Slug flow 	<ul style="list-style-type: none"> • Interfacial waves grow sufficiently in amplitude to block the entire cross-section at some axial locations, leading to the visual appearance of slugs of liquid flowing down the tube (Weisman et al. 1979) • These slugs cause large pressure spikes due to rapid deceleration of the vapour flow (Hubbard and Dukler, 1966; Dobson, 1994) • In other cases a slug like flow does not create these large pressure spikes, pseudo-slug flow. These slugs do not entirely block off the tube or they do so only momentarily
Plug flow 	<ul style="list-style-type: none"> • Slugs coalesce into elongated bubbles within a predominantly liquid flow (Weisman et al. 1979) • Large vapour bubbles pass at random with liquid flow in between and no small bubbles or frothy flow
Bubbly flow 	<ul style="list-style-type: none"> • Turbulent fluctuations within the liquid eventually break these plugs into small, dispersed vapour bubbles
<i>continued on next page</i>	

Flow regime	Description
-------------	-------------

2.4.2 Methods of observation

Historically, visual observations are used as the principal method of flow regime identification. This is a subjective method and results in discrepancies in the noted flow regimes by various researchers under similar conditions. This is a major reason for investigating alternative, more objective, flow regime identification methods. Some of the observation methods used by researchers in the past are mentioned here. Many techniques have been developed during the past 30 years

- Visual observations consist of observing and recording images in a transparent section of tube. This method, as described, has its drawbacks in terms of the subjective nature of such observations. For observations made at the end of a condenser heat exchanger section, the presence of a condensing film would cause flow to appear annular or intermittent (El Hajal *et al.*, 2003), resulting in further bias of reports. This method is still the mainstay of flow pattern identification.
- A more advanced type of visual observation is the laser sheet technique used by Thome and coworkers, developed by Ursenbacher *et al.* (2004), to record void fraction data in stratified flow by recording an oblique cross section of tube and reconstructing the correct cross section. This method also offer accurate void fraction information and therefore vapour qualities can also be verified. This method is limited because it can only be applied to stratified flows.
- Another visual method developed by Revellin *et al.* (2006) involves the use of thin lasers and diodes to sense the light. This method is applied to plug type flows in micro channels but demonstrates the principal that will be used in this study. Two laser beams, a fixed and accurately measure distance apart, are focused through a transparent section of tube. The voltage signal from the sensor is proportional to the light intensity. Cut offs are defined for vapour and liquid and then the signals can be used to count bubbles, frequency analysis and to measure the velocity of bubbles.

2.4 Condensate flow in tubes

- The method of using pressure signals and analyzing a power spectral density, (PSD) of the pressure drop between two nearby wall locations was first mentioned by Hubbard and Dukler (1966). Their experiment dealt with air-water flows. Another group, Weisman *et al.* (1979), used the pressure difference between two nearby pressure signals as indicator of flow pattern in air-water flows. Their study did not yet make use of frequency analysis but mention is made of the possibility to use frequency analysis. The method of using power spectral density (PSD) signals was proven and used by Liebenberg (2002) to characterise refrigerant flow.
- There have been many efforts to develop capacitive void fraction sensors that use the di-electric properties of the fluid to generate a signal that is proportional to the void fraction of fluid in the tube. Attempts are under development for capacitive void fraction measurements, but these are mostly for air-water and oil-water flow (Elkow and Rezkallah, 1996; Jowarek and Krupa, 2004; Tollefsen and Hammer, 1998). Capacitive void fraction sensing of refrigerants have been under development by Gent University by De Paepe *et al.* (2006). As it turns out the signal from this sensor can be used to generate probability density functions (PDF), cumulative probability density functions (CPDF) and fast Fourier transforms (FFT) data that can be used as flow regime descriptors.

The first researchers to find objectivity in flow regime identification, using PDF of void fraction signal were Jones and Zuber (1974). Keska *et al.* (1999) also used other signal processing tools like the root mean square (RMS), power spectral density (PSD) and cumulative probability density function (CPDF) on a density measurements. These tools only showed significant results for capacitive sensors.

- Research has also been done using an electromagnetic flow meter. This device detects the potential difference between electrodes that is induced when a conducting fluid flows through the magnetic field. The magnetic field is excited by a low frequency voltage and the difference in the output signal can be used to make deductions on the flow pattern. This method is used with success in bubbly and slug flow regimes by Cha *et al.* (2002).

2.4 Condensate flow in tubes

- Another sensor type used to sample information on flow patterns and dynamic stability is the resistive impedance technique. The signal from this device is a function of the local interfacial area or void fraction Klein *et al.* (2004). This device uses an excitation ring and a sensory ring mounted flush with the tube. The sensor is connected to conditioning electronics and the signal can then be sample by a data acquisition system
- The signal from a density meter was compared to the results from visual, pressure and capacitive sensors in order to determine the capability of these methods to discriminate between flow regimes (Keska *et al.*, 1999).
- Genetic algorithms are used as a search technique in computing to find optima and to do searches. These algorithms are a class that find application by using methods inspired by natural systems and evolutionary biology. A solution domain is defined in a genetic manner and the fitness parameter is also set up. A generation is evaluated by the fitness profile and only the fittest samples in the population are allowed to propagate to the next generation. This method has found application in flow pattern mapping and other two-phase flow applications (Cho *et al.*, 2001)
- Visualization by neutron radiography is a suitable method for two-phase flow studies. Quantitative measurements of cross-sectional averaged void fraction of two-phase flows are done for various flow patterns. The uncertainty of void fraction in slug flow is about 0.2 (Takenaka and Asano, 2005). In comparison with the drift flux model the radiography method for slug flow is within 20% for churn and for annular it is within 6%. When using the method described in Takenaka and Asano (2005) no changes need to be made to the experimental setup.
- Ultra sound also offers the possibility to image flow and for the calculation of flow velocity with the use of several techniques. The use of ultrasound is however generally reserved for use in biological systems and the analysis of blood vessels and heart functions (Aoudi *et al.*, 2006)

2.4 Condensate flow in tubes

In this study an investigation was launched to find an objective measure within a recorded image observation of a tube. For this reason visual observations are made at the sight glass at the beginning of the test condenser. This location is preceded with a length of tube that is adiabatic and at least 0.5 meters or 55 (L/D ratio) diameters of straight tube. This is done to ensure that the flow patterns observed is representative of an equilibrium condition (Weisman *et al.*, 1979). The frequencies observed in condensing refrigerant flow occur from 1 to 120 Hz and a Nyquist folding frequency analysis results in a sampling rate of at least 240 Hz to eliminate any aliasing (Liebenberg *et al.*, 2005). The frame rate of the camera was kept at 250 fps. The signal from the camera was analyzed using National Instruments Software, NI Vision development module. The details of the hardware and software are given in Chapter 3. The image signal was masked to include only the refrigerant section of the tube and an image intensity of each image, taken at 250 frames per second (fps), was taken. Due to the defraction of light from the liquid vapour interface, various intensities of light is captured through the sight glass. It is this signal that is used to discriminate between flow patterns. The time-domain data, frequency domain data and probability density function data can be recorded and used to evaluate the flow regime.

2.4.3 Flow map history

It has been established that it is essential for designers to determine the flow regime that is present in the heat exchanger based on the flow rate, tube diameter and fluid properties. There are many flow regime maps available for use in the case of horizontal, two phase flow. Maps of transitions for adiabatic conditions have been proposed by Taitel and Dukler (1976) and Baker (1954), as well as Mandhane *et al.* (1974), Soliman and Azer (1974), Hashizume (1983) and Steiner (1993). Other maps have been developed for condensation, taking into account the diabatic conditions in heat exchangers. These maps include those of Breber *et al.* (1980), Soliman (1982), Cavallini *et al.* (2002); Tandon *et al.* (1982), and El Hajal *et al.* (2003). The maps presented by El Hajal *et al.* (2003) and Thome *et al.* (2003) is based on the widely accepted evaporation flow map presented by Kattan *et al.* (1998a,b) and will be used as a basis for this study.

2.4 Condensate flow in tubes

The above mentioned maps all use transition criteria to define a boundary between the various regimes. Each map defines its own flow regimes and groups some flow types together while others discriminate each flow type. Because of the discrepancies in the description of these many flow regime maps the latest and proven map of El Hajal *et al.* (2003) will be used in this study.

Papers have also been presented that discriminate between stratified and non-stratified flows. Among them is Akers and Rosson (1960), Sardesai *et al.* (1981), Shah (1979) and Dobson and Chato (1998).

The availability of such a number of flow pattern maps presents some problems as defined by Thome *et al.* (2003) and the aim in recent years has been to develop a unified model for two phase flows and in attaining this goal, this current study will be based on the work done by El Hajal *et al.* (2003) in collaboration with that by Thome and Cavallini. The problems that usually arise with the flow maps and transition criteria are:

- There are a large number of maps to choose from and no indication which is best for a specific application.
- Flow regimes are described with different names and categorized into different groupings under different definitions. This results in qualitative measures with no quantitative measures for comparison.
- The subjective nature of flow observations. One observer would classify a particular flow regime differently from another. The transition regions, where correct classification is important, become very biased and unclear.
- Some flow pattern maps discriminate between some stable regimes while others do not and this leads to difficulty in comparisons of the maps.
- The transition zones are large and result in a scenario where both flow regimes occur intermittently.
- There may or may not be hysteresis during transitions.
- Observations of a flow regime and its transition to all the bordering patterns are not usually available thus increasing the difficulty in defining a transition.

- Many maps used are for adiabatic flow and do not consider diabatic conditions.

2.4.4 Contemporary flow condensation maps

In this section a short description of a selection of contemporary flow pattern maps are given. These maps are all commonly used by designers and engineers and are for horizontal smooth tubes.

2.4.4.1 Baker map, 1954

This map is based on adiabatic flow in large tubes, ranging from 24.4 mm to 101.6 mm in diameter (Baker, 1954). The fluids involved were air-water and oil-water mixtures. A typical Baker map is shown in Figure 2.2. The map coordinates are made up of appropriately scaled superficial liquid and vapour mass velocities. The scaling takes care of variations in fluid properties. The horizontal and vertical coordinates are given by $G_{water} = G_l/\psi$ and $G_{air} = G_v\lambda$ where ψ and λ are given by equations 2.1 and 2.2 respectively, where subscripts w and a depict water at room temperature and air at atmospheric pressure respectively.

Flow patterns were said to be strong functions of superficial liquid and vapour velocities and weak functions of other parameters like tube diameter and density (Mandhane *et al.*, 1974; Weisman *et al.*, 1979). The flow pattern maps of the time were defined with superficial phase velocities as axes. The superficial velocity of a phase is when that single phase is considered to fill the entire tube and the velocity is calculated from the mass flow of that phase. There is no connection with the actual velocity of the phase in the tube unless single phase flow exists.

$$\psi = \left(\frac{\sigma_w}{\sigma}\right)\left(\frac{\mu_l}{\mu_w}\right)^{\frac{1}{3}}\left(\frac{\rho_w}{\rho_l}\right)^{\frac{2}{3}} \quad (2.1)$$

$$\lambda = \left(\frac{\rho_v}{\rho_a}\right)\left(\frac{\rho_l}{\rho_w}\right)^{\frac{1}{2}} \quad (2.2)$$

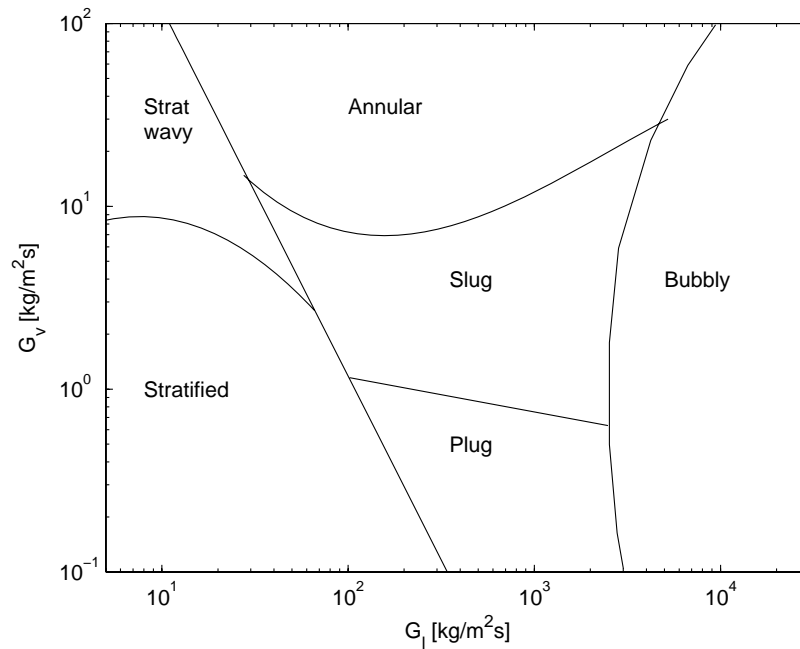


Figure 2.2: Baker flow map for air-water at standard conditions

2.4.4.2 Mandhane map, 1974

The Mandhane map (Mandhane *et al.*, 1974) is based on the Baker map and uses superficial gas and liquid velocity as horizontal and vertical coordinates. The map is based on a large data base of adiabatic two phase flows and categorizes flow into stratified-wavy, wavy, bubbly, slug and annular flows. Weisman *et al.* (1979) reports that not taking the diameter of tubes into consideration introduces errors in the map.

The Mandhane map has been used for condensing refrigerants, but problems have been experienced due to the higher vapour density of refrigerants compared with air (Wattelet *et al.*, 1994). Dobson (1994) modified the superficial vapour velocity to account for the high vapour densities. The modified superficial vapour velocity agrees better with experimental data. Some changes in the interpretation of flow regimes were also made. This included classifying annular-wavy flow as slug flow for refrigerants. The Mandhane map using modified superficial vapour velocity is shown in Figure 2.3. The modified superficial vapour velocity as de-

2.4 Condensate flow in tubes

defined in equation 2.3 was first introduced by Dobson and Chato (1998). The modification is defined to take into account the large difference in densities of refrigerant versus air and water cycles.

$$j_v^{corr} = \sqrt{\rho_g/\rho_a} \cdot j_v \quad (2.3)$$

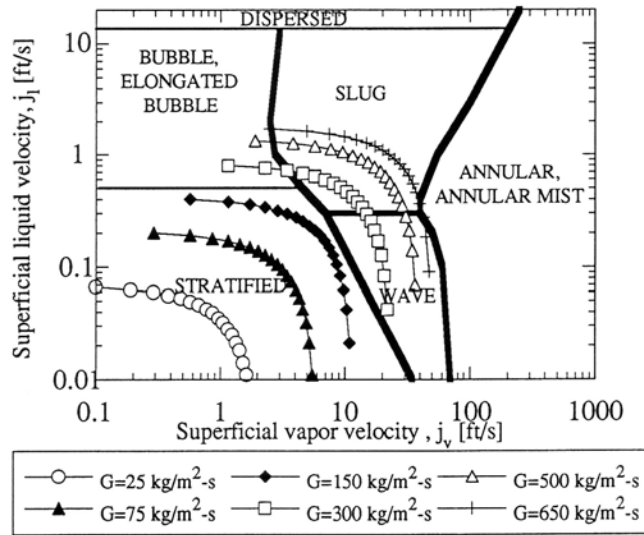


Figure 2.3: Mandhane map with Dobson (1994) modifications

2.4.4.3 Breber map, 1980

Breber *et al.* (1980) predict flow pattern transitions based on a dimensionless vapour mass velocity, j_g^* , equation 2.4, and the Lockhart-Martinelli parameter X_{tt} , equation 2.5. The dimensionless velocity is indicative of the ratio between shear and gravity forces (Breber *et al.*, 1980). The Lockhart-Martinelli parameter states the liquid volume fraction and is the ratio of liquid-to-vapour pressure drops. At lower velocities gravity dominates, while shear forces dominate at higher velocities and give rise to annular flows. The Breber map defines the zones of flow regimes as given in Table 2.4 and in Figure 2.4.

2.4 Condensate flow in tubes

$$j_g^* = \frac{xG}{[gD\rho_g(\rho_l - \rho_g)]}^{0.5} \quad (2.4)$$

$$X_{tt} = \left(\frac{\rho_v}{\rho_l}\right)^{0.5} \left(\frac{\mu_l}{\mu_v}\right)^{0.1} \left[\frac{(1-x)}{x}\right]^{0.9} \quad (2.5)$$

Table 2.4: Flow pattern criteria

Flow pattern	j_g^*	X_{tt}
Mist and annular	> 1.5	< 1.0
Wavy and stratified	< 0.5	< 1.0
Slug	< 0.5	> 1.5
Bubble	> 1.5	> 1.5

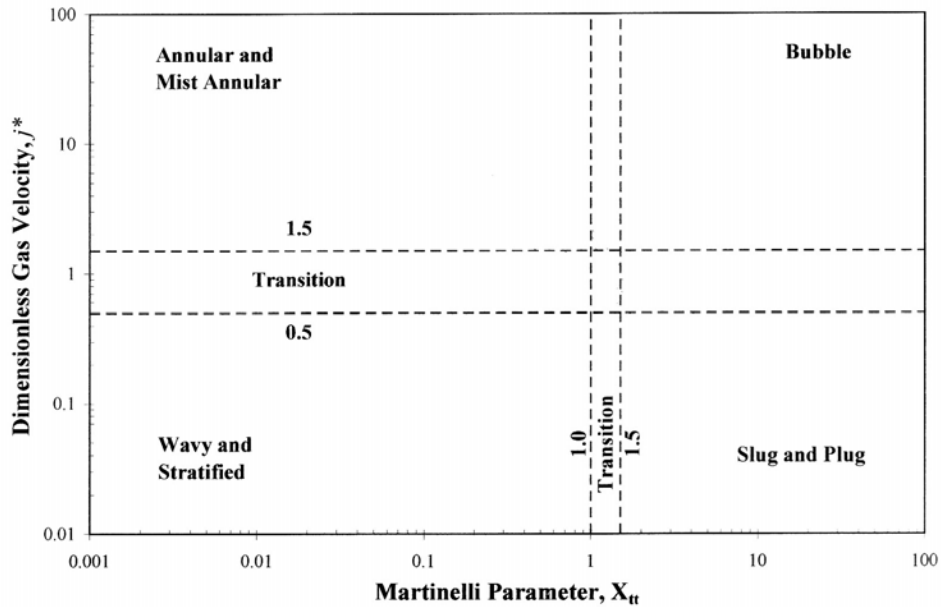


Figure 2.4: Breber *et al.* (1980) map

2.4.4.4 Taitel and Dukler map, 1976

Taitel and Dukler (1976) developed a semi-theoretical flow regime map. They reasoned that flow regime transitions were based on a different set of competing forces, that a single parameter or a set of coordinates cannot predict all transitions and that only combinations of dimensionless groupings that they defined can predict transitions. The Taitel and Dukler (1976) map predicts stratified, stratified-wavy, intermittent (slug and plug), annular flow and dispersed bubble flow. The map has been used for diabatic flow even though it is an adiabatic map.

The flow transitions defined by Taitel and Dukler are dependent on a modified Froude number, F_{td} , and the liquid Reynolds number, Re_l . The transitions used by Taitel and Dukler are given in Table 2.5.

$$F_{td} = \sqrt{\frac{\rho_g}{\rho_l - \rho_g}} \frac{\frac{Gx}{\rho_g}}{\sqrt{Dg \cos \varepsilon}} \quad (2.6)$$

$$K_{td} = F_{td} \sqrt{Re_l} \quad (2.7)$$

Table 2.5: Flow pattern criteria of Taitel and Dukler (1976)

Flow pattern	Criteria
Stratified to wavy	$K_{td} \geq \frac{20}{\{\tilde{u}_g \sqrt{\tilde{u}_l}\}}$
Stratified-wavy to intermittent annular	$F_{td}^2 \left[\left(\frac{1}{(1-\tilde{h}_l)^2} \right) \frac{\tilde{\mu}_g^2 \sqrt{1-(2\tilde{h}_l-1)^2}}{\tilde{A}_g} \right] \geq 1$
	Intermittent flow $\tilde{h}_l > 0.5$
	Annular flow $\tilde{h}_l < 0.5$
Intermittent to bubbly	$T_{td}^2 > \left[\frac{8\tilde{A}_g (\tilde{\mu}_l \tilde{D}_l)^n}{\tilde{S}_i \tilde{\mu}_l^2} \right]$
	where $T_{td} = \left[\frac{-(\frac{\delta p}{\delta z})_l}{(\rho_l - \rho_v)g \cos \varepsilon} \right]$
	$= \left[\frac{2\alpha}{Re_l^u} \frac{j_l^2}{gD \cos \varepsilon} \frac{1}{1 - \frac{\rho_v}{\rho_l}} \right]$

The Taitel and Dukler map can be plotted on a two-dimensional axis if no dispersed bubble flow is present. This eliminates the need for the additional transition line. Figure 2.5 is a plot of the Taitel and Dukler transitions on a plot of X_{tt} and F_{td} .

When all the axes and transitions of the Taitel and Dukler map are combined onto one graph, Figure 2.6 is constructed. The transition lines and combination of axes that they use are given in the legend.

2.4.4.5 Soliman map, 1982

The Soliman (1982) flow regime map was specifically developed for flow condensation and is based on experimental testing done with water, refrigerants and acetone. Soliman grouped several flow regimes together and based his map on three flow regimes: wavy flow including stratified, slug and wavy flows, annular flow and mist flow. The Soliman map is based on two transition criteria men-

2.4 Condensate flow in tubes

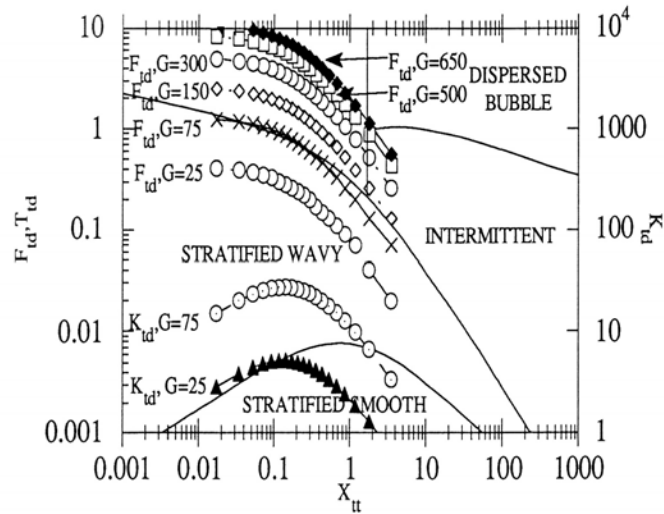


Figure 2.5: Taitel and Dukler map (1976) used by Dobson (1994)

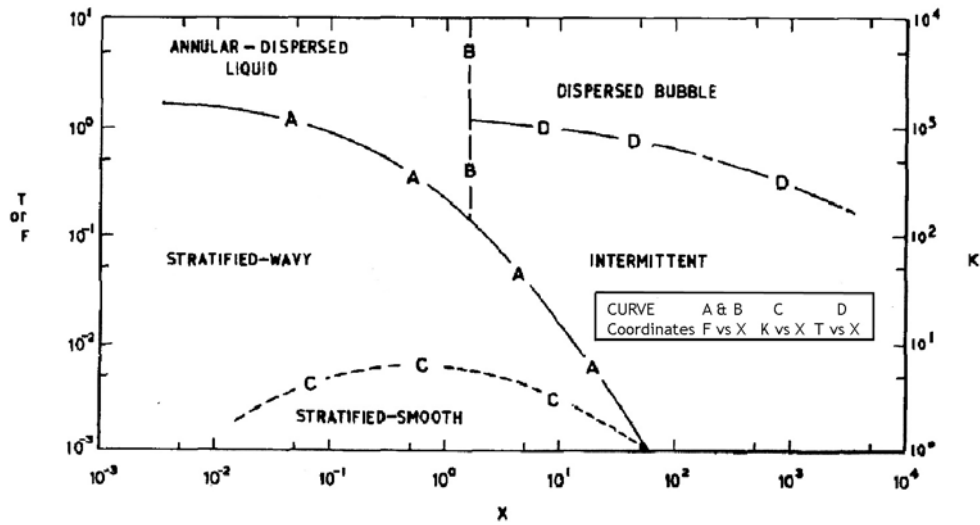


Figure 2.6: Taitel and Dukler map on combined axes (Bukasa *et al.*, 2004)

tioned in Table 2.6 and the flow pattern map for condensing R-134a is illustrated in Figure 2.7.

2.4 Condensate flow in tubes

Table 2.6: Soliman transition criteria

Flow pattern	Criteria
Wavy to annular	For $Re_l \leq 1250$: $Fr_{so} = 0.025 Re_l^{1.59} \left[\frac{1+1.09 X_{tt}^{0.039}}{X_{tt}} \right]^{1.5} \frac{1}{Ga^{0.5}}$
	For $Re_l > 1250$: $Fr_{so} = 1.26 Re_l^{1.04} \left[\frac{1+1.09 X_{tt}^{0.039}}{X_{tt}} \right]^{1.5} \frac{1}{Ga^{0.5}}$
	Wavy flow $Fr < 7$
	Annular flow $Fr > 7$
	Wavy to annular transition $Fr = 7$ (Dobson and Chato, 1998)
	Symmetric annular flow $Fr = 18$ (Dobson and Chato, 1998)
Annular to mist	For $Re \leq 1250$: $We_{so} = 2.45 \frac{Re_v^{0.64}}{Su_v^{0.3} (1+1.09 X_{tt}^{0.039})^{0.4}}$
	For $Re > 1250$: $We_{so} = 0.85 \left[\left(\frac{\mu_v}{\mu_l} \right)^2 \left(\frac{\rho_l}{\rho_v} \right) \right]^{0.084} \frac{Re_v^{0.79} X_{tt}^{0.157}}{Su_v^{0.3} (1+1.09 X_{tt}^{0.039})^{0.4}}$
	Annular flow $We_{so} < 20$
	Pure mist flow $We_{so} > 30$
	Annular to mist flow $20 < We < 30$

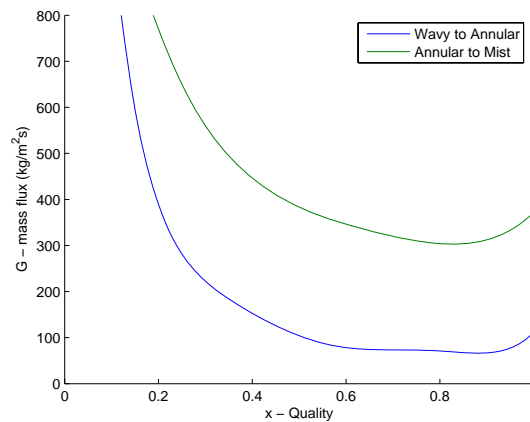


Figure 2.7: Soliman (1982) map

2.4.4.6 Weisman et al. map, 1979

Weisman *et al.* (1979) presented extensive data on two phase flow patterns in horizontal tubes. They compared their data with other experiments and presented revised dimensionless transition correlation that fits all the data.

This flow regime map is of specific importance because pressure signals were used to define the transitions and as secondary indicator of flow regime. At the time of the study the availability of frequency domain analyzers were not common and the study used time domain data.

The Weisman *et al.* (1979) map shows a considerable increase in accuracy in comparison with other experimenters (Wang *et al.*, 1997). The data captured by Wang *et al.* (1997) are compared to the Weisman et al. transitions in Figure 2.8.

Table 2.7: Weisman transition criteria

Transition	Equation
Stratified-intermittent transition	$\frac{u_{gs}}{\sqrt{gD_i}} = 0.25\left(\frac{u_{gs}}{u_{ls}}\right)^{1.1}$
Stratified-wavy transition	$\left[\frac{\sigma}{gD_i(\rho_l - \rho_g)}\right]^{0.2} \left[\frac{D_i u_{gs} \rho_g}{\mu_g}\right]^{0.45} = 8\left(\frac{u_{gs}}{u_{ls}}\right)^{0.16}$
Transition to annular flow	$1.9\left(\frac{u_{gs}}{u_{ls}}\right)^{\frac{1}{8}} = \left[\frac{u_{gs} \rho_g^{0.5}}{gD_i(\rho_l - \rho_g)}\right]^{0.2} \left[\frac{u_{gs}^2}{gD_i}\right]^{0.18}$
Transition to dispersed flow	$\left[\frac{(\frac{\delta p}{\delta x})_l}{gD_i(\rho_l - \rho_g)}\right]^{0.5} \left[\frac{\sigma}{g^2 D_i(\rho_l - \rho_g)}\right]^{-0.25} = 9.7$

2.4.4.7 Dobson and Chato map

Dobson and Chato (1998) suggested a modification to the superficial vapour velocity used by Mandhane, section 2.4.4.2, in order to improve the transition accuracy.

$$j_v^{corr} = \sqrt{\frac{\rho_g}{\rho_a}} j_v \quad (2.8)$$

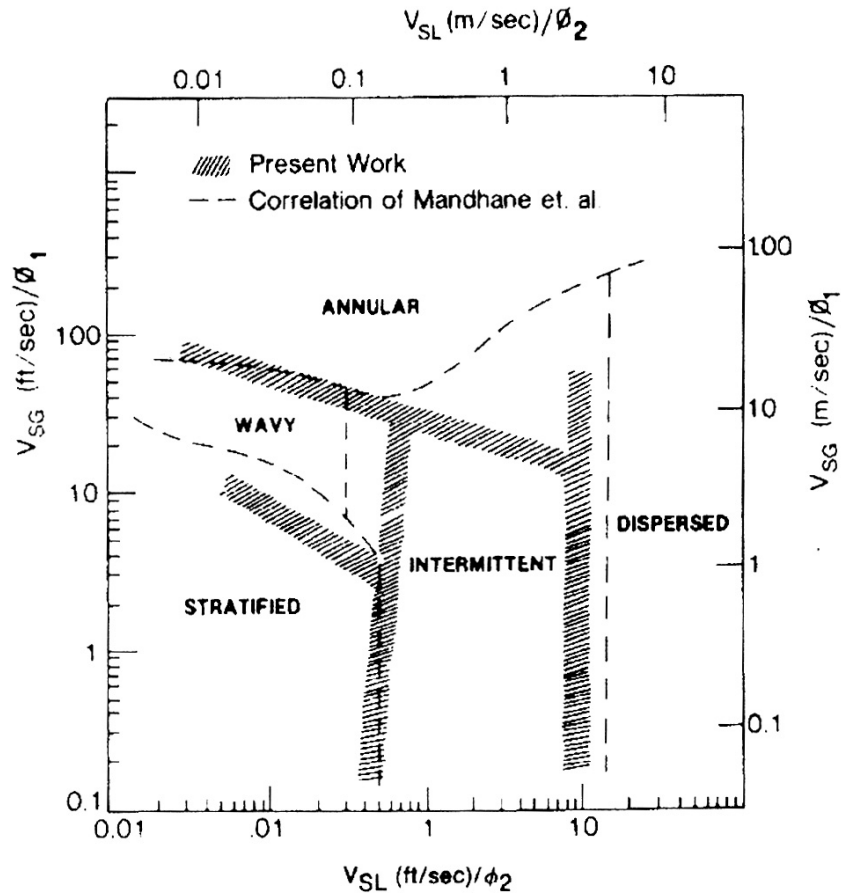


Figure 2.8: Comparison of observations by Weisman *et al.* (1979) flow regime map to Mandhane *et al.* (1974)

Equation 2.8 states that the modified superficial velocity is proportional to the square root of the vapour kinetic energy. This change is made to vapour and liquid superficial velocities. Making this simple correction to the Mandhane map produced much better agreement with experimental data (Dobson and Chato, 1998). The modification is defined to take into account the large difference in densities of refrigerant versus air and water cycles.

They found that the Soliman transition between wavy and annular flow is better presented by a Froude number of 20 rather than 7. The transitions predicted by Dobson and Chato (1998) is compared against the observations of El Hajal *et al.* (2003) and some agreement is present.

2.4.4.8 Sardesai et al. map, 1981

Sardesai *et al.* (1981) applied the recommendations of the German VDI *Heat Atlas* to the transition between stratified and non-stratified flow. Their map correlates well with the El Hajal et al. condensation map.

They used the ratio, R , of heat transfer coefficients on the bottom and top of the tube with a parameter β that they defined. The ratio R relies on the assumed difference in heat transfer that would occur between stratified and non-stratified flows. The parameter β is defined as a scale of the stratified-wavy to annular transition of Taitel and Dukler, $\beta(F, X_{tt})$. They produced the map shown in Figure 2.9 that distinguishes between stratified and non-stratified flows. They also commented on the temperature dependence and independence of flows in the two regimes, noting that gravity controlled flow is temperature dependent. Thus, the temperature at the top and bottom of the tube and the heat transfer coefficients of these points show a temperature dependence in gravity controlled flow. A heat transfer model based on the principle mentioned here is given in Cavallini *et al.* (2006).

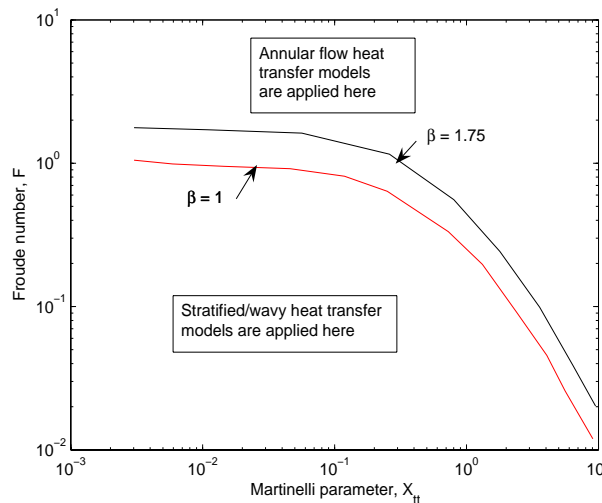


Figure 2.9: Sardesai *et al.* (1981) heat transfer guide

2.4.4.9 Cavallini et al. map, 2002

The Cavallini *et al.* (2002) flow pattern map is a composite of flow transition criteria proposed by other researchers into a single map. They adapted transition boundaries in the flow regimes to corresponding transitions found in their heat transfer data. The details of transition criteria and heat transfer models used in this map are described in Cavallini *et al.* (2002).

2.4.4.10 Cavallini et al. map, 2006

This latest heat transfer model from Cavallini *et al.* (2006) is based on the flow regime map modification done by Sardesai *et al.* (1981) on the Taitel and Dukler (1976) transition. Instead of using the Sardesai map as a flow regime map Cavallini uses it to define two zones where different heat transfer models are applicable. The transition is basically the same as proposed by Sardesai *et al.* (1981) and Cavallini has two heat transfer equations for the two zones, temperature dependent and temperature independent, (Figure 2.10). The intermittent zone is defined as a combination of the two zones. This model is very simple and compares well with data sets from many independent researchers.

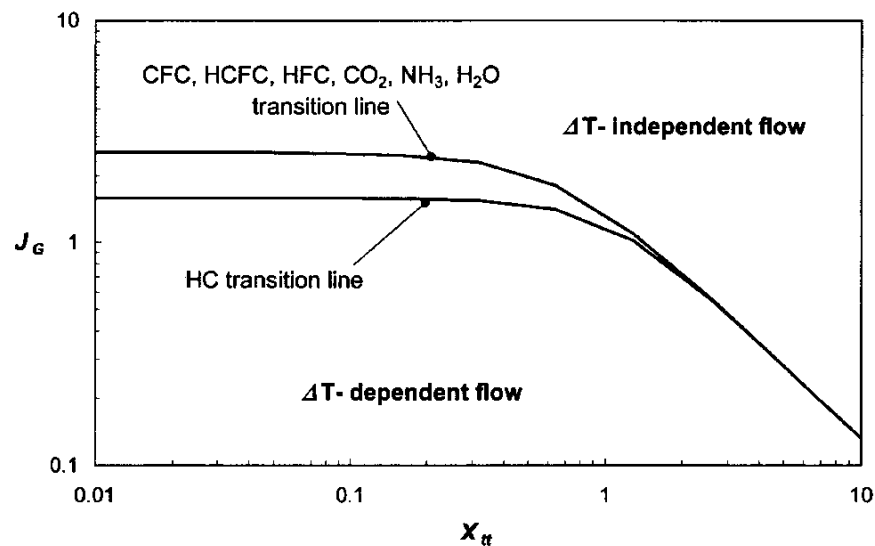


Figure 2.10: ΔT -dependent and ΔT -independent transition

2.4.4.11 Time-fraction methods

Probabilistic time-fractional data have been presented by Niño *et al.* (2002). In their study of multi port flows in microchannel they evaluated video images of the flow for a set amount of time. The samples was representative of the typical flow patterns for the set mass flows and vapour qualities. The video analysis classified the flow in every tube according to the flow regime present. The result of analysing the flow regimes at the mass flows as seen in Figure 2.11. The flow regimes are classified according to the fraction of time that they are likely the be found in the tubes. The variation in compositional makeup of the flow regimes present can be followed for each mass flow across the quality range. This method will make up the basis of the methods developed further in this study.

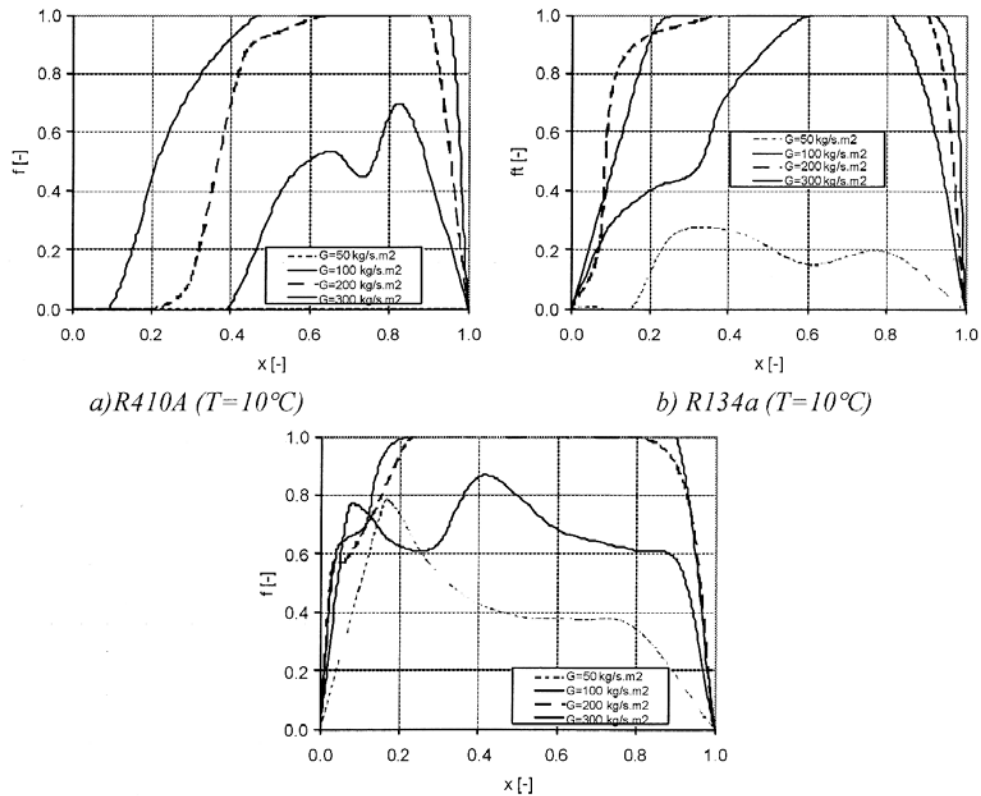


Figure 2.11: Time-fractional data for several mass flows (Niño *et al.*, 2002)

Research on probabilistic mapping of two-phase flow that was done concur-

2.4 Condensate flow in tubes

rently with this study at the UIUC (Jassim, 2007). In the study a time-fractional map was produced for a mass flux and vapour quality range spanning over intermittent, annular and stratified-wavy flows in tube diameters from 1 to 8 mm. A unique flow pattern recognition method was developed in this study to identify the flow patterns present in the tube. The video footage of the experiments are saved in *.avi* files which are analysed with the above mentioned method and allocated time-fractions to every flow regime. This resulted in time-fractions allocated to each flow regime for the mass fluxes tested. In using a continuous time fractional model the discontinuities in conventional flow pattern based correlations fall away and a more natural approach to flow pattern transition happen where the one blends into the next as the time-fractional coefficient changes. The study then used physical parameters to define a function that can be used to give a time fractional coefficient to each of the heat transfer correlations selected for the model. The study also expanded the probability time fractional model to pressure drop and void fractional models.

2.4.5 El Hajal et al. map, 2003

An important characteristic in any two-phase flow is the void fraction. El Hajal *et al.* (2003) defined a logarithmic mean void fraction, equation 2.11, for accurate prediction of void fraction over a wide pressure and vapour quality range, based on the homogeneous (2.9) and Rouhani and Axelsson (2.10) void fractions for working with fluids at high reduced pressures.

$$\varepsilon_h = \left[1 + \left(\frac{1-x}{x}\right)\left(\frac{\rho_v}{\rho_l}\right)\right]^{-1} \quad (2.9)$$

$$\varepsilon_{ra} = \frac{\frac{x}{\rho_v}([1 + 0.12(1-x)])}{\left[\frac{x}{\rho_v} + \frac{1-x}{\rho_l} + \frac{1.18(1-x)[g\sigma(\rho_l - \rho_v)]^{0.25}}{G\rho_l^{0.5}}\right]} \quad (2.10)$$

$$\varepsilon = \frac{\varepsilon_h - \varepsilon_{ra}}{\ln\left(\frac{\varepsilon_h}{\varepsilon_{ra}}\right)} \quad (2.11)$$

The flow pattern map used in this study and discussed here is based on the maps presented by Kattan *et al.* (1998a). This map is modified from the Steiner (1993) map, which is based on the Taitel and Dukler (1976) map for adiabatic conditions in horizontal tubes. The updated version of the map by Kattan *et al.* (1998a) is used by Thome and Hajal (2003) for the basis of the condensation flow map. The condensation map differs from the evaporation map in that the transition between annular and stratified wavy flow does not represent the onset of dry-out, which is an evaporation phenomenon. For condensation flow the quality decreases and as this happens the flow condition moves from right to left on the flow map (Figure 2.12). When saturated vapour enters the condenser it forms either a thin liquid annular film or a liquid layer at the bottom of the tube in a stratified or stratified-wavy flow with a gravity controlled liquid film. This means that flow either forms an annular or stratified-wavy flow depending on the mass flux being above or below G_{wavy} .

The parameters required to evaluate the condensation flow pattern transitions are given in Table 2.8.

The flow regimes are described by geometrical models (Thome, 2005). For stratified flow see Figure 2.13 where P_L is the stratified perimeter around the

Table 2.8: Parameter needed for flow pattern determination Kattan *et al.* (1998a)

Parameter	Variable	Units
Internal tube diameter	d	m
Vapour quality	x	-
Total mass velocity	G	kg/m^2s
Liquid density	ρ_l	kg/m^3
Vapour density	ρ_v	kg/m^3
Liquid dynamic viscosity	μ_l	kg/ms
Vapour dynamic viscosity	μ_v	kg/ms
Surface tension	σ	Ns

tube while P_V describes the remaining non-stratified perimeter, h_L is the liquid height, P_i is the interface length and A_L and A_V are the cross-sectional areas of liquid and vapour respectively. These variables are normalized using the tube diameter in equation 2.12.

$$h_{Ld} = \frac{h_L}{d}, P_{id} = \frac{P_i}{d}, A_{Ld} = \frac{A_L}{d^2}, A_{Vd} = \frac{A_V}{d^2} \quad (2.12)$$

The logarithmic mean, $(LM\varepsilon)$ void fraction equation is used to obtain ε and allows the use of the flow pattern map at high reduced pressures. The cross-sectional area, A , of the tube can be used to determine the values of: A_L , A_V , A_{Ld} and A_{Vd} with equation 2.13.

$$A_L = A(1 - \varepsilon), A_V = A\varepsilon \quad (2.13)$$

The area A_L does not include the condensate formed around the perimeter of the tube. This leaves only the stratified angle to compute. This can be done iteratively by using equation 2.14 by solving equation 2.15.

$$A_{Ld} = \frac{1}{8} [(2\pi - \theta_{strat}) - \sin(2\pi - \theta_{strat})] \quad (2.14)$$

$$\theta_{strat} = 2\pi - 2 \left\{ \begin{array}{l} \pi(1 - \varepsilon) + \left(\frac{3\pi}{2}\right)^{\frac{1}{3}} [1 - 2(1 - \varepsilon) + (1 - \varepsilon)^{\frac{1}{3}} - \varepsilon^{\frac{1}{3}}] \\ -\frac{1}{200}(1 - \varepsilon)\varepsilon[1 - 2(1 - \varepsilon)][1 + 4((1 - \varepsilon)^2 + \varepsilon^2)] \end{array} \right\} \quad (2.15)$$

The dimensionless liquid height can be determined from the geometric equation 2.16.

$$h_{Ld} = 0.5 \left(1 - \cos\left(\frac{2\pi - \theta_{strat}}{2}\right) \right) \quad (2.16)$$

P_{id} can be expressed in terms of θ_{strat} as equation 2.17.

$$h_{Ld} = 0.5 \left(1 - \cos\left(\frac{2\pi - \theta_{strat}}{2}\right) \right) \quad (2.17)$$

These transitions are based on the equations from the Zürcher *et al.* (2002) evaporation map. In condensation some of the factors influencing the equation can be neglected. There is no dry-out in condensation and therefore heat flux effect is not taken into account. Thus, the values of F_1 and F_2 are 0 and 1.023 respectively and the transition equation for wavy flow is given as equation 2.18. The minimum value of this equation has the coordinate $(x_{min}, (G_{wavy})_{min})$. From this point for all vapour qualities $x > x_{min}$, $G_{wavy} = (G_{wavy})_{min}$ as seen in Figure 2.12.

$$G_{wavy} = \left\{ \frac{16A_{Vd}^3 g d \rho_L \rho_V}{x^2 \pi^2 (1 - (2h_{Ld} - 1)^2)^{0.5}} \left[\frac{\pi^2}{25h_{Ld}^2} \left(\frac{We}{Fr} \right)_L^{-1.023} + 1 \right] \right\}^{0.5} + 50 - 75e^{\frac{-(x^2 - 0.97)^2}{x(1-x)}} \quad (2.18)$$

The transition line between fully stratified and stratified-wavy flow is defined by the updated Zürcher *et al.* (2002) equation 2.19.

$$G_{strat} = \left\{ \frac{(226.3)^2 A_{Ld} A_{Vd}^2 \rho_V (\rho_L - \rho_V) \mu_L g}{x^2 (1 - x) \pi^3} \right\}^{\frac{1}{3}} + 20x \quad (2.19)$$

The transition between intermittent and annular flow is a vertical line given in equation 2.20 by x_{IA} . This transition can be defined by plotting the Froude rate against the void fraction (Liebenberg, 2002). The x_{IA} line is bounded by the G_{wavy} and G_{misty} lines below and above.

2.4 Condensate flow in tubes

$$x_{IA} = \{[0.2914(\frac{\rho_V}{\rho_L})^{-1/1.75}(\frac{\mu_L}{\mu_V})^{1/7}] + 1\}^{-1} \quad (2.20)$$

The transition between annular and intermittent flow to misty flow at higher flow rates is given by equation 2.21. In equation 2.21 the ratio of liquid Weber number to liquid Froude number is given by equation 2.22 and ξ is defined in equation 2.23. The G_{mist} equation is evaluated for all x to find the minimum ($< x_{min}, (G_{mist})_{min} >$). For all $x > x_{min}$, G_{mist} is set equal to $(G_{mist})_{min}$.

$$G_{mist} = \left\{ \frac{7680A_{Vd}^2gd\rho_L\rho_V}{x^2\pi^2\xi} \left(\frac{Fr}{We}\right)_L \right\}^{0.5} \quad (2.21)$$

$$\left(\frac{We}{Fr}\right)_L = \frac{gd^2\rho_L}{\sigma} \quad (2.22)$$

$$\xi = \left[1.138 + 2 \log\left(\frac{\pi}{1.5A_{Ld}}\right) \right]^{-2} \quad (2.23)$$

The bubbly flow regime occurs at very high flow ranges and the transition line is define in equation 2.24.

$$G_{bubbly} = \left\{ \frac{256A_{Vd}A_{Ld}^2d^{1.25}\rho_L(\rho_L - \rho_V)g}{0.3164(1-x)^{1.75}\pi^2P_{id}\mu_L^{0.25}} \right\}^{1/1.75} \quad (2.24)$$

The local flow patterns can then be determined by the procedure described in El Hajal *et al.* (2003). To identify the flow pattern transitions during design of a condenser the design value of mass flux, G , is used. For visualization purposes it is stated that a mass flux, G , in the general range of interest be selected. The choice of mass flux, G , affects the void fraction to a small extent. For a detailed discussion of the effects that certain parameters have on the flow map refer to section 2.5.1.

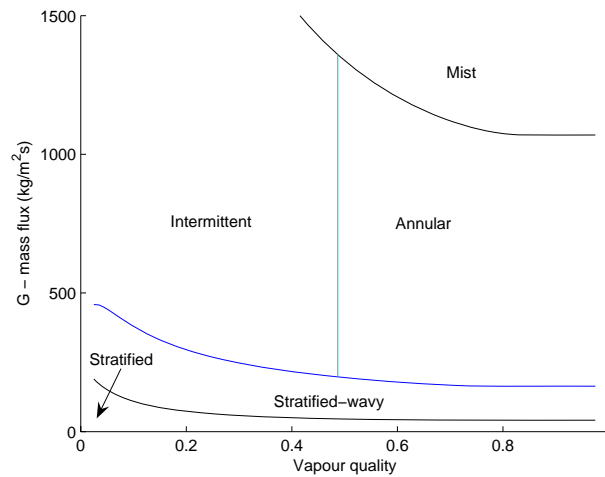


Figure 2.12: The El Hajal *et al.* (2003) condensation flow map

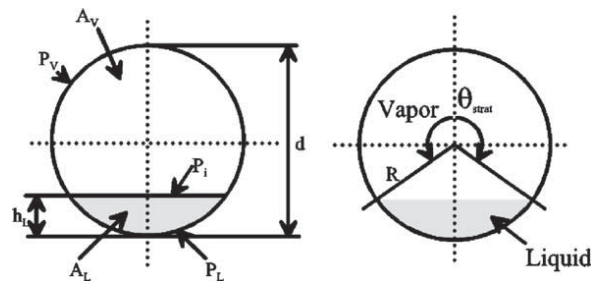


Figure 2.13: Void fraction geometry for stratified flow (El Hajal *et al.*, 2003)

2.4.6 Comparison of maps

Currently the most advanced model taking into account the flow regime and geometry of flows is that of El Hajal *et al.* (2003). This map has its origins in the evaporation work done by Kattan *et al.* (1998a,b). Kattan did an evaluation of many different flow maps and based his boiling map on that of Steiner (1993), which is based on the original map from Taitel and Dukler (1976) as stated above.

There are many flow maps that originated from many laboratories over the years and for many different types of flow. Many flow maps are for adiabatic

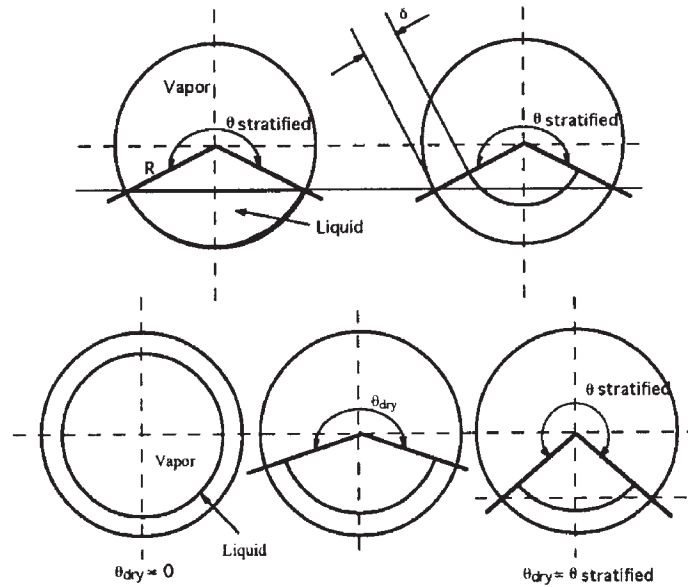


Figure 2.14: Other void fraction geometries (Thome *et al.*, 2003)

conditions and do not account for the changes in flow patterns brought on by diabatic conditions. This is however the focus of work done by Kattan *et al.* (1998a) and their flow map.

In the studies done by Dobson and Chato (1976) and El Hajal *et al.* (2003), they compared their visual observations with transitions of Mandhane *et al.*, Taitel and Dukler, Breber *et al.*, Tandon *et al.*, Sardesai *et al.*, Dobson and Chato, and Soliman. In their studies they found problems in the methodology of flow regime map reporting. First the subjectivity of visual reports and the use of unique categories to classify flow regimes are considerable. If visual recordings were made at the end of a condenser test section the Nusselt film condensation on the perimeter of the tube will cause transitions to be lower. Last there is a discrepancy between the transitional areas defined by different researchers. For example, Soliman includes stratified, wavy and slug flow in one regime while Mandhane, and Taitel and Dukler treat these as three different regimes. The

2.4 Condensate flow in tubes

more transitions the higher the possibility of incorrectly defining a flow regime area.

The following comments have been made by Dobson (1994), Dobson and Chato (1998) and El Hajal *et al.* (2003) on flow pattern maps.

Breber *et al.* (1980) map

- Agreement to within $\pm 25 \text{ kg/m}^2 \text{ s}$ was found for the transition between stratified-wavy and annular flow by El Hajal *et al.* (2003). The Breber map coincided with the El Hajal map in the regions of stratified, stratified-wavy flow and the Breber slug and plug flow coincided with intermittent flow regimes by El Hajal.

Mandhane *et al.* (1974) map

- This map was found to be a poor predictor of flow regime by Dobson and Chato (1998) and Liebenberg (2002). This was a result of the higher vapour densities compared with the original data.
- A correction factor was defined by Dobson (1994) that resulted in a larger increase in accuracy.
- The Mandhane map is not defined as a function of tube diameter and this was mentioned as a potential problem for smaller tubes by Dobson and Chato (1998)

Tandon *et al.* (1982) map

- The stratified-wavy to intermittent transition of the Tandon map coincided well with the transition from the El Hajal *et al.* map but deviated at higher vapour qualities.
- The slug and plug regime of Tandon compared well with intermittent flow regimes on El Hajal *et al.*
- Annular/semi-annular flow on the Tandon map agreed with annular and intermittent flow regimes of El Hajal *et al.* (2003).

Taitel and Dukler (1976) map

- The Taitel and Dukler flow regime map distinguishes between the stratified and stratified-wavy flow regimes with success.
- This map predicts that slug flow is directly followed by annular flow at low qualities although experiments have shown that slug flow is followed by wavy, wavy-annular and annular flow as quality increases.
- The annular flow regime on the Taitel and Dukler (1976) map exhibits a larger amount of stratification, particularly at low qualities or high Lockhart-Martinelli parameters.
- Kattan *et al.* (1998a) stated that the Taitel and Dukler map correctly predicted only 50% of their data.

Soliman (1982) map with Dobson and Chato (1998) modifications

- Good agreement between the wavy to intermittent and the intermittent to annular transitions were found by El Hajal *et al.* (2003).
- Soliman's predictions of wavy to annular transition agrees well with Taitel and Dukler at high vapour qualities.

2.4 Condensate flow in tubes

- Soliman lumped flow regimes together and this results in difficult comparisons. At high mass fluxes the region predicted to be wavy flow by Soliman corresponds almost exactly to the slug flow region by Taitel and Dukler. At lower mass fluxes the region predicted to be wavy flow extends to higher qualities than the slug flow boundary by Taitel and Dukler.
- Annular flow transition from Soliman corresponds well to the wavy to wavy-annular transition given in Dobson and Chato (1998).
- The wavy-annular to annular transition is well predicted by $Fr_{so} = 18$ rather than 7.
- The Soliman map includes a distinct mist flow region that is absent from other maps.
- The Soliman mist flow region corresponds well with annular-mist predicted by Dobson (1994).

The Sardesai map is based on the Taitel and Dukler map. They added a parameter to assist in discriminating between annular or non-stratified flows and stratified flow. The heat transfer on the top and bottom of the tube was used and the Taitel and Dukler transition function was modified. Their flow patterns fall correctly within the El Hajal et al. map.

The Cavallini et al. 2002 annular flow regime (Cavallini *et al.*, 2002) coincides with the El Hajal annular regime, but definition of the transition+stratified-way zone by Cavallini et al. is not clear and overlaps the intermittent and stratified-way zones defined by the El Hajal et al. map.

The Cavallini et al. 2006 heat transfer model (Cavallini *et al.*, 2006) is based on the flow regimes as defined in Sardesai *et al.* (1981). They distinguish between annular (ΔT -independent) and stratified (ΔT -dependent) flows and apply the appropriate heat transfer models.

2.4 Condensate flow in tubes

Dobson and Chato proposed modifications to the Mandhane et al. map and the Soliman wavy flow transition. The transition that they define intersects the El Hajal et al. map but differs at high and low qualities. Some of the other observations made by Dobson and Chato correlates well with the transitions defined by El Hajal et al. The two maps were evaluated at different mass fluxes but the effect should be minimal.

Dobson (1994) and El Hajal *et al.* (2003) concluded the following on condensation flow regimes in horizontal tubes. Flow regimes that can be expected in practical condensers include: wavy, wavy-annular, annular and annular-mist flow. Slug or pseudo-slug flow followed at the lower vapour qualities. There was no mist flow observed without a stable liquid film. The net mass flux towards the wall during condensation always results in a stable liquid film (Dobson and Chato, 1998). Pure stratified flow existed at the lowest mass fluxes around 25 kg/m^2s and would not be present in practical condensers. There still remains a large amount of subjectivity in flow regime reporting.

2.4.6.1 Conclusion

The heat transfer model by Thome and coworkers is extensive and has much more rigor. The method is accurate and leads to good results. Opposing methods that are simple and easy to use include the new Cavallini *et al.* (2006) heat transfer model and does not rely heavily on the flow regime to be identified. This method is also fairly accurate but is not yet proven over the entire flow and pressure range.

The main problem with the Thome method is the determination of the flow regime. If simplicity and objectivity can be obtained in this process the rest of the model will hopefully follow naturally and in combination with advances in the heat transfer models this method may be most accurate for design and development of a wide range of applications.

2.5 Transitions

A list of transitions defined by researchers over the years are given in Table 2.9.

Table 2.9: Transition criteria by various authors

	Annular	Wavy-stratified	Slug	Transition annular to wavy	Transition annular to slug
Taitel and Dukler (1976)		$K_{td} \geq \frac{20}{\{u_g \sqrt{u_l}\}}$	$Fr_{td}^2 \left(\frac{1}{(1-h_l)^2} \right)$ $\left[\frac{\bar{\mu}_g^2}{A_g} \frac{1-(2h_l-1)^2}{A_g} \right]$ ≥ 1		
Weisman (1979)	$1.9 \left(\frac{u_{gs}}{u_{ls}} \right)^{\frac{1}{8}} =$ $\left[\frac{u_{gs} \rho_g^{0.5}}{[g D_i (\rho_l - \rho_g)]^{0.25}} \right]^{0.2}$ $\left[\frac{u_{gs}^2}{g D_i} \right]^{0.18}$	$\left[\frac{\sigma}{g D_i (\rho_l - \rho_g)} \right]^{0.2}$ $\left[\frac{D_i u_{gs} \rho_g}{\mu_g} \right]^{0.45}$ $= 8 \left(\frac{u_{gs}}{u_{ls}} \right)^{0.16}$	$\frac{u_{gs}}{\sqrt{g D_i}} =$ $0.25 \left(\frac{u_{gs}}{u_{ls}} \right)^{1.1}$		$\left[\frac{(\frac{\delta p}{\delta x})_l}{g D_i (\rho_l - \rho_g)} \right]^{0.5}$ $\left[\frac{\sigma}{g^2 D_i (\rho_l - \rho_g)} \right]^{-0.25}$ $= 9.7$
Breber (1980)	$J_G > 1.5$ $X < 1.0$	$J_G < 0.5$ $X < 1.0$	$J_G < 1.5$ $X > 1.5$	$1.5 < j_G < 0.5$ $X < 1.0$	$J_G < 0.5$ $1.0 < X < 1.5$
Sardesai (1981)	$J_G > J_{G1} =$ $\frac{1.75}{(0.7X^2 + 2X + 0.85)}$ $X < 1.6$	$J_G < J_{G2} =$ $\frac{1}{(0.7X^2 + 2X + 0.85)}$		$J_{G2} < J_G < J_{G1}$ $X < 1.6$	
Soliman (1982)	$We_{so} < 20$ $Fr > 7$	$Fr < 7$		$Re_l \leq 1250$ $Fr_{so} = 0.025$: $Re_l^{1.59}$ $\left[\frac{1 + 1.09 X_{tt}^{0.039}}{X_{tt}} \right]^{1.5}$ $\frac{1}{Ga^{0.5}}$ and	

continued on next page

2.5 Transitions

	Annular	Wavy-stratified	Slug	Transition annular to wavy	Transition annular to slug
				$Re_l > 1250$ $Fr_{so} = 1.26 Re_l^{1.04}$ $[\frac{1+1.09X_{tt}^{0.039}}{X_{tt}}]^{1.5}$ $\frac{1}{Ga^{0.5}}$	
Dobson and Chato (1998)	$G > 500$ $kg/m^2 s$ or $G < 500$ $kg/m^2 s$ and $Fr_{so} > 20$				
Cavallini (2002)	$J_G > 2.5X_{tt} < 1.6$			$J_G < 2.5X_{tt} < 1.6$	$J_G < 2.5X_{tt} > 1.6$
Thome, El Hajal (2003)	Equation 2.20	Equation 2.19		Equation 2.18	
Cavallini (2006)	$\frac{J_G > J_{G1} = \frac{1.75}{(0.7X^2+2X+0.85)}}{X < 1.6}$	$\frac{J_G < J_{G2} = \frac{1}{(0.7X^2+2X+0.85)}}$		$\frac{J_{G2} < J_G < J_{G1} X < 1.6}$	

2.5.1 Effect of variables on transitions

The functions used to describe transitions are complex and make use of many variables. Some are more important than others and might even be unnecessary. By close examination of transitions and the effects that they cause, simpler transition criteria would hopefully become obvious.

Variables that affect flow pattern transitions:

- **Mass flux.** Mass flux and quality are the dominant factors affecting the flow regime. As mass flux increases flow becomes wavy and less stratified. Later annular flows and mist flow prevails as the vapour shear increases.

- **Vapour Quality.** Vapour quality has a direct relation to the void fraction. At high qualities the liquid film is thin and becomes thicker and unstable as the quality decreases. At lower qualities, slug then plug flow and bubbly flow occurs.
- **Tube diameter.** A reduction in tube diameter results in a shift of the transitions of wavy to wavy-annular and wavy-annular to annular, to lower qualities.
- **Working fluid.** The differences that fluid properties make becomes clear in the transition regions where not one flow regime is dominant. The primary fluid properties that affect the flow regime is the vapour and liquid densities and viscosities, the ratios between these quantities and surface tension.
- **Reduced pressure.** Much of the difference in fluid properties is due to the reduced pressure. At high reduced pressures the liquid and vapour properties become similar and the surface tension decreases. At low reduced pressures annular flow is present over a wider quality range.
- **Density and viscosity.** Physical properties like density and viscosity can have minor effects on flow transitions. For a model to be complete it needs to be compared with a variety of fluids and take the physical differences into account.
- **Oil.** The presence of lubrication oil in condensers affects the surface tension which is proven to have an effect on the pressure drop and heat transfer (Dobson and Chato, 1998).

The dominant factors affecting the flow regime were mass flux and vapour quality. The thermo-physical properties affected the flow regime in the 150 – 300 kg/m^2s range where there is no dominant flow regime. At a given mass flux where wavy, wavy-annular and annular flows occurred, the size of the quality range occupied by annular flow was greater at lower reduced pressures. It follows that R-134a at 35 °C will exhibit the most annular flow and R-410A at 45 °C the least annular flow (El Hajal *et al.*, 2003). A higher temperature results in a greater reduced pressure for a refrigerant.

2.6 Time-Frequency analysis

As proven by Hervieu and Seleglim (1998) the time-frequency domain analysis of the signal from an inductive sensor can be used as an objective indicator of flow regime. Later the use of time-frequency analysis in the intermittent regime to prove the existence of sub regimes was done by Klein *et al.* (2004). In these cases an inductive sensor was used on air-water flows and in both cases the method proved successful in identifying flow regimes. The use of time-frequency analysis has not been exploited much further.

In this study the time-frequency analysis of other parameters will be investigated. The first and most obvious step is to analyse the pressure signal of two-phase condensing flows as done by Liebenberg (2002), since the frequency domain has already been investigated and was found to contain significant frequency information. Second, since a capacitive void fraction sensor is available the voltage signal that we capture from this device will also be analysed for time-frequency content. Third a high speed video camera is used to record the two-phase flow through a short section of glass tube. This is related to the classical visual observation method that is subject to the objectivity of the researcher. In an attempt to improve this method the light intensity of the recorded 8-bit image over a selection of areas in the image will be analysed using spectral techniques. The area of interest consists of a rectangular section of the image spanning the inside of the tube and for a short length along the tube. The transient intensity signal is the analysed with various methods including statistical analyses and time-frequency analysis.

The object of all this analysis is to attempt to reveal the transient nature of intermittent flow. First the various methods mentioned above will be investigated for suitability for this type of analysis. If the sub regimes present within intermittent flow show significant differences on a time-frequency domain plot, spectrogram, the analysis will be carried further. The advantage of the visual signal is that the signal can be analysed in parallel with the visual recording and the time domain signal, thus giving the researcher more information on which to base decisions.

2.6 Time-Frequency analysis

The purpose of the study is to use the time-frequency data for the intermittent regime and to map the sub regimes within the intermittent regime. The method can hopefully be proven in this study and taken further by future studies. The mapping of the sub regimes will be done by a statistical time-fractional analysis of the time-frequency data. The time-fractional data can then be used for a correlation that will map the sub regimes of the intermittent regime. The purpose of time-frequency analysis in this study is to serve as a tool for the time-fractional analysis of the two-phase flows, instead of visual inspection of each frame.

The end result of a sub mapped intermittent regime is the ability to apply a more local heat transfer and possibly pressure drop correlation in the intermittent flow regime resulting in more accurate heat transfer predictions.

It is known from Fourier theory that any signal can be expressed as the sum of a series (possibly infinite) of sines and cosines. The major disadvantage of such Fourier expansions is that they only represent frequency data and no time data. This means that we can determine all the frequencies present in a signal but not when they occur. Several methods have been developed in the past decades in order to represent a signal in the time and frequency domain simultaneously.

The basic premise of time-frequency representation is to cut the signal into smaller parts and to analyse each part separately in the frequency domain. From this method short time Fourier transforms, spectral analysis and time-frequency analysis with Fourier transforms, power spectral densities, Wigner-Ville analysis and many more came to be. A time-frequency distribution is a transform that maps a 1-D signal into a 2-D time-frequency map that describes how the frequency content changes with time.

The short time Fourier transform (STFT), defines a window function that is multiplied with the signal and translated along in time. The Fourier transform is then taken of each signal and the time-frequency map is constructed. Much is dependent on the window function in STFT analysis. The type of windows to choose from include square, Gaussian, triangular and many more. The length of the window also determines the final resolution of the map. A longer window will have more accurate frequency information as a result and shorter windows give better time resolution, both at the expense of the other.

2.7 Mathematical background

In contrast to the short time Fourier transform (STFT), which is resolution limited either in time or in frequency (determined by the window function) and also has smearing and side leakage problems. The Wigner-Ville spectrum offers good time and frequency resolution. The Wigner-Ville spectrum is a quadratic transform which results in cross terms that make interpretation difficult. Higher order Wigner-Ville distributions suppress the cross terms.

A newer solution to the time-frequency problem is wavelet analysis. In wavelet analysis a scalable, modulated window function, called a wavelet or mother function, is used to solve the signal cutting problem (Matlab R15, Reading, MA). The window function is shifted along the signal and a spectrogram is calculated at every position. The window function scale is then increased or decreased and the process is repeated (Figure 2.15). By this scaling and translating of the mother function a wavelet analysis is done. In the case of wavelet analysis the result is usually not known as time-frequency but as time-scale representation. The final result is a time versus scale graph indicating the presence of scales with high accuracy on the timeline. An equivalent frequency or pseudo frequency can be calculated that corresponds to the scale and larger scales represent higher frequencies. Wavelet analysis is complicated by the choice of wavelet, the interpretation of frequencies as scales and the ranges to set the analysis up for. For these reasons wavelet analysis will not be used in this study.

Different methods were investigated and evaluated. The STFT was found to be simple and even with its limitations STFT allows good flexibility when window size and type can be controlled. The Wigner-Ville and higher order time-frequency analysis was found more complex and with no similar increase in usefulness for this application. Wavelet analysis is very powerful and can pick up small variations in time accurately. The interpretation and complexity of parameters in the analysis like wavelet choice, window and scale to frequency translation excludes this method of analysis.

2.7 Mathematical background

The analysis of the frequency content of a signal based on the Fourier transform may not succeed in describing the process and all physical aspects because the

2.7 Mathematical background

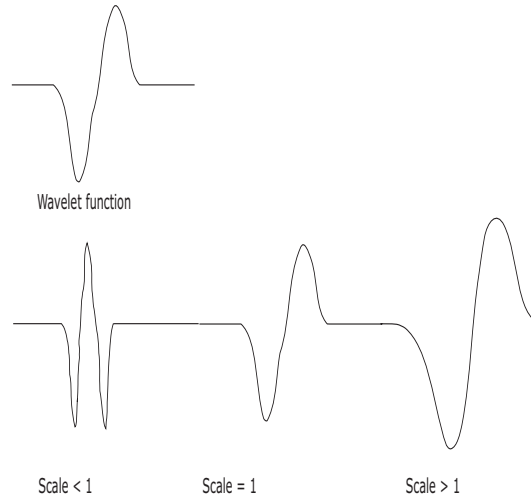


Figure 2.15: Principle of wavelet analysis

temporal information is overlaid due to the integration in time. It becomes obvious that a joint time-frequency representation is necessary to pinpoint all physical aspects of the signal. There are several methods available in this approach. Described here and used in this study is a method called spectral analysis that is equivalent to a short time Fourier transform (STFT) analysis. A window function is translate over the signal to emphasize temporal features in certain regions of the signal. If $s(\tau)$ denotes the original signal and $h_t(\tau)$ denotes the window function centered at $\tau = t$ with implicit duration. It is now possible to define a new signal with emphasis around time t as 2.25, (OpenCourseWare, 2006).

$$s_t(\tau) = s_\tau \cdot h_t(\tau) \quad (2.25)$$

The new signal depends on three aspects: the window function $h_t(\tau)$, the instant of analysis t and the implicit length of the window, T . Since the signal will now be emphasized around time, t , the Fourier analysis (equation 2.26) or power spectral analysis will also reflect the spectral composition of the signal around time t , (OpenCourseWare, 2006).

$$S_t(\omega) = \frac{1}{\sqrt{2\pi}} \int_{-\infty}^{\infty} s_t(\tau) e^{-i\omega\tau} d\tau \quad (2.26)$$

Replacing $s_t(\tau)$ in equation 2.26 with equation 2.25,

$$S_t(\omega) = \frac{1}{\sqrt{2\pi}} \int_{-\infty}^{\infty} s(\tau)h(\tau)e^{-i\omega\tau} d\tau \quad (2.27)$$

The resulting time-frequency spectral density can be defined according to the following equation,

$$P(t, \omega) = \|S_t(\omega)\| = \left| \frac{1}{\sqrt{2\pi}} \int_{-\infty}^{\infty} s(\tau)h(\tau)e^{-i\omega\tau} d\tau \right|^2 \quad (2.28)$$

Where the power spectral density is defined as the product of the Fourier transform and its complex conjugate, equation 2.29. This equation as with all the above are stated for the continuous transform.

$$\Phi(\omega) = \left| \frac{1}{2\pi} \int_{-\infty}^{\infty} f(t)e^{-i\omega t} dt \right|^2 = \frac{S(\omega)S^*(\omega)}{2\pi} \quad (2.29)$$

2.8 Conclusion

Knowing the flow regime means knowing what mechanisms are responsible for heat transfer and pressure drop. The Thome et al. map defines the flow regime and transitions based on mass flux and vapour quality. In the future heat transfer and pressure drop correlations based on flow regimes and the fluid dynamics in these flow regimes will be the cornerstone of prediction methods. The methods used however still need to be developed to a level where they seamlessly integrate. The rest of this dissertation mentions the experimental system that was designed and installed and then a hypothesis is stated. The experimental work is focussed on the validation of the techniques used and not yet on the validation of the hypothesis. The purpose is to improve accuracy of correlations with a novel analysis method.

Chapter 3

Experimental Set-up

3.1 Introduction

This chapter describes the conceptualization, construction, components and commissioning of the experimental system. The experimental setup envisioned by the department was to be modular in such a way that condensation and evaporation experiments could be done on the same system. The system was to improve on the design on an existing setup used by the Rand Afrikaans University (RAU), now University of Johannesburg. The RAU system used a 12 meter long continuous condenser test section for smooth tube and a shorter length for enhanced tubes. The test section had short coaxial heat exchanger sections linked by adiabatic U bends in which the refrigerant condensed from superheated vapour to subcooled liquid. This section could not be locally controlled and measurements had to be taken at each heat exchanger section regardless of the properties at that point. The new design attempts to allow control of the properties at the inlet to the test section. Figure 3.1 shows a top view of the laboratory and the two-phase flow experimental setup.



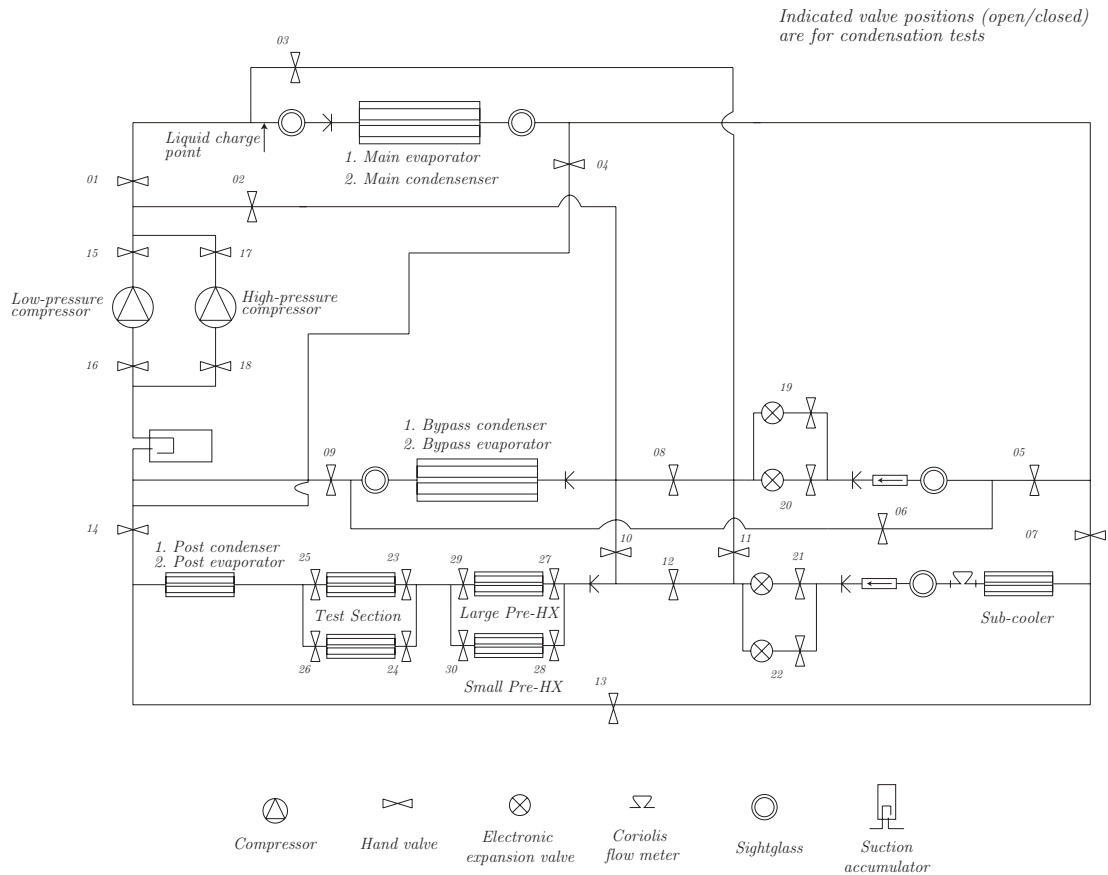
Figure 3.1: Top view of the two-phase flow experimental setup

3.2 Test Facility

3.2.1 Refrigerant cycle

The modular heat pump's refrigerant cycle (see Figure 3.2), which can be used to perform both evaporation and condensation tests, allows for the test section's inlet and outlet properties of the refrigerant to be controlled. To control the mass flow, a bypass section would be used to divert the excess flow through a bypass condenser. To enable control of the refrigerant properties, the test line is made up of a sequence of heat exchangers, which is as follows: a pre-condenser to control the test section's inlet properties, the test-section condenser, a post-condenser to ensure that that the refrigerant is in the subcooled regime, and the sub-cooler, to control superheat. A simplified test schematic for condensation experimentation is shown in Figure 3.10.

3.2 Test Facility



Valve Positions

- | | |
|------------|-----------------|
| 1. Closed | 16. Open |
| 2. Open | 17. Closed |
| 3. Open | 18. Closed |
| 4. Open | 19. Closed/Open |
| 5. Closed | 20. Open/Closed |
| 6. Open | 21. Closed/Open |
| 7. Closed | 22. Open/Closed |
| 8. Closed | 23. Open |
| 9. Closed | 24. Closed |
| 10. Open | 25. Open |
| 11. Open | 26. Closed |
| 12. Closed | 27. Open |
| 13. Open | 28. Closed |
| 14. Closed | 29. Open |
| 15. Open | 30. Closed |

Figure 3.2: Physical refrigerant pipe connection schematic

3.2 Test Facility

This system utilizes a Copeland scroll ZR72 (10 kW nominal cooling) compressor that delivers smooth flow in the refrigerant loop. This selection was done to minimize the pressure pulses present when using reciprocating-type compressors. In addition, the screw compressor does not require as much lubrication as its reciprocating counterpart. Figure 3.3 shows a rear-view of the test bench. The compressor is protected by internal thermal overload and over current protection systems including: a low-pressure switch set to a pressure of 300 kPa at the inlet of the compressor, a high-pressure switch set to 2500 kPa at the outlet of the compressor, and a safety high-pressure switch that ensures that the inlet pressure to the compressor is below 1200 kPa and that there is a pressure difference greater than 300 kPa between the compressor ports.

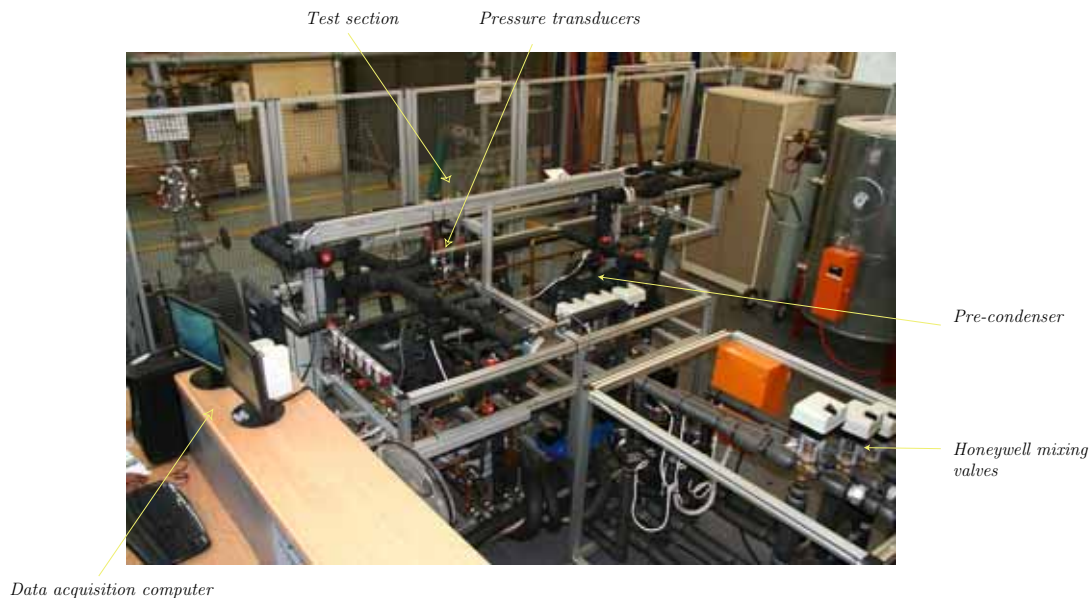


Figure 3.3: Rear view of the refrigerant bench

The refrigerant line splits into two after the compressor. The test line continues on to the pre-condenser. The bypass line contains only the bypass heat exchanger and an electronic expansion valve. The bypass line is used to divert flow from the test section for low mass flow tests, as was stated previously. The expansion valves on both these lines are discussed later.

3.2 Test Facility

The pre-condenser is used to control the properties at the inlet of the test section. The methods utilized are elaborated in more detail in Section 3.4. The properties at the inlet of the pre-condenser (exit of compressor) are assumed to be superheated. The refrigerant thermal properties are measured at the inlet of the pre-condenser. The state of the refrigerant before the pre-condenser is used as the starting point for calculations of properties and energy balance; for testing to commence, the energy balance from the pre-condenser inlet up to the post-condenser outlet has to be below 1%. The measurement devices used are discussed later, in Section 3.4.

The test section splits into two after the pre-condenser and rejoins before the post-condenser. These lines can be used independently by opening and closing manual valves at the inlets and outlets of the test sections. This allows a new test section to be inserted without disturbing tests. The test section can be constructed to the required length that will allow for flow to fully develop and such that it has a long enough diabatic section for sufficient heat exchange (for tests to be accurate relative to the thermocouple accuracy). Both sections can be shut off with valves and are equipped with vacuum points and stainless steel flanges with Teflon seals. The test line will be instrumented with the necessary temperature and pressure measurement devices. Sight glasses are used directly before and after the diabatic section as insulators against axial conduction through the copper tube and for visual recordings to be made using a high-speed camera and uniform backlight. Fluid axial conduction can be neglected, as stated in Liebenberg (2002). The effect of axial conduction and the purpose of the sight glasses with respect to this phenomenon are discussed later. As mentioned previously, the energy balance is maintained until the exit of the post-condenser. The test line is the only part of the system where measurements are taken and on which calculations are performed. As such, it is not necessary to have an energy balance over the entire system.

After the test-section, the flow enters the post-condenser to remove any additional heat, depending on the setting of the pre-condenser and test-section, such that the outlet of the post-condenser reaches saturation. The post-condenser is followed by a sub-cooler to ensure that sub-cooled liquid enters the coriolis flow meter to measure the flow of refrigerant in the test line.

3.2 Test Facility

Both the test line and bypass line have electronic expansion valves (EEVs). The test line valve is used to set the mass flow through the test section and the bypass expansion valve can then correct the system pressure in the test line. To cater for large flow ranges, two expansion valves are connected in parallel in both the test line and bypass line. These expansion valves are connected one at a time while the other is shut off and closed. In the test line a large Carel E²V EEV014 is used with a smaller Carel E²V EEV009 to be used for accurate control at low mass fluxes. The bypass line expansion valve is then selected according to the selected test line expansion valve, either a Carel E²V EEV024 or Carel E²V EEV014. The expansion valves are bi-directional, although this function will not be used.

The refrigerant lines join after the expansion valves and enter the evaporator. The evaporator is designed with capacity for the maximum demand and will operate as the condenser when evaporation tests are done. The flow moves on after the evaporator into the suction accumulator and then into the compressor inlet.

Small sightglasses are positioned along the refrigerant line where necessary. There are sightglasses at the inlet to the coriolis flow meter, inlet and exit of the evaporator and after the bypass line expansion valve.

The system is currently usable with most common refrigerants and condensation tests are planned using R-22, R-134a and R-407C (over this study, and subsequent studies). The whole system, excluding only the compressor, is designed to withstand the high saturation pressures of R-410A. Provisions have been made for a high-pressure compressor to be installed in the system by leaving blanked-off pipes and space in the bench for such a compressor. The refrigerant lines, in and out of the compressors can be closed off with manual valves such that the operator can use the system with the correct compressor.

The system is reversible and as such this makes the required heat exchanger units named earlier dual-function. Thus the condensers would be evaporators and vice versa when evaporation tests are done. The pipe network is designed in such a way that the flow through the test sections is in the same direction for condensation and evaporation testing. This is done by controlling 29 valves throughout the system that would facilitate the reversal of function without reverse flow.

3.2.2 Water cycle

The water cycle consists of a hot and cold side. The majority of the water cycle systems are on a separate apparatus than the refrigerant cycle. The water is used to exchange heat with the refrigerant side at the condensers (cold water) and the evaporator (hot water). The supply is controlled by Honeywell-actuated valves and the required pressure head is supplied by Ebarra centrifugal pumps.

The water system is based on two insulated 5000 liter tanks. The two tanks share a 70 kW heating/50kW cooling heat pump and are thermostat-controlled between 13-17°C and 23-27°C respectively. The heat pump works in two modes; the first, the most efficient, is water to water, in which a vapour-compression cycle running R-22 is used to both heat up and cool down the two water flows. Further, if any of the two water tanks are on temperature, an alternate conditioning system is automatically switched to, in which the water flow is passed through a large radiator and over which air is forced by using fans. The size of the tanks, and the size of the heat pump allow the experimental setup to run indefinitely, due to the fact that it can maintain a relatively constant system inlet temperature, regardless of how much heat is being put in and out of the tanks.

The control bench is used as the connecting unit between the reservoirs and the test sections. The control units are each made up of a pump, flow meter and actuated valve. Figure 3.4 shows the flow meters, their transmitters and the servo-controlled valves on the control bench. Every heat exchanger on the refrigerant bench has a control unit. The control units are located on the control bench and on the refrigerant bench. The control bench is used to control the supply to the evaporator, sub-cooler and bypass heat exchanger (Figure 3.5) and it directs flow to the control units on the test bench. The control units on the test bench are for the pre-, test-section and post-condensers (Figure 3.6). Names used for the heat exchangers are for condensation experiments.

The basic control unit receives water from the reservoir and this gets pumped by a centrifugal pump through the heat exchangers. On the return, the water flow rate through the heat exchanger passes through a flow meter, either a coriolis flow meter or a Bürkert flow meter. The flow then enters the return line through a valve. The valves used are servo-actuated and control the flow through the heat

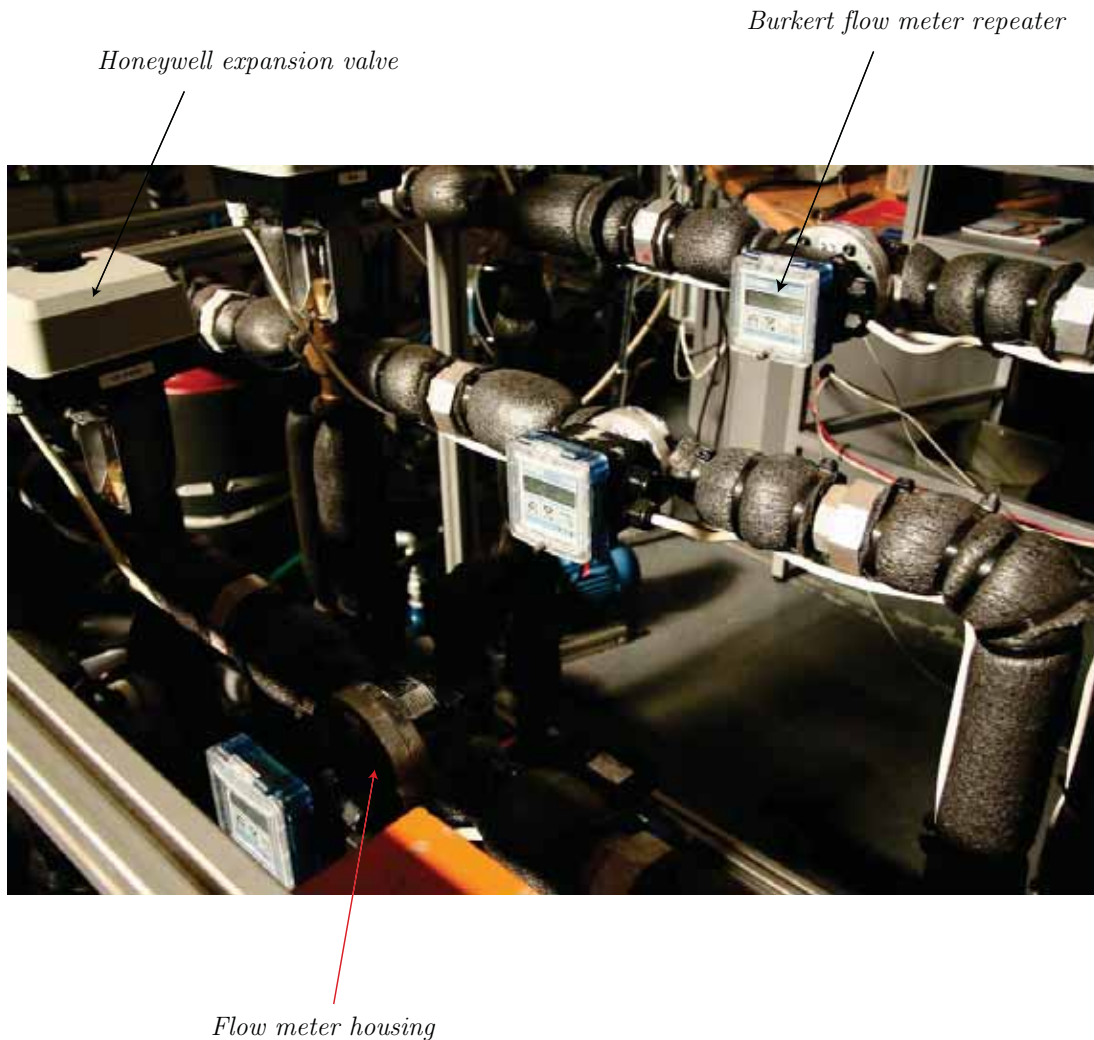


Figure 3.4: Control equipment on the water control bench

exchangers while the remaining flow bypass the heat exchanger and immediately enters the return line back to the reservoirs. Each control loop is designed for the correct flow range expected through the heat exchanger. The pre-condenser is made up of two parallel heat exchangers; the large one, is specified for 10 kW heating capacity, and would be used when testing at high mass fluxes. The smaller pre-condenser is specified for 2.5 kW heating capacity and is used for low mass flux tests. The flow meters used by the control loops depend on the accuracy that will be needed. Therefore the pre-condenser, test sections and

post-condenser are fitted with coriolis flow meters and the rest use a less accurate and cheaper Bürkert flow meter. The flow meters are sized according to flow requirements and heat exchanger size.

3.2.3 Instrumentation and data acquisition

The experimental setup, as described above, is completely monitored and controlled using a computer. Signals from the thermocouples, pressure transducers, mass flow meters, mixing valves, and expansion valves are collected by a computerized data acquisition system. Furthermore, this system is controlled using the monitored data mentioned previously, in conjunction with signals sent to both the expansion (current input) and the water-mixing (volt input) valves. The entire acquisition system is comprised of:

1. IBM compatible PC, running Windows XP Professional.
2. LabView[®] 8.0, a graphical data acquisition programming language (National Instruments, 2006). A LabView program was written to perform manual/automatic system control, as well as automatic data acquisition (Section 3.3).
3. One NI SCXI-1001 12-slot chassis (Signal Conditioning eXtensions for Instrumentation).
4. One NI SCXI-1600, USB Data Acquisition and Control module for the SCXI-1001. It allows for 200 kS/s on a single channel, and can multiplex 1 kS/s on multiple channels.
5. Four (4) NI SCXI-1102 32-channel thermocouple amplifiers. These are the signal conditioning modules for thermocouples and low-bandwidth millivolt, volt and current inputs.
6. Three (3) NI SCXI-1303 32-channel Isothermal terminal blocks. These connect thermocouples and signals to two of the SCXI-1102 modules. Eighty four (84) of the available ninety-six (96) channels are utilized for measuring thermocouple readings. The remaining twelve (12) channels may be utilized at a later stage.

3.2 Test Facility

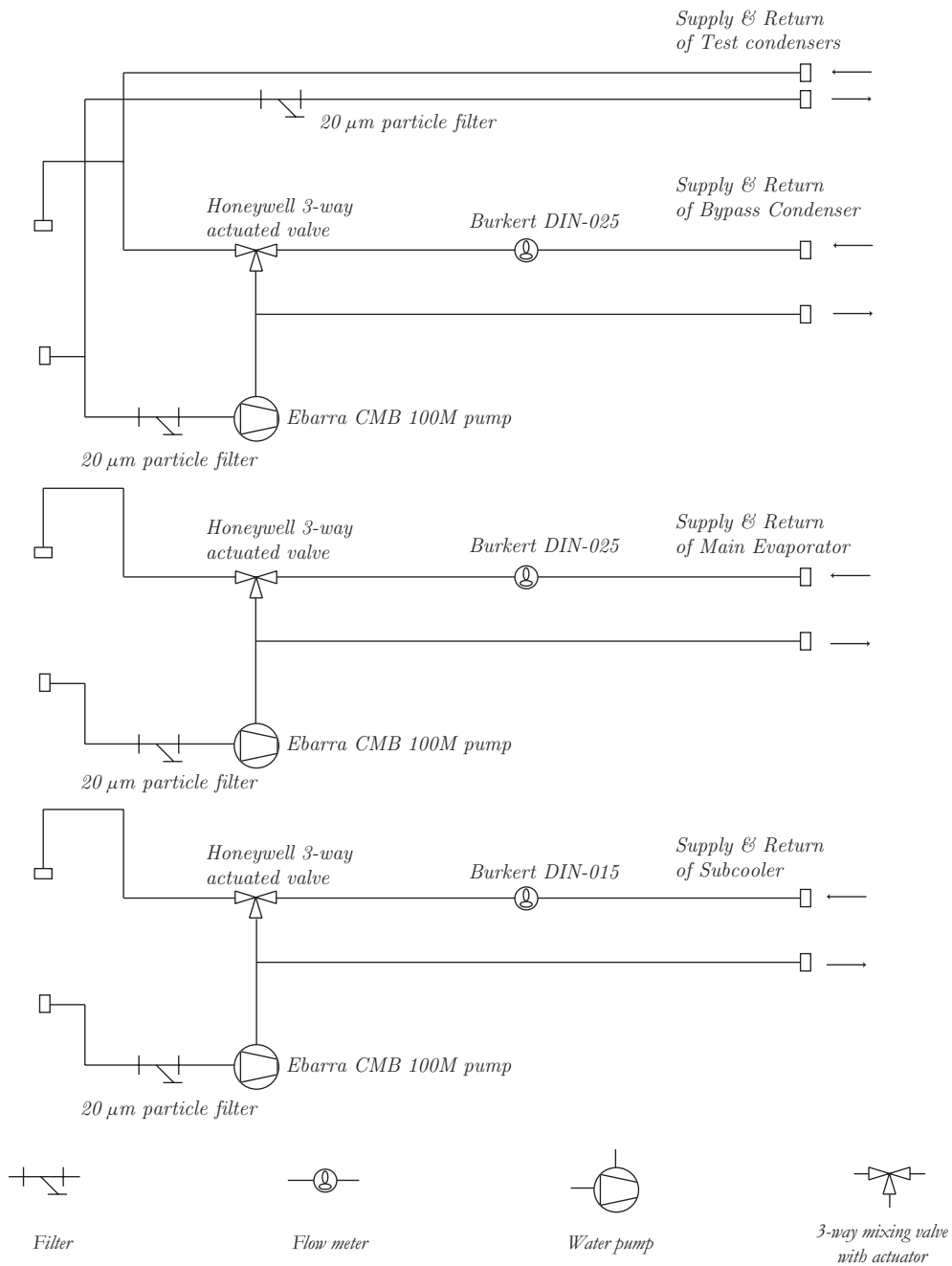


Figure 3.5: Control bench water pipe layout

- One (1) NI SCXI-1308 32-channel current input terminal block. It connects 0-20 mA and 4-20 mA signals to one of the SCXI-1102 modules. Fourteen

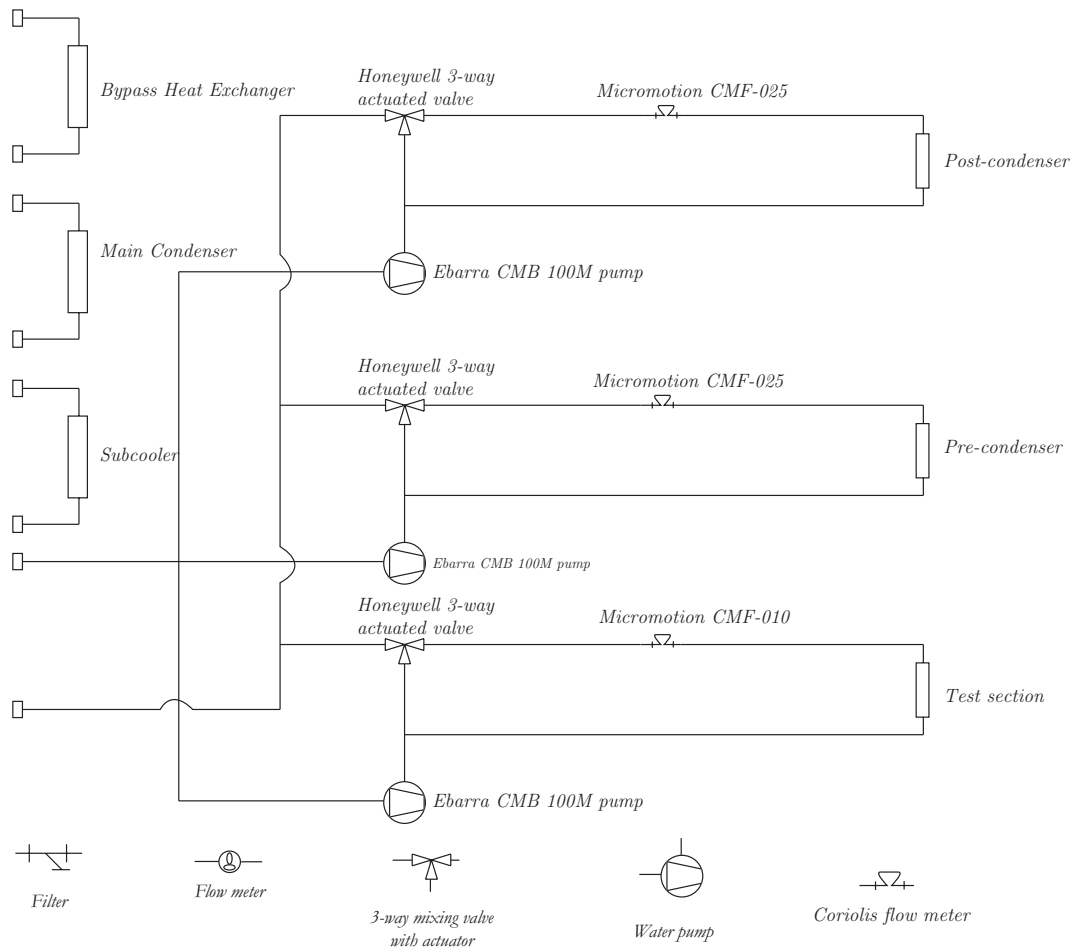


Figure 3.6: Water cycle layout on the refrigerant test bench

(14) of the available channels are utilized for the pressure transducer and mass flow meter signals.

8. Two (2) NI SCXI-1124 6-channel isolated analog output modules. These are capable of supplying 0-10 V and 0-20 mA control signals. They are utilized to control the Honeywell mixing valves, and the Carel expansion valves.
9. Two (2) NI SCXI-1325 terminal blocks. These are used with the SCXI-1124 modules, and are utilized to send the generated current/volt signal. One (1) of the two terminal blocks is fully utilized to control the six (6) water

Honeywell mixing valves, using a 2-10 V signal, while in the other terminal block, only two 4-20 mA current signals are generated, to control the test-line and bypass-line expansion valves. There are four slots remaining, which may be used in the case of any expansion of the system.

10. One (1) NI SCXI-1322 terminal block. It measures $\pm 40V$ input signals, and connects to the SCXI-1122 module. Two (2) of the inputs are utilized; one measures voltages coming from the void fraction sensor, and the second input measures the DC voltage being produced from the AC/DC inverter, for use in the Sensotec pressure sensor ratiometric measurement system (more on this in Section 3.6).
11. One (1) NI SCXI-1122 6-channel voltage input module. It is used in conjunction with the SCXI-1322 terminal block.
12. One (1) NI PCI-8252 high-speed 1394a camera card; it couples with NI's Vision Development Module (Software) for both image processing and analysis, directly in Labview.
13. The high-speed camera in use is an 8-bit Basler A620f IEEE 1394a firewire camera capable of up to 300 frames per second, on a reduced Region of Interest¹ (ROI). It should be noted that there is a difference between the maximum video framerate and the shutter speed. The maximum shutter speed (which is only a function of available light) is $10'000^{th}$ of a second. The camera is used in conjunction with the National Instruments Vision Development module image software that allows saving and post-processing of the video images. The software is also used to trigger the start of a capture. The backlight used is a 98.7% uniform, 50 by 50 mm red LED light made by Phlox in France. It emits low heat and does not influence the refrigerant flow like an incandescent light would. The lens utilized is a μ -Tron FV2520. Details are shown in Table 3.1.

¹The region of interest is defined as the picture size (in pixels) that is presented to the user. The smaller this is, the greater the videography speed can be. At full size (640 x 480 pixels), the camera can sustain 100 frames per second videography. At a reduced ROI of 100 x 100 pixels, the camera can save video at 300 frames per second.

3.3 Labview and the Labview program

14. The void fraction sensor used is under development at the University of Gent in Belgium. It is a capacitive void fraction sensor using six electrodes, four for shielding and two for sensing. The weak signal is amplified by an electronics circuit for measurement with the NI DAQ. The voltage output varies from one to ten volts and can be sampled at any frequency less than 1000 Hz.

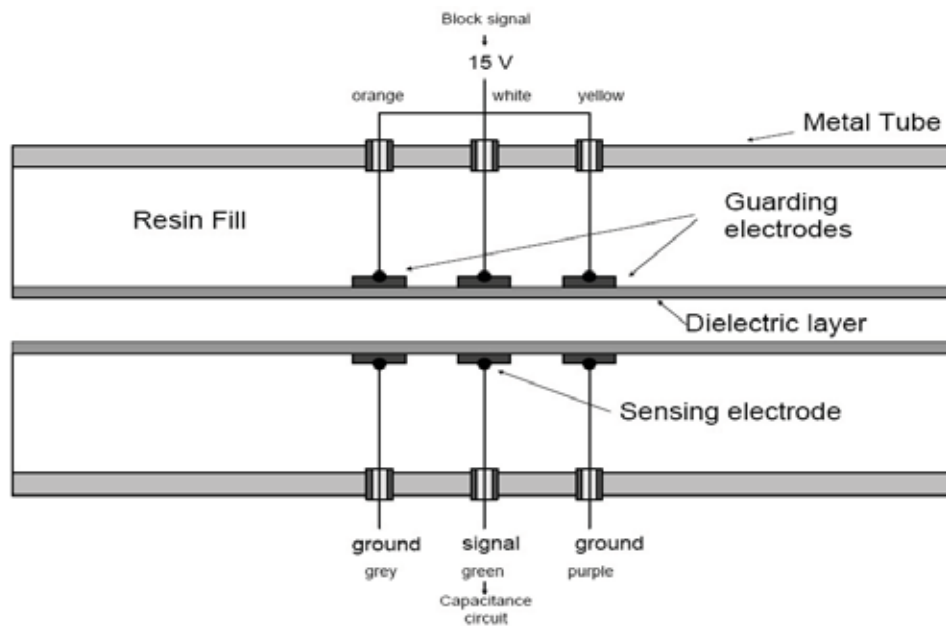


Figure 3.7: Diagram of void fraction sensor provided by UGent

3.3 Labview and the Labview program

The experimental setup is comprised of the components and systems as set out in Section 3.2.1. The software backbone of the experimental setup, developed in National Instruments' *Labview*, utilizes both inputs received from sensors, and outputs sent to controllable operating systems to achieve data acquisition and manual/automatic control.

3.3 Labview and the Labview program

Table 3.1: Equipment utilized by the Labview software backbone in the two-phase experimental setup

Quantity	Equipment	Range
Temperature	Type T thermocouple wire <i>Omega</i> , UK, 30-gauge	-30 – 300°C
Pressure Sensors		
<i>Low</i>	<i>Gems Sensor</i> , UK,	0 – 2000 kPa
<i>High</i>	<i>Gems Sensor</i> , UK	0 – 4000 kPa
<i>Test</i>	FP2000, <i>Sensotec</i> , USA	0 – 3400 kPa
Mass flow rate		
<i>Water</i>	Coriolis flow meter: <i>Micro Motion Inc.</i> , USA	CMF 010 (0.4 kg/s) CMF 025 (0.6 kg/s)
<i>Refrigerant</i>	Coriolis flow meter: <i>Micro Motion Inc.</i> , USA	CMF 010 (0.4 kg/s)
<i>Water</i>	Flow meter: DIN025,015 <i>Bürkert</i> , Germany	DIN025 (1.8 kg/s) DIN015 (0.6 kg/s)
Expansion valves		
<i>Test line</i>	<i>Carel E²V-014</i> <i>Carel E²V-009</i>	4-20 mA input 4-20 mA input
<i>Bypass line</i>	<i>Carel E²V-024</i> <i>Carel E²V-014</i> Italy	4-20 mA input 4-20 mA input
Data acquisition	<i>National Instruments</i> , USA	
<i>Temperature</i>	SCXI-1102 32-Channel multiplexer	±10 V, 4-20 mA inputs 250 kS/s single channel sampling rate
<i>Pressure and Mass flow</i>	SCXI-1102 32-Channel multiplexer	±10 V, 4-20 mA inputs 250 kS/s single channel sampling rate
<i>Control</i>	SCXI-1124 6-Channel low-bandwidth output module	±10 V, 0-20 mA outputs
<i>Void Fraction</i>	SXCI-1327 8-Channel analog voltage input	±40 V inputs
Flow visualization		

Continued on next page

3.3 Labview and the Labview program

Table 3.1 – continued from previous page

Quantity	Equipment	Range
<i>Camera</i>	<i>Basler A602f</i> high-speed camera	Up to $\frac{1}{10'000}$ th s aperture time dependent on ROI
<i>Lens</i>	<i>μTron FV2520</i>	25 mm, f/2 lens
<i>Backlight</i>	<i>Phlox</i> 50 mm x 50mm red LED backlight	98.7% even lighting

The main LabView VI (Virtual Instrument) performs both the control and data acquisition operations required. As shown in Figure 3.8, the program is divided into several 'tabs'; each one of these is utilized to show the salient information contained within each 'subsection'. What is more, there are several data which are not placed inside tabs; due to the fact that they are, in general, in continuous use, they have been placed off to the left of the tabbed section. These include the refrigerant in use, the water and refrigerant mass flow rates (the refrigerant mass flow rate includes the mass flux - 'G', its most common notations), salient temperatures in both the refrigerant and the water lines, and the pressures at several points in the system. The tabbed section comprises of 7 tabs; In no particular order, these are:

Control This tab is the manual control tab; both the expansion valves and the water mixing valves are controlled from here. As was stated in Section 3.2.1, although there are two expansion valves per line, only one is used at a time, depending on what the required test conditions are. As such, there is physically only one control signal going to each line, and the required EEV is selected by manually installing the connector to the correct EEV, and opening the necessary valves. In the control tab, two inputs are available, which will directly accept inputs from 4-20 mA, and actuate the expansion valves. It is also possible to change that 4-20 mA required input to an input varying from 0-1, indicating 'fraction opening' (where 1 is fully open). The conversion to required input happens automatically in the background. The theory behind the control aspect of the EEV movements is detailed later, in section 3.5. On the bottom half of the 'Control' tab is the section controlling the actuation and fraction-opening of all the Honeywell water

3.3 Labview and the Labview program

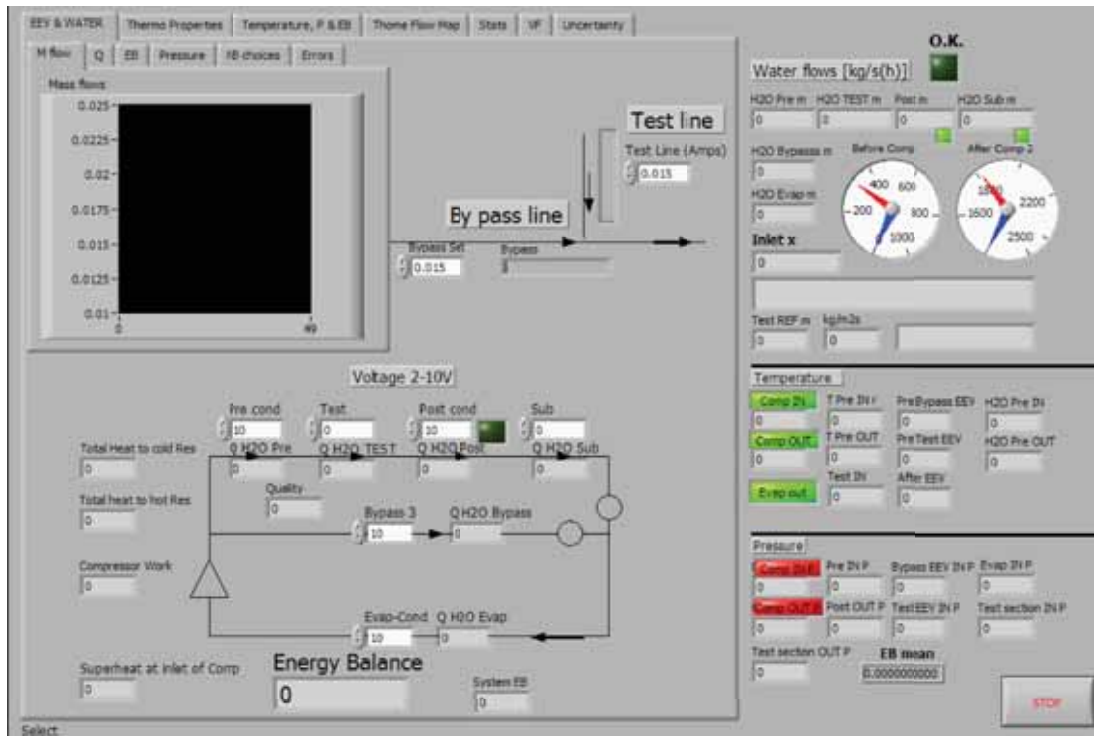


Figure 3.8: Front panel of the LabVIEW program

mixing valves. Section 3.2.1 gives a brief explanation of the workings of the mixing valves. These valves are controlled using a 2-10 V signal; it is stated that these valves have fully-continuous actuation, meaning that they, in theory, do not move on step input signals. However, it has been seen that the lowest repeatable input signal change that will register, and make the valves operate, is 0.2 V. It should be noted that the 4 mA and 2 V signals correspond to the valves being fully closed, while 20 mA and 10 V represent the valves fully open. An indicator at the bottom of the tab shows the amount of superheat available at the inlet of the compressor, which is calculated using a Matlab script. This is utilized in the control of the system, as set out in section 3.5. Furthermore, indicators showing the compressor work, test energy balance and system energy balance are also shown. What is more, a sub-menu is available in this tab; a running history of the mass flows, heat transfer (hot and cold sides) and energy balance are available, along with a tab that lets the user make important choices, such

3.3 Labview and the Labview program

as the inner diameter of the tube, heat exchanger length and conductivity of the copper. A final tab controls the error indicators, which are aural in nature and notify the user if any system parameters falls over or runs over the specified safety limits. The 'Save' tab is used to manually specify the file name convention, and the directory used for saving, as well as the number of samples to capture per saved data point.

Void Fraction The void fraction tab essentially runs the Void Fraction sub-VI, and shows the two most important graphs generated by the sensor. The sensor utilized is a capacitive void fraction sensor, which uses three electrodes to pick up the difference in vapour/liquid dielectric constant and generates a voltage signal (De Paepe *et al.*, 2006). A toggle switch is utilized to activate the Void Fraction sub-VI, while two outputs of the sub-VI, the power spectral density (PSD) graph of the voltage signal and the Void fraction statistical graph are output to the main control program for monitoring purposes. The statistical value of the void fraction sensor's signal is compared to the logarithmic-mean void fraction prediction and the percentage deviation is calculated.

Thermodynamic Properties This tab utilizes pressure and temperature data, coupled to the Matlab script to generate two graphs, the first, a T-s diagram, and the second, a P-h diagram. While these are not of direct influence, or importance, to two-phase testing and experimentation, it is useful from a system-control point of view, as it is possible, in one quick glance, to summarize the complete operating window, instead of having to check each point separately. The method utilized to generate these graphs is detailed in section 3.4.

Temperature, Pressure and Energy Balance This tab includes all of the temperature and pressure measurements that are found in the system, both on the refrigerant and the water sides. Also, several energy balances are calculated in this tab. Furthermore, several key control aspects are also shown here, as are the amount of superheat available at the inlet of the compressor (also shown in the "Water & EEV" tab), the condensation temperature

3.3 Labview and the Labview program

at the test pressure, and the refrigerant states at the temperatures. Furthermore, in terms of pressure, the experimental system has an operating range from 300 kPa up to 2500 kPa (at the moment; once R410a is used, the HP trip pressure will have to be increased up to at least 3800 kPa (de Vos, 2005)). Warning systems, which include sonic and visual alarms, notify the user when the low-pressure (*i.e.* in front of the compressor), the high-pressure (right after the condenser) or any of the temperatures (*i.e.* compressor inlet temperature $< 0^{\circ}\text{C}$, or compressor outlet $> 100^{\circ}\text{C}$) in the system fall out of their adequate range. While it has not been previously stated, the control program is heavily dependent on a Matlab script to calculate refrigerant and water properties, refrigerant quality and heat transferred (Q). This will be detailed in section 3.4. Using experimentally calculated values for the heat transferred to and from the pre-, test- and post-condensers (in Condensation mode), both on the refrigerant side and water side, an overall test energy balance is calculated. For the purposes of any studies performed at UP's thermoflow research group, the energy balance must be less than 1%. It should be noticed that the total refrigerant mass flow is not measured (*i.e.* through the compressor), nor is the bypass line mass flow, as they are, for purposes of testing, irrelevant. Nonetheless, using several well-based assumptions (shown in section 3.4), it is possible to estimate the mass flow through the compressor. Using this approximated mass flow, the work input to the compressor, and the total energy input into the main evaporator can be approximated. These are also shown in this tab. The system energy balance is calculated by checking the amount of energy in and out of the refrigerant system; that is, a control volume over the entire system allows us to equate energy out of the system (in the condensers) to the sum of the work input in the compressor and the thermal energy input in the main evaporator.

Thome flow map The method used to construct this flow map is as found in El Hajal *et al.* (2003). It is generated using a Matlab script, and is used to theoretically confirm the flow regime found in the sightglass during experimentation. The Rouhani-Axelsson void fraction and the LMTD void

fraction are both calculated, and indicators are included in the Void Fraction tab as comparison values. The flow-regime based heat transfer coefficient and pressure drop prediction are automatically updated and presented in this section.

Stats Stemming from the fact that there are several key data that need to stabilize for useful testing to commence, the behavior of these is studied on a time basis, in the sense that the standard deviation about the point's mean value is calculated over 30 iterations of the main program's `while` loop. The mean is also updated at each iteration, such that the deviation comparison occurs in real-time. Information in this section includes temperatures, pressures, mass flows and void fraction signals.

Uncertainties The uncertainties in the system, as derived in Appendix A were included into a separate Matlab script that runs continuously in the program. It takes the measurements made in the system and continuously calculates the uncertainties in the system. This information is also saved when saving data. This tab can be utilized to decide in real-time whether the uncertainties are within tolerances to begin testing, or whether changes are required. These could be from an instrumentation point of view, or from a testing point point of view.

3.4 Matlab script

3.4.1 Thermodynamic properties

As has been stated previously, the Matlab script running the Control VI is critical to the control, data acquisition and monitoring aspects of the experimental system. At present, Matlab R15 (Matlab R15, Reading, MA) is used. The major component of the Matlab script involves finding the properties of both the water and refrigerant at the required measuring points. This is done using XPROPS, a suite of Microsoft Excel, Labview and Matlab functions, developed by Thermal Analysis Partners (Thermal Analysis Partner XPROPS, University of Maryland,

MD), which make reference to NIST's REFPROP 7 (National Institute of Standards and Technology, 2002) fluid property database. Thermal Analysis Partners is fully endorsed by NIST in its endeavors. XPROPS Matlab property functions are called using the required inputs to generate the desired fluid properties.

Due to the fact that the temperature and pressure stay constant during condensation and evaporation, additional information is required to calculate the temperature and pressure before and after the test section. This is done by assuming that the entirety of the energy transferred into the water goes out of the refrigerant (which is an acceptable assumption once the test line energy balance drops below 1%), and knowing what the properties of the refrigerant are at the inlet of the pre-condenser. However, one cannot always assume that the outlet of the precondenser is in the mixed regime, thus for generality purposes, a case structure must be utilized, using `if` statements in the Matlab script. With the known properties of the refrigerant at the inlet of the precondenser, two extra energy quantities are calculated:

1. Q_{satvap} This is the amount of energy required to make the outlet of the precondenser go to the saturated vapour point at the pressure and temperature measured at the inlet of the test section.
2. Q_{satliq} This is the amount of energy required to make the outlet of the precondenser go to the saturated liquid point at the pressure and temperature measured at the inlet of the test section.

As such we can easily surmise that there will be three possible cases; first, the inlet of the test section is fully-liquid, second, in the mixed regime, and third, still superheated. This is shown in Figure 3.9. The first and third cases are not of large concern, as the properties of the refrigerant can be simply garnered from the pressure and temperature at the point. However, for the mixed regime, it is necessary to know what the quality is, such that the relevant properties may be found. In this case, though, it is necessary to first calculate the enthalpy of the outlet of the outlet of the precondenser, using:

$$h_{ref,pcout} = h_{ref,pcin} - \left| \frac{\dot{Q}_{H_2O,pre}}{\dot{m}_{ref}} \right| \quad (3.1)$$

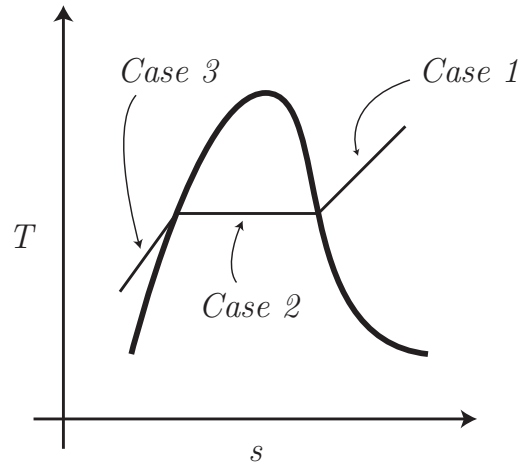


Figure 3.9: Refrigerant pre-condenser outlet possibilities

where $h_{ref,i}$ is the specific enthalpy of the refrigerant at the inlet and outlet of the precondenser. Once the precondenser outlet enthalpy is known, this is equal to the enthalpy at the inlet of the test section. Then, knowing what the enthalpy at the inlet of the test section is, the saturation liquid and vapour enthalpies at the condensing temperature and pressure of the inlet of the test section are called up, to calculate the quality at the inlet:

$$x_{test,in} = \frac{h_{ref,testin}}{h_{ref,satvap} - h_{ref,satliq}} \quad (3.2)$$

To calculate the test outlet properties, a three-tiered approach is also used; depending on what the test inlet looks like, additional steps are performed. When the inlet of the test section is fully-liquid, it stands to reason that the exit can only be liquid as well, thus the temperature and pressure are utilized to calculate the properties of the refrigerant at the exit. When the inlet regime is mixed, the amount of energy required to drop to fully saturated liquid at the exit temperature and pressure conditions is calculated. Then a two-level condition structure is utilized to calculate the properties at the outlet. When the inlet remains superheated, the same conditional structure used in the pre-condenser must be utilized.

3.4 Matlab script

The rest of the system refrigerant points can be directly calculated using XProps, and the refrigerant temperature and pressure, except for one point. After the expansion valves, the point at the lower temperature is almost certainly mixed, but without any other information other than pressure and temperature, one cannot know exactly where it is. Nonetheless, since this is not a critical point, and is only calculated for the sake of completeness, and to complete the cycle in the "Thermodynamic" tab, there are several assumptions one can make. First, it may be assumed that there is no heat loss over the expansion valve, nor is there any work done on, or by, the fluid. Furthermore, the mass flow stays constant over each expansion valve. As such, over each expansion valve,

$$h_{ref,EEV\ in} = h_{ref,EEV\ out} \quad (3.3)$$

And, when the bypass and test lines meet,

$$\dot{m}_{ref,test}h_{ref,test} + \dot{m}_{ref,bypass}h_{ref,bypass} = \dot{m}_{ref,tot}h_{ref,tot} \quad (3.4)$$

However, both $\dot{m}_{ref,bypass}$ and $\dot{m}_{ref,tot}$ are unknown. The mass flow of refrigerant through the bypass line may however be approximated by assuming that the pressure at the inlet of the bypass-condenser (which is not measured), is equal to the pressure at the inlet of the pre-condenser. It is also assumed that the bypass heat exchanger's inlet is superheated. Thus, by using the measured temperature and the assumed pressure, a specific enthalpy for the refrigerant at the inlet of the bypass-condenser can be approximated. Then, using the known quantity of heat transferred into the water side of the bypass-condenser (assuming very good energy balances), and the known outlet state, an approximate refrigerant bypass mass flow can be found,

$$\dot{m}_{ref,bypass} = \left| \frac{\dot{Q}_{H_2O,bypass}}{h_{ref,bin} - h_{ref,bout}} \right| \quad (3.5)$$

With this approximated bypass refrigerant mass flow, the total mass flow can be shown to be:

$$\dot{m}_{ref,tot} = \dot{m}_{ref,bypass} + \dot{m}_{ref,test} \quad (3.6)$$

And, finally knowing the above, the specific enthalpy at the exit of the mixing chamber, located after the EEVs is

$$h_{ref,tot} = \frac{(\dot{m}_{ref,test}h_{ref,test}) + (\dot{m}_{ref,bypass}h_{ref,bypass})}{\dot{m}_{ref,tot}} \quad (3.7)$$

With this final point, it is possible to calculate the quality using the pressure at the point and the specific enthalpy. Finally, the entire cycle may be graphed, as in the 'Thermodynamic Properties' tab.

To estimate the real mass flow through the main and bypass lines, it is assumed that the main evaporator has a good enough energy balance such that the energy transferred into the refrigerant can be assumed to come only from the water. As such, if we calculate the energy transferred, we can work back to a refrigerant mass flow, since we have assumed that the inlet enthalpy into the evaporator is reasonably accurate as calculated above. Thus,

$$\dot{m}_{ref,tot} = \left| \frac{\dot{Q}_{H_2O,evap}}{h_{ref,evapout} - h_{ref,evapin}} \right| \quad (3.8)$$

3.4.2 Energy balance

The test-line energy balance must be calculated to make sure that, first of all, the assumptions made in the previous section are valid (*viz* the quality calculation), and second, to make sure there is no stray energy lost in the system. The system energy balance consists of comparing the total test-line energy transferred between the refrigerant and test sections, inside the pre-, test- and post-condensers. The equation for the system energy balance is:

$$EB_{sys}(\%) = \left| \frac{\dot{Q}_{ref} - \dot{Q}_{H_2O}}{\dot{Q}_{avg}} \right| \cdot 100 \quad (3.9)$$

where Q_{avg} is the mean of the absolute values of the experimentally found values for the heat transferred to and from the refrigerant test line, on both the refrigerant and water side.

3.4.3 Thome flow map

The Thome flow map, as stated beforehand is automatically calculated utilizing the most up-to-date inputs from the rest of the system, including the prevalent mass flux inside the test section, and the temperature at the test point. Utilizing these, and using a `for` loop, the entire flow map can be generated in realtime, with changing conditions reflected automatically. As stated in Section 3.2.1, two sight glasses, one each in front and back of the test-condenser, are installed. Due to the potential difference in quality between the inlet and outlet, these two points are plotted; a third point, using a linear average of the two condition qualities is also plotted. This vapour quality is the average quality used in the flow map and heat transfer. Again, this flow map is utilized to corroborate the experimental findings, and to troubleshoot the system.

3.5 Control methodology

As has been shown previously, there are a multitude of factors and settings which can be changed in the system which will affect the working pressure P , mass flux ϕ and test inlet quality x . Coincidentally, these are the three main areas which must be controlled in this setup to successfully carry out valid and meaningful experiments. However, changing one factor does not necessarily mean only one of these three main parameters change; in most cases, altering any one factor will have an effect on more than one of the three critical parameter.

As was previously stated, it is necessary to be able to control the working pressure, mass flux and test inlet/outlet vapour qualities. The methodology for this is stated in the following sections.

Due to the complex relation between the multiple parameters that affect the three main test criteria, automating the system is a non-trivial procedure. While this was begun during this study, as a part of both the author's work and Van Rooyen's work, it was not finalized. As such, any control performed in this system is still manual.

3.5.1 Mass flux control

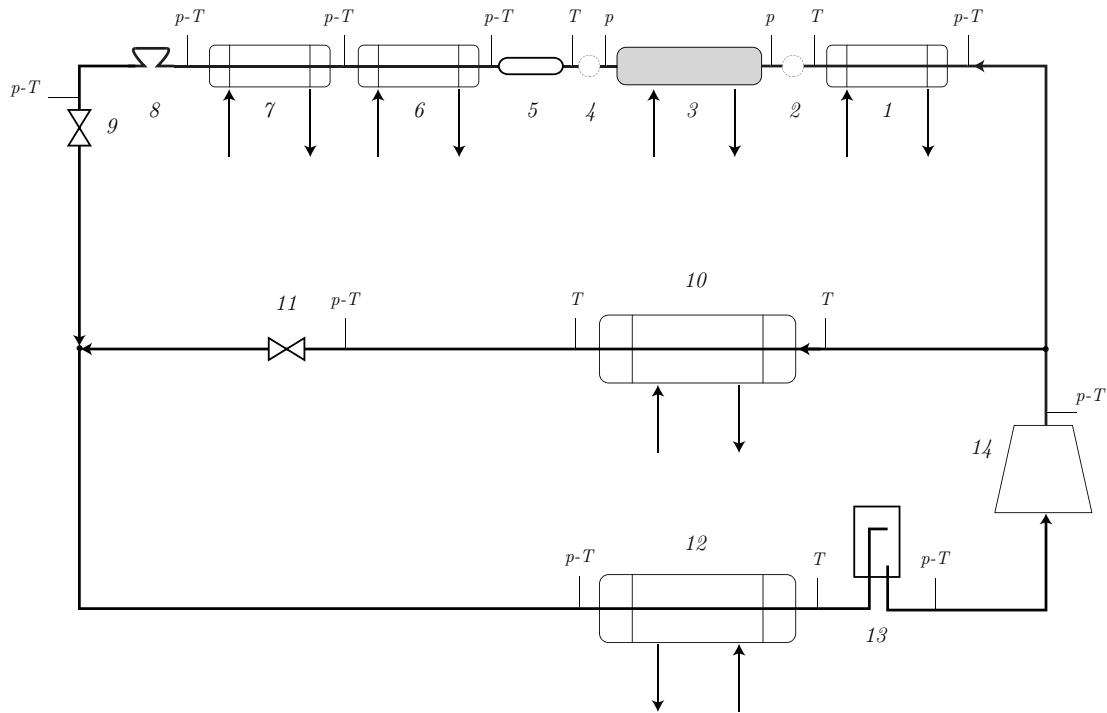
To control the test line mass flux, the amount of refrigerant bypassed or let into the test line needs to be changed. In this case, as shown in Figure 3.10, this can be done using the test line expansion valve. By opening and closing the expansion valve, the general backpressure on the line changes, which means that more, or less flow will be diverted to the bypass line, depending on the action taken.

With the Carel expansion valves that are currently installed on the test-line, it is possible to test from 25 up to 1000 $\frac{kg}{m^2s}$. Under 150 $\frac{kg}{m^2s}$, the E²V-009 should be utilized as it affords accuracy of up to $\pm 1 \frac{kg}{m^2s}$, with relatively small changes between valve settings. The E²V-014 should be utilized when in higher mass flux situations; once the system has stabilized, it has been shown that the variations over and below the required mass flux can be kept at $\pm 1 \frac{kg}{m^2s}$. The methodology for control of mass flux would involve, firstly, setting the required mass flux and adjusting the test-line EEV to achieve said flux. Since the actuation of the test-line EEV will have an effect on the system pressure, the pressure will need to be controlled. In all cases, any changes made to the system parameters require adequate settling time.

3.5.2 Test line pressure control

Due to the fact that the test-line expansion valve settings change to accommodate the mass flux requirement, the backpressure increases and decreases which cause the change in mass flux to also have an influence on the system pressure. To control the pressure, there are several methods that can be utilized; namely the modification of the bypass line expansion valve setting. Further, to achieve the correct condensation pressure in the system, the bypass expansion valve is also opened and closed as is necessary. Thus, when the condensing pressure needs to be increased, the bypass EEV should be closed. To achieve the same effect, the bypass condenser water can also be used. That is, to increase the testing saturation pressure, the water flow through the condenser should be slightly dropped. The converse is also true. From experimentation, the system is more sensitive to small water flow changes than to medium changes in the EEV setting. As such, the water flow should be used for approximate settings, with the EEV used for

3.5 Control methodology



1. Pre-condenser (water cooled)
2. Sight glass: high-speed videography
3. Test section (water cooled)
4. Sight glass
5. Capacitive void fraction sensor
6. Post-condenser (water cooled)
7. Sub-cooler (water cooled)
8. Coriolis mass flow meter
9. Test line expansion valve
10. Bypass condenser (water cooled)
11. Bypass line expansion valve
12. Evaporator (water cooled)
13. Suction Accumulator
14. Compressor

Figure 3.10: Schematic of the system cycle

precision control. Larger changes will affect the pressure in the system greatly, and should be avoided. As a last resort, if the system is in danger of tripping the HP (high pressure) switch, the bypass condenser water supply should be opened a large amount. This immediately drops the pressure. If the system is in danger of tripping the LP (low pressure), the bypass EEV should be closed and so

3.6 Sensotec FP2000 ratiometric measurements

should the bypass condenser water flow. While the test-line mass flux is quite insensitive to changes performed in the bypass EEV, it is not entirely so, which entails further small corrections.

3.5.3 Test inlet and outlet vapour quality control

The vapour quality of the refrigerant before and after the test section must be finely controlled, as the overall test quality is defined as the average between the inlet and outlet of the test section. As such, depending on what is required, the amount of heat taken out of the system needs to be controllable. As was stated in section 3.4, this is done by controlling the water mass flow rate through the pre-condenser. The method utilized requires monitoring the properties of the refrigerant at the inlet of both the pre- and the test-condenser. If the desired test inlet quality is known, then the Matlab script can calculate how much energy to take out from the refrigerant. Then, not taking into account the water outlet temperature change, it is possible to calculate the water mass flow required. Finally, the water inlet mixing valve can be opened or closed, depending on the amount of water necessary. The same procedure should be followed in the test section. It should be noted that the refrigerant must be in fully-liquid state at the exit of the post-condenser. This can be manually ensured by using indicators and alarms showing the state at the exit of the post-condenser — it can also be automatically controlled — there is a pressure transducer at the exit of the post-condenser, from which it is possible, using Xprops and Matlab, to find the saturation temperature at that pressure. Then, since the temperature of the refrigerant is also monitored, the water mass flow rate should be controlled such that the temperature at the exit of the post-condenser is always less than the calculated saturation temperature.

3.6 Sensotec FP2000 ratiometric measurements

The output of a strain gauge based sensor is directly proportional to the physical pressure measurement the sensor is detecting and also the excitation voltage

3.7 Experimental Procedure

across the bridge network. The full scale output of the transducer varies directly with the excitation thus, a sensor with a calibration factor of 3 mV/V will exhibit 30 mV at full pressure if it is being supplied with 10 V, but only 15 mV at full pressure if it is being supplied with 5 V (Manual, Columbus, OH). This means that output varies with supply voltage. If the effect of the change in supply voltage cannot be perceived, then it is not truly possible to know how much the real pressure has changed. This approach is known as a ratio metric measurement because it relies on the ratio of voltage output to the calibration factor (mV/V) to determine pressure. Sensotec pressure sensors require the user to monitor both transducer output and power supply excitation (rather than being voltage-independent). Using the mV/V calibration constant given in the pressure sensors' factory calibration certificates, it is possible to redefine the output of the system such that, independent of incoming supply voltage, the milli-ampere output varies between 4-20 mA between 0-3447 kPa, using an independent pressure calculation sub-VI in the control VI.

3.7 Experimental Procedure

To start the experimental setup, and to make sure there are no leaks, the system needs to be pumped up with nitrogen to 1500 kPa; once at this pressure, it must be kept there for at least 24 hours. If no pressure drop occurs, the system can be said to be leak-tight.

To evacuate the system of the nitrogen, the system must be evacuated (without use of a vacuum pump) until the internal pressure is not much higher than ambient pressure. This is due to the fact that, at higher internal pressures, the vacuum pump oil can be driven out, potentially causing large amounts of damage to the pump. In Liebenberg (2002), a system charged with 4 kilograms of R-22 was evacuated for 6 hours; in the case of this system, 13 kilograms constitute a full system charge. Thus, from linear extrapolation, the system needs to be evacuated for a minimum of 18 hours.

Of course, this is done only when changing refrigerants. If only the test section is to be replaced, the test section area is evacuated using the vacuum pump,

3.7 Experimental Procedure

charged with nitrogen and pressure tested. Once the system can be considered leak proof, it is charged with the proper refrigerant and testing can continue.

Once the system is charged, a minimum compressor warm-up time of eight hours is required, such that the crank-case heater ensures the refrigerant entrance to the compressor is fully superheated. For this reason, the crank case heater should always be on. Then, once the system is ready to be started, it is necessary to check that the water supply temperatures are within tolerances. In the case of the cold water supply, the water temperature should be between 13-17°C, while the hot water temperature should be between 23-27°C.

To start up the system, the hot and cold water supply lines need to be fully opened at the control-bench distributor. Then, the control pumps for all six heat exchangers can be turned on. The compressor has a safety feature, which does not let it start up if any of the pumps are not working correctly. Once the mixing valves and the expansion valves are set to their midway points, the compressor can be turned on.

After a 10-20 minute stabilization period, it is possible to make modifications to the system's controllable parameters such that the first testing point can be reached. Once the system is allowed to stabilize (i.e. the test-line energy balance < 1% for more than 5 minutes), data collection can commence.

As has been pointed out previously, the sight glasses are utilized as buffers against axial conduction in the system. Furthermore, just before the sight glass at the entrance to the test section, and straight after the sight glass at the exit of the test section, thermocouples and pressures are measured as shown in figure 3.11.

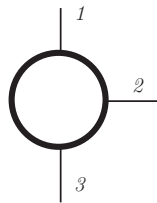


Figure 3.11: Pressure sensor and thermocouple placement at the inlet and outlet of the test section (1.: Top position, 2.: Side position, 3.: Bottom position)

The inside wall temperatures of the refrigerant line can be measured using direct measurements, or can be inferred using the Wilson-plot method.

3.7 Experimental Procedure

Apart from thermocouple and pressure measurements, the calculated overall and semi-local heat transfer coefficients, as dynamically calculated in the Matlab program are saved. The general list of raw data saved is as follows:

1. Thermocouple readings (placement as shown in the figure) at the inlet and outlet of the test section. These readings are utilized by themselves and in averaged form.
2. Thermocouple readings along the outer diameter of the inner tube.
3. Pressure transducer readings (placement as shown in the figure) at the inlet and outlet of the test section. These are also used by themselves and in averaged form.
4. Calculated momentum pressure drop readings.
5. Raw void fraction voltage, as well as the PDF and statistically-separated bin void fraction measurement.
6. Overall and semi-local heat transfer coefficients.
7. Mass flux, and inlet and outlet qualities.
8. Heat transfer rates, on both water and refrigerant sides.
9. High-speed video images.

In terms of data reduction, the following is needed for the heat transfer and pressure drop correlation:

1. A time-fraction map in the intermittent flow regime is generated using data processed from the high-speed camera videos.
2. When utilizing direct wall temperature measurements, the measured heat transferred on the annulus is divided into a unit heat flux and is propagated along the tube. Either way, this is utilized to calculate the inside heat transfer coefficients.

3. The time-fraction data is used in conjunction with the shear stress-based and gravity-based correlations of Thome, to develop a more general prediction for the intermittent flow regime.
4. The same type of regression analysis technique is also used for the pressure drop. In this case, the mass flux, inlet and outlet vapour qualities, and the fluid properties are required, among others.

The flow regime study involves using three methods of identifying flow regimes and comparing the results. The first method uses power spectral density analysis of pressure measurements to identify flow regime (Liebenberg, 2002). Secondly a capacitive void fraction measurement device will be used and by analyzing the frequency response of the signal a probability density of the current flow regime will be given. Thirdly by directly analyzing and manipulating the video feed from a high-speed camera in LabView and using IMAQ visual software a probability density of flow regime will again be constructed. The output of these three independent methods of flow regime identification will then be compared for conclusions to be made on the use of any of these methods. For modern heat transfer and pressure drop correlations the identification of flow regime plays an important part and finding an effective and accurate method with rapid results will aid in future development and improvement towards a unified approach.

Tests will be done at all the necessary points by setting the system, correcting the imbalance, waiting for stability and running the test. This procedure is repeated until complete.

3.8 Test section design

The test section is comprised of a horizontal straight tube-in-tube counterflow heat exchanger. Furthermore, just before and after the heat exchanger, sight glasses are positioned on the refrigerant side. At the exit of the back sight glass (*i.e.* the sight glass at the (refrigerant) exit of the heat exchanger) the void fraction sensor (De Paepe *et al.*, 2006) is positioned. Refrigerant flows in the inner tube, while water flows in the annulus. The entire test system is installed into the apparatus using flanges, such that the experimental apparatus need not

3.8 Test section design

be stopped and deconstructed to fit a new type of tube. The test section is shown in Figure 3.12.

The test tubes utilized all have an outer diameter of 9.55 mm, which is a standard size in refrigeration systems. The reason why tubes of this size were chosen was precisely because they are widely used in industry. The annulus outer tube has an outer diameter of 15.87 mm. It has one inlet and outlet for water to circulate in and out from, at the refrigerant outlet and inlet sides respectively.

Between the inlet flange and the inlet sight glass, a minimum distance of 50 internal diameters is required, for settling and flow development (Lienhard and Lienhard, 2005). In this case, the maximum length this will ever be is 450 mm; as such, this distance is used for any changing inner diameters. At the inlet of the inlet sight glass, several circumferential thermocouple readings are taken; these are the test section refrigerant inlet thermocouple readings. As has been previously stated, the thermocouple readings are taken before and after the sightglasses, as they serve the important role of breaking up the axial conduction through the walls of the inner tube, which have a potentially large effect on the read temperature. The first sight glass is fitted with the Phlox backlight and the Basler camera for high-speed videography purposes.

The sight glass construction is shown in Figure 3.13. The main housing is made out of brass and consists of two identical parts that are machined. On the interior face, four holes are drilled and tapped, to keep the retaining plate secure. Also, a housing for the U-seal is machined out. The main reason that U-seals were utilized in this application is for their self-energizing capabilities; the higher the pressure in the refrigerant system, the more the seal will tend to expand and seal against the housing and the boron silicate inner tube. The material used in the seals is Teflon. These seals, however, are not compression seals; they need a thin layer of oil on which to press down. By soaking them in oil for 20 hours before installing the seals, the sightglasses could be proven leak-tight.

Both the inner refrigerant glass tube, as well as the safety tube around the housing are made out of boron-silicate, chosen for its good clarity and exceptional strength. The housings have grooves cut into the outside to fit the O-rings against the safety glass. Further, the housings have a hole machined out of them, into which the tube coming and going from the rest of the system fit. The tube

3.8 Test section design

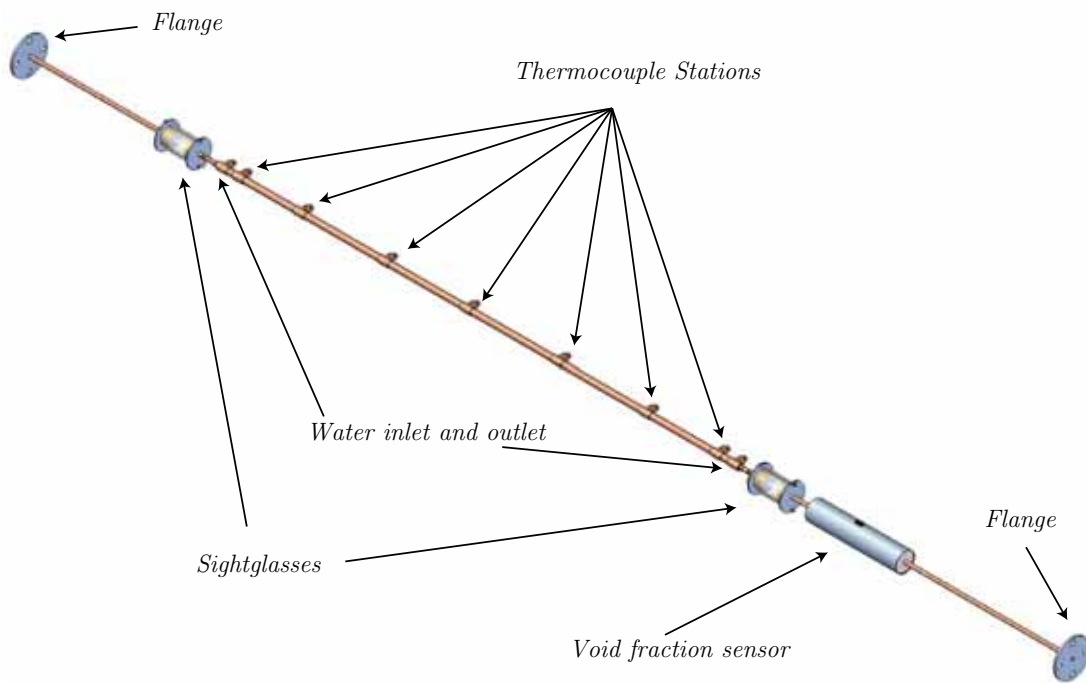


Figure 3.12: Test Section model

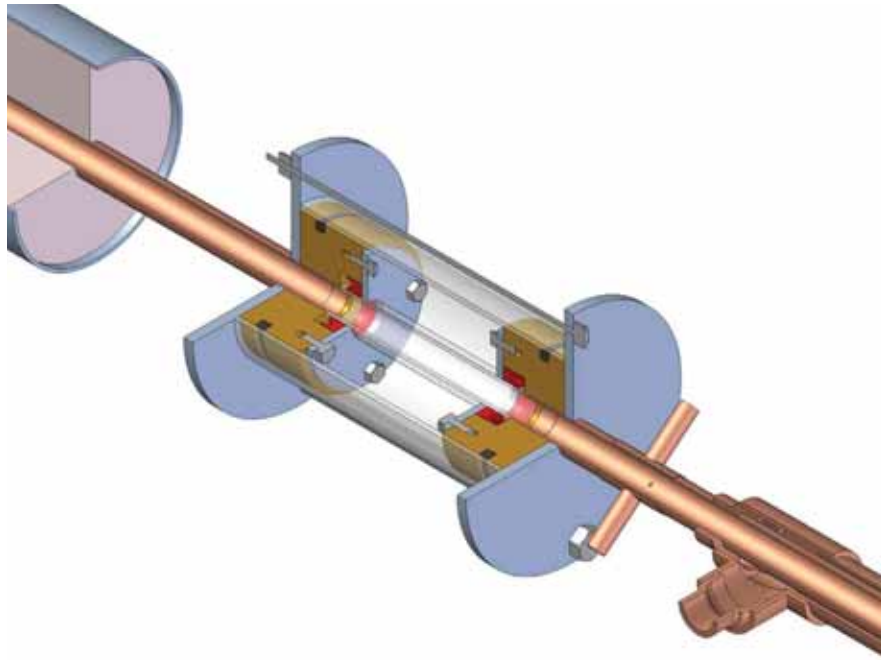


Figure 3.13: Cutaway view of the sight glass assembly

and housing are soldered together. Between the glass test tube and the incoming/outgoing tubes, there is a thin piece of housing to separate them, and to make sure that the two tubes do not press into each other, causing damage. The backing plates, connected by two bolts, hold the entire assembly together, under a slight amount of compression (such that there is no play among any of the components).

Between the sight glass and the test section, a distance of no more than 40 mm is left. Three circumferential pressure taps are made in this space. To ensure that the size of tap is not large, but to ease pressure transducer and capillary piping installation, a bush is installed over the outside of the tube and soldered at both ends. This bush has three fittings into which the capillary tubes slide. The tubes are also soldered into the fittings. The advantage of using this method is that, since you are applying heat and solder relatively far away from the small pressure tap hole, there is much reduced chance of plugging the hole. Also, it allows for the use of capillary tubes with much larger diameters, which help the responsiveness of the pressure signal, and can help make sure that the signal is

3.8 Test section design

not compromised by having liquid pockets in the line.

The heat exchanger itself, as previously stated, is a straight, horizontal tube-in-tube counterflow heat exchanger. The inner tube runs straight through, uninterrupted. A 2 mm copper wire is twisted onto the outside of the inner tube, at a pitch of about 0.3 meters. This acts both as a spacer between the inner and outer tubes of the annulus, and as a mixer, especially important to avoid temperature stratification when laminar flow is present in the annulus. The end connections between the annulus and inner tube are comprised of 15.8 mm to 9.55 mm reducers. At the ends, T-junctions are used to construct the inlet and outlet ports for the annulus. This construction is shown in Figure 3.14.

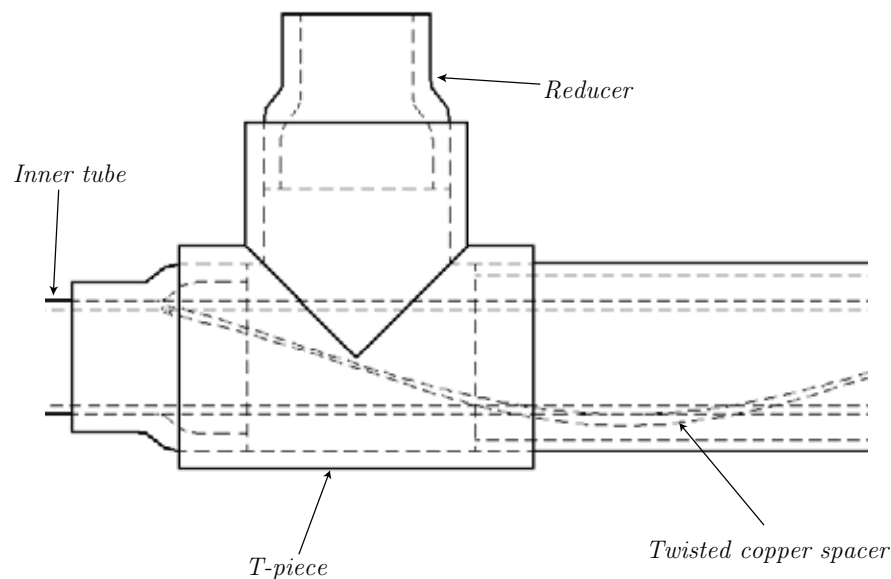


Figure 3.14: Inlet and outlet exchanger construction

Rather than having an uninterrupted length of outer tube in the annulus, this length is split into several parts, in equidistant sections along the heat exchanger. At each junction, an extra T-junction is placed there. The main reason for these junctions is to allow for the thermocouple wire utilized in direct inner tube outer wall temperature measurements to be strung out into the DAQ. As such, seven extra 15.8 mm to 9.55 mm reducers are utilized, and the remaining spaces between the exit and the wires are sealed using PTFE tape and put through a ferrule connector, which is tightened until proven to be leak-tight.

The exit configuration of the heat exchanger is constructed in the same method as the inlet. Between the refrigerant exit and the sight glass, the same pressure tap bush construction as in the inlet is used. The sight glass exit then leads to the void fraction sensor. When doing void fraction testing, the pressure traces found at the exit of the test section heat exchanger are used. After the void fraction sensor, as was necessary at the inlet of the section, a minimum of 50 internal diameters are required, such that the effect of the ninety degree turn (after the flange) is not propagated into the void fraction sensor.

3.9 Conclusion

This chapter detailed the experimental setup, i.e. its design, layout, construction, the apparatus and instruments utilized and the software backbone of the control. It also covered, in broad terms, the control methodology and instrumentation.

Furthermore, the experimental procedure is briefly discussed in this Chapter; this gives a brief overview of the methods that were utilized to fulfill the objectives of this study.

Chapter 4

Smooth tube air-water flow patterns

4.1 Analysis methodology

4.1.1 Introduction

At present, two main methods of forced heat transfer in condensing two-phase flow in horizontal tubes have been identified, namely gravity-based and shear-stress based heat transfer (Collier and Thome, 1994; Liebenberg, 2002). Neither one of these can adequately describe the heat transfer in the intermittent flow regime. Problems with the classification of the heat transfer methods in the intermittent flow regime are presented, and a possible method for classifying the heat transfer mode is evaluated. Preliminary results, obtained in an air-water experiment, are discussed, as well as their applicability in a refrigeration setup.

4.1.2 Classical heat transfer modes

The major flow regimes that have been identified as gravity-dominated are stratified and stratified-wavy flow. In these flows condensate pools at the bottom of the tube due to the relatively low velocity of the fluid. Although these are two distinct flow regimes, from a heat transfer model point of view, they are treated using very similar forms of the same equations.

A large number of existing heat transfer correlations, such as those of Dobson and Chato (1998) and Shah (1979), were not specifically developed for application when the prevailing heat transfer mode is gravity-controlled. The correlation of Thome *et al.* (2003) is one of the few methods that correctly models the heat transfer in stratified and stratified-wavy flow.

In a similar manner, the shear-stress model is best utilised to represent the annular flow regime. In this model, a thin liquid film wets the perimeter of the tube, which is in contact with a fast moving vapour core.

The majority of heat transfer correlations available in the literature were specifically tailored for this type of condensation, and it is the most efficient heat transfer mode, apart from dropwise condensation. It is however very difficult to design a heat exchanger to take advantage of dropwise condensation, due to the special coating required on the inner surface of the tube, among other problems. Furthermore, about 85% of the overall heat transfer in a two-phase heat exchanger occurs in the shear-stress-dominated domain, hence the importance and wide availability of correlations for said domain.

However, not all flow regimes that readily occur in a horizontal tube during condensation can be described and modelled using just one of the two models above. The intermittent flow regime, made up of both slug and plug flow defies classification of a single prevailing heat transfer mode. The next section details this particular case.

4.1.3 The intermittent flow regime and the prevailing heat transfer mode

As was previously discussed, it is difficult to classify the intermittent flow regime into a single dominant heat transfer mode, as could be done with the stratified-wavy and annular flow regimes. Intermittent flow can be described as a stochastic mixture of plug and slug flow. Nevertheless, due to the randomness presented by the flow, the development of a single model that can be used for heat transfer correlations is severely hampered.

In fact, modern heat transfer correlations (such as that of Thome *et al.* (2003)) do not specifically treat the heat transfer in the intermittent flow regime, rather,

they extend the shear-stress controlled heat transfer mode into this regime. The deviation between experimental data and the present model by Thome *et al.* (2003) in intermittent flow is 20%.

4.1.4 Time-fraction and probability

This section presents the hypothesis that will be stated later on in the dissertation and that forms the major focus of the investigation. Considering only the figures below (Figure 4.1 and Figure 4.2) it is difficult to judge what flow regime prevails. It is however, easy to judge the instant captured as a stratified flow or at least as a flow where gravity is the dominant force. In Figure 4.1 a still picture was taken as the middle of a slug went past the camera and the correct prediction would be intermittent flow. Thus over time, looking at the other stills before and after, and then objectively analysing the data it is easy to see that a slug was traveling past the camera. Figure 4.2 is an image of stratified-wavy flow.

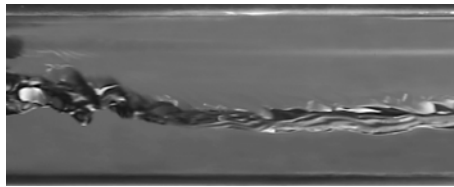


Figure 4.1: Stratified Flow?

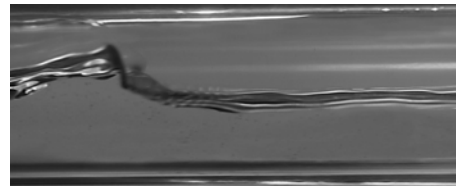


Figure 4.2: Slug Flow?

From a heat transfer perspective, this temporal variability in the flow has a large effect that has not yet been quantified. A simple shear-controlled model (*i.e.* annular flow) or a gravity-controlled model will not suffice on their own. Because of the mixture in dominant flow patterns as mentioned above the hypothesis is proposed that identifying and mapping these flow regimes in intermittent flow and adapting the model to this information will result in an improvement in heat transfer prediction if not at least a better understanding of intermittent flow. The objective is to utilize temporal analysis of intermittent flow to give more information about what is occurring in the intermittent flow regime.

Going back to Figure 4.2, the dominating mode of heat transfer, at that instance, can be seen to be gravity-dominated, due to the thick liquid pool at

4.1 Analysis methodology

the bottom of the tube, and the relatively thin layer at the top. Going to Figure 4.3, which was also taken in the intermittent flow regime, it can be seen that the dominating heat transfer mode is shear-stress based. This is concluded from the redistributed liquid film layer around the perimeter of the tube, and a relatively clear vapour core. Notice that there is still a thicker layer of liquid around the bottom due to gravity. This is also seen, but to a lesser degree, in annular flow.



Figure 4.3: Intermittent flow - between slugs

Thus, we can distinguish that in a single flow regime, the two separate heat transfer modes will have an effect. The question is whether a more accurate heat transfer prediction method can be developed if we can classify the flow regimes so that for every mass flow and vapour quality we know the fractional probability of time that the flow will be in a dominant heat transfer mode?

At present the existing models for annular flow are used in the intermittent flow regime. These models do not model the physical behavior of intermittent flow and only provide an average heat transfer coefficient by fitting the correlation to the data. The purpose of a unified model and of this study is to develop a model from the basic physics of the flow and to understand the driving phenomena behind the flows. The methods used here may not completely solve this problem but it is a step in a direction that strives to understand the physics behind these flows instead of modeling averages.

However we define the dominating heat transfer mode, the flow regime and its characteristics do not change. Although we are classifying sections of intermittent flow as either shear-stress or gravity-dominated, this does not change the fact that slugs and plugs occur and that the statistics are based on an instantaneous evaluation of the flow regime.

The main methodology we propose is to separate the flow into two main heat transfer modes, *i.e.* gravity and shear-stress based modes. We can then construct

4.1 Analysis methodology

a probability map showing the fraction of time that a specific heat transfer mode will occur (ranging from 0 to 1) at discrete points of vapour quality and mass flux. Once we have this, the heat transfer coefficient can be calculated using the time-fraction probability map combined with the different heat transfer correlation equations to improve the overall prediction of the heat transfer coefficient. For example, a heat transfer coefficient equation could take the form of

$$h_{c,o} = tf \cdot h_{grav} + (1 - tf) \cdot h_{shear} \quad (4.1)$$

where $h_{c,o}$ is the total heat transfer coefficient, the tf number is a dimensionless number that varies between 0 and 1, and indicates the probability that the heat transfer mode will be gravity-dominated, h_{grav} is the heat transfer coefficient calculated from the equation stemming from the gravity-based heat transfer mode, and h_{shear} is the coefficient calculated from the shear-stress-based heat transfer mode.

The methodology used to distinguish between the heat transfer modes objectively is separated into the time-frequency response analysis of the void fraction, pressure sensor data, and the light intensity through the tube. Further detail of the analysis is discussed in Section 4.1.5.

4.1.5 Analysis

In order to improve the model for intermittent flow an objective method of evaluating flow regimes had to be used. The methods mentioned in Chapter 2 all have their advantages and disadvantages. The major requirement in this study is to be able to evaluate the flow regime at every time step during the sample time. Methods such as pressure PSD which result in a spectrum of all frequencies over the entire time is insufficient. Visual observations are too subjective. Thus a more objective method had to be found that allows analysis in the time domain with the available equipment.

The first step is to use time frequency methods. This method of signal analysis results in a frequency response over time and the change in frequency content can then be mapped. This can then be used to evaluate the flow at smaller intervals of time. This method has been used previously and Hervieu and Seleglim (1998)

4.1 Analysis methodology

and Klein *et al.* (2004) demonstrated that it can be used to discriminate flow regimes. This method of signal analysis can be applied to any of the dynamic signals that are sampled from the test section.

A further step in assisting the analysis of flow regimes is the use of high speed video recordings of the flow. The intensity of light that passes through the test section is used and time-frequency analysis is done on the intensity signal.

For the heat transfer equation proposed in section 4.1.4 it would be necessary to determine the statistical probability that a heat transfer mode will be dominant for each mass flow and vapour quality in intermittent flow. This will then result in a time-fractional function that represents the probability and fraction of total time that the flow spends in a particular heat transfer mode. The time-fractional mapping of flow regimes were used by Niño *et al.* (2002) to describe flow in micro channels. The time-fraction will naturally increase to unity at the boundaries of intermittent flow close to the classical transitions as the dominant flow occurs all of the time. For example, the transition from intermittent to annular is marked by an increase in percentage time-fraction of annular flow up to 100%.

The data used and method of analysis will be described in short with some data gathered from an air-water system. The investigation was done on an air-water system to validate the data capture and video analysis on a system with a forgiving working fluid. It has already been shown by Liebenberg (2002) that power spectral density (PSD) analysis of the pressure traces can be used to predict flow regimes. This method is, however, limited in that it gives only frequency information and no time domain information. Furthermore a PSD is based on the assumption that the signal is periodic and repeating, not stochastic and thus limits the use of this analysis method to the determination of the overall dominant flow patterns.

A more objective method had to be found that allows analysis in the time domain with the available equipment. The first step was to use time-frequency methods. This method of signal analysis resulted in a frequency response over time and the change in frequency content could then be mapped. This could be used to evaluate the flow at smaller intervals of time. This method of signal analysis could be applied to any of the dynamic signals that were sampled from the test section. With additional analysis of the signal and evaluating the stationarity

(Hervieu and Seleglim, 1998) of the signal over time the transitions could be located as flow rates with high levels of 'unstationarity'.

A further step in assisting the analysis of flow regimes was the use of high-speed video recordings of the flow. The intensity of light that passed through the test section was used and time-frequency analysis was done on the intensity signal. The method of using light intensity passing through the tube was similar to the work done by Revellin *et al.* (2006) with lasers and diode light meters for micro channels. The background of time-frequency analysis and the methods investigated as potential candidates for use in analysis of the experimental data are given in Section 2.6.

4.2 The analysis procedure

For the analysis of the high-speed recorded image sequences, a LabView program was used. The sequence of images was captured at 250 frames per second and saved as an *.avi* file. The amount of data that these images use prohibited the real time analysis of a flow regime. The recordings were analyzed by using an area of interest defined on the image. The area was wide enough to ensure a continuous examination of the flow in most cases. The height of the area was taken from the bottom to the top of the tube. The mean light intensity and standard deviation of the light intensity in this area was sampled during the sequence. When the measurement was completed the necessary statistics and signal analysis were done. This included fast Fourier transform (FFT), power spectral density (PSD) analysis, and a time-frequency analysis of the mean light intensity. The probability density function (PDF) and cumulative probability density function (CPDF) of the light intensity range were also computed in order to establish if these statistical methods were relevant.

The analysis of the time-frequency data could then commence. For intermittent flow in general the high frequency activity represented annular flow or a liquid annulus with bubbles and a liquid flow with entrained bubbles. From a light intensity point of view the large number of liquid vapour interfaces and the unstable, wavy interfaces in these flows caused diffraction of the light and a rapid variation in light intensity, thus higher frequency activity. The stratified and

4.3 Classification of flow regimes

stratified-wavy flows resulted in less spectral activity and the largest variation of light intensity was due to the liquid vapour interfaces of the stratified layer. Stratified flow had lower frequency activity. The time-frequency method could thus improve objectivity in classifying flow patterns, especially in this case where a stochastic regime, namely intermittent flow was being investigated in detail. The use of a spectrogram with the light intensity method also had the advantage that the corresponding image at the instant of time being investigated could be recalled and used by the analyst in decision making.

The flows classified as annular flow were defined as such based on the premise that annular flow is a shear-dominated flow where gravity does not play a large role and this corresponded to high frequency activity due to the large number of small interfacial waves. The stratified regimes are flows where gravity has a significant influence on the flow pattern and were characterized by low frequency activity due to the low amount of interfacial activity.

To facilitate the analysis a classification method was devised where the energy density of a single frequency of the signal was plotted over time. The frequency of this plot could be set in the program. The peaks where the energy density was above a set value were classified accordingly and the troughs which were flows with spectral activity at other frequencies were classified as the opposing sub-regime. The method proposed only included the two opposing sub-regimes. If future flow regime mapping should include the entire flow regime range the classification method could be expanded but such analyses would become complex and are beyond the scope of the present study.

4.3 Classification of flow regimes

Before any results are discussed it is important to discuss the interpretation of the flow regimes. The air-water tests were done primarily to validate the visual method and secondly as validation of the void fraction and pressure data time frequency analysis. It has to be stated that the flow regimes that occur in air-water mixes at low pressure differ considerably from those of condensing refrigerant but if sub-regimes in the intermittent flow can be identified with success

4.3 Classification of flow regimes

the possibility of taking this method further will be investigated. What follows is a discussion of the interpretation method used during the analysis.

Annular flow is specifically defined for this study and in this case has a wider definition than conventional standards.

Annular flow:

- A high velocity vapour core with continuous liquid annular film around the perimeter of the tube.
- Annular flow with a thick liquid pool.
- The interface between the liquid annulus and the vapour core is disturbed by small amplitude waves and droplets.
- Bubbles may occur in the annulus and usually do when the annulus is thick.
- Liquid film is thicker at the bottom than at the top.

For visual observations these include:

- A darker than average image with a large amount of distortion.
- Usually a large amount of vapour moving at a high speed.
- An annular flow with a large amount of liquid pooling with visible waves on the annulus.
- Both of the above may include small bubbles.
- A bubbly type of flow is assumed as annular with an average vapour core. This is assuming that the liquid next to the wall, as with annular flow, is responsible for heat transfer.

Stratified and stratified-wavy:

- Vapour on top of a liquid, stratified layer.
- A stratified layer with interfacial waves.
- The annular film effectively covers only part of the tube and it is therefore classified as stratified.

For visual observations these include:

- A stratified flow with no visible annular film or interfacial waves on the film interface.
- A stratified-wavy flow with the same criteria as above.

4.4 Preliminary air-water testing

Experiments were done on an air-water loop to validate the method. Using the Baker map as rough guideline experiments were done in the slug and plug regions that would coincide with the characteristics of intermittent flow. The results given in the figures below represented a small sample of what can be expected for this type of analysis.

4.4.1 Experimental facility

The air-water loop used for these experiments used the air supply in the workshop and this line was passed through a valve and regulator to control the pressure and flow rate (Figure 4.4). The water and air lines both went through a coriolis flow meter before they were mixed in a T-section mixer. The mixer had holes for the air to mix with the water flow around the circumference of the water tube. The mixer was followed by a long calming section. The flow then passed through a glass section for visual observations. The next section had two pressure transducers and this was followed by the capacitive void fraction sensor. The water then passed through another section of tube before emptying into the holding tank where the air was separated from the water.

4.4 Preliminary air-water testing

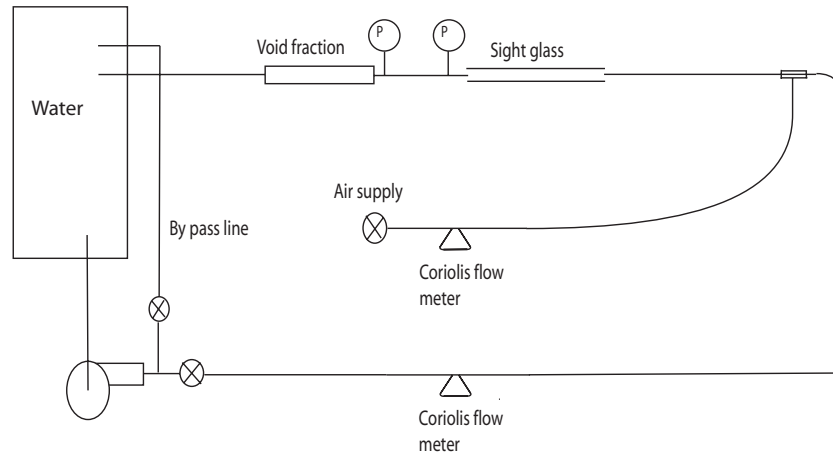


Figure 4.4: Schematic of air-water test loop

The equipment available for this test section allowed a range of testing that suited the Baker map predictions of flow regime well. The superficial mass flows of water tested included $100 \text{ kg/m}^2\text{s}$ to $2000 \text{ kg/m}^2\text{s}$. The superficial mass flow of air could be up to $60 \text{ kg/m}^2\text{s}$ (Figure 4.5). This test range included almost the complete slug and plug regimes of the Baker map and included the transition into annular flow.

During these tests the pressure, void fraction and vision data needed for frequency analysis were saved with controlled timing. The mass flows and other properties like flow temperature were also saved. The main purpose of the air-water testing was the validation of the visual analysis methods and as a secondary outcome the other signals were also recorded for analysis.

4.4 Preliminary air-water testing

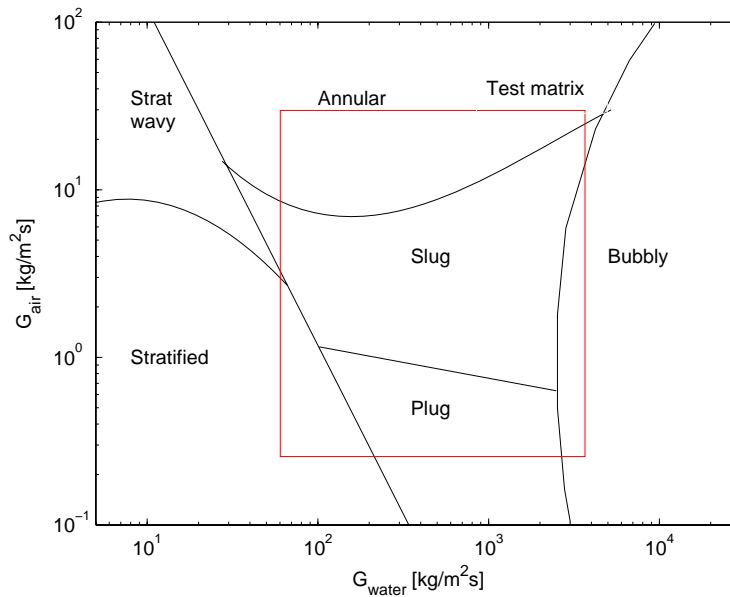


Figure 4.5: Baker map with test region

4.4.2 Results

4.4.2.1 Time-frequency

The time-fractional distribution, which was the final outcome of this investigation was computed by using a time-frequency analysis. The time-frequency analysis of light intensity was the basis of most work done in this section. The time-frequency varies with mass flow and vapour quality or fraction of air in the case of an air-water system. The change in frequency data between gravity-dominated flows and shear-dominated flows was the major characteristic used in the analysis. With the settings for the spectral analysis used during this study a strong emphasis was put on the time resolution. This meant that the window size was set shorter and the prediction of the time that a specific frequency occurred was more accurate. This was done at the expense of frequency resolution with the result that time-frequency plots showed long lines in the direction normal to the time axis. If the window of analysis was changed more accurate frequency data could have been gathered although that had no application in this study.

As a case study, the change of spectrographic data of tests done at a total mass

4.4 Preliminary air-water testing

flux of $250 \text{ kg/m}^2\text{s}$ will be discussed. The data represented here are in the form of PSD graphs and time-frequency plots. The time-frequency plots represent the time domain, frequency domain and time-frequency domain data together. The top graph is the time signal for 10 seconds. The left hand side of the figure has the frequency domain PSD graph with the frequency on the vertical axis. The time-frequency plot represents the time scale on the x-axis and frequency on the y-axis. This results in a plot where times of high frequency activity can easily be seen and correlated with the correct frequency.

For low fractions of air the flow was inclined to be more stratified and the corresponding PSD (Figure 4.6) indicated a frequency content of less than 20 Hz. On a time-frequency plot the occurrence of higher frequency activity coincided with annular flows. The higher frequencies would be the result of fast changing light intensities due to the large amount of small interfacial waves caused by the interfacial shear between vapour core and annulus. The time-frequency plot of a predominantly gravity-dominated flow at a mass flux of $250 \text{ kg/m}^2\text{s}$ is given in Figure 4.7. The gravity-dominated regime was characterized by a steady interface between liquid and air and the frequency content was low. As the air flow rate increased for a constant mass flux of water the shear forces became more dominant and therefore the shear-dominated flow regimes like annular flow occurred for longer.

The PSD graphs of flow with higher mass flows of air are given in Figures 4.8 and 4.10. The frequencies for shear-dominated flows have a wider range of frequency activity. In these figures the increase in amplitude and the frequency of activity can be seen. On the time-frequency plots the higher frequencies occurred at intermittent time periods and the increase of these activities were recorded for the time-fractions. The highest level of activity could be seen at frequencies less than 40 Hz. The low energy frequency activity at frequencies above 100 Hz were not found useful for the purpose of classifying air-water flow.

4.4.2.2 Time-fraction map

The result of analysing the air-water flow over a range of flow rates that included the intermittent and annular regimes was a time-fractional map. The

4.4 Preliminary air-water testing

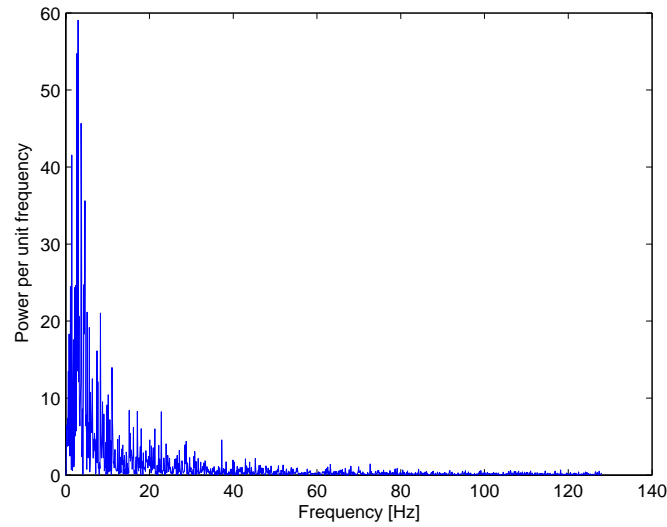


Figure 4.6: Vision based PSD of air-water flow for $G_{air} = 5 \text{ kg/m}^2\text{s}$ and a total mass flux of $250 \text{ kg/m}^2\text{s}$

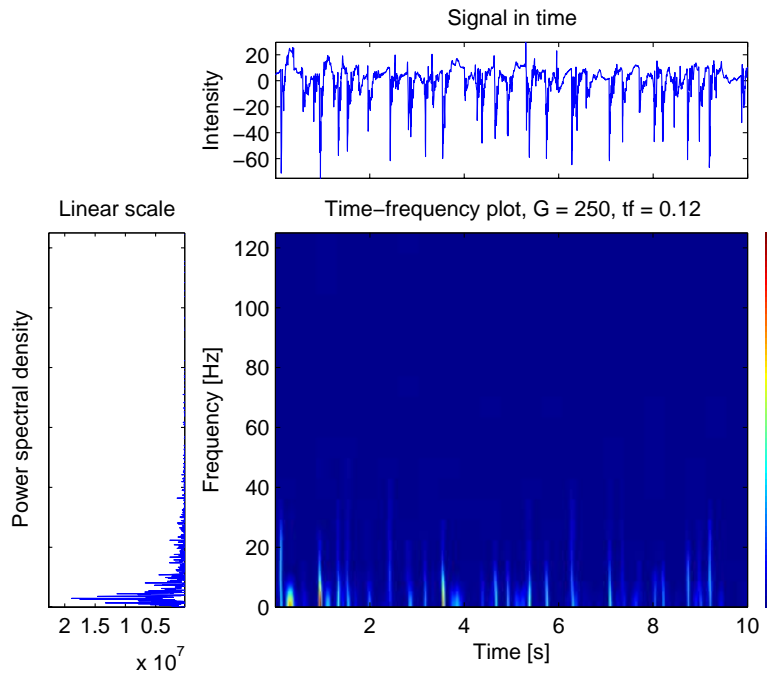


Figure 4.7: Vision based time-frequency analysis of air-water flow for $G_{air} = 5 \text{ kg/m}^2\text{s}$ and a total mass flux of $250 \text{ kg/m}^2\text{s}$

4.4 Preliminary air-water testing

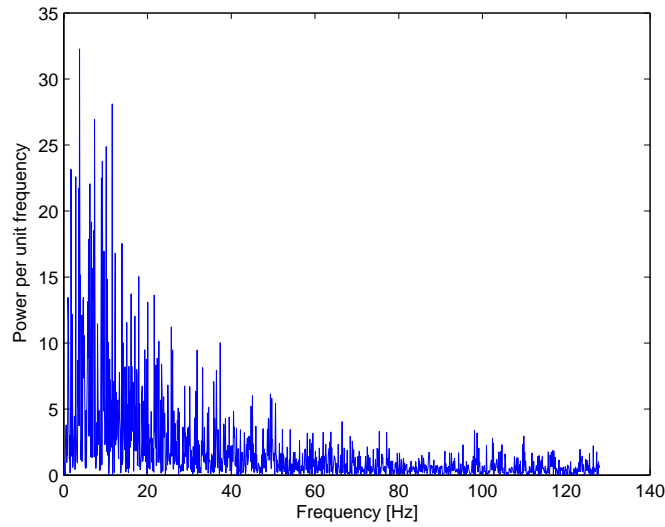


Figure 4.8: Vision based PSD of air-water flow for $G_{air} = 12 \text{ kg/m}^2 \text{ s}$ and a total mass flux of $250 \text{ kg/m}^2 \text{ s}$

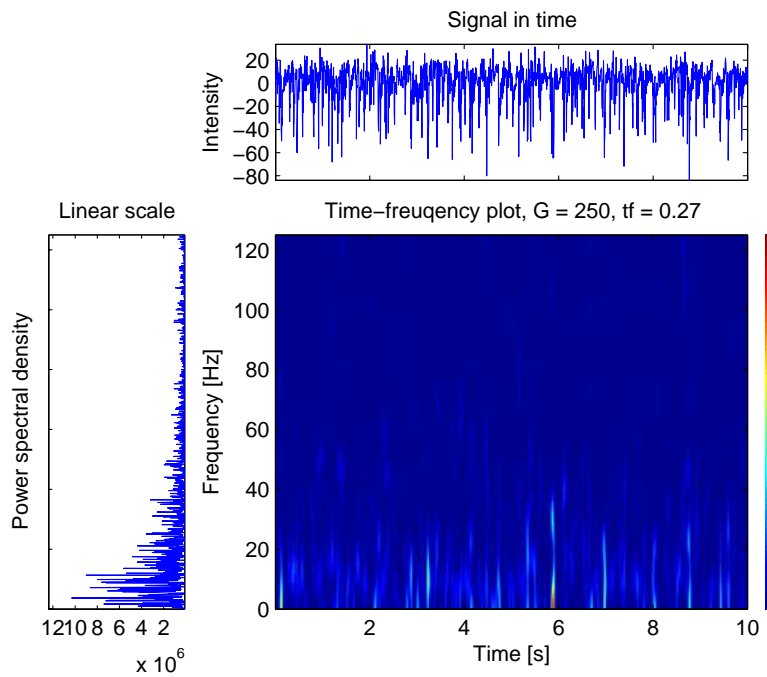


Figure 4.9: Vision based time-frequency analysis of air-water flow for $G_{air} = 12 \text{ kg/m}^2 \text{ s}$ and a total mass flux of $250 \text{ kg/m}^2 \text{ s}$

4.4 Preliminary air-water testing

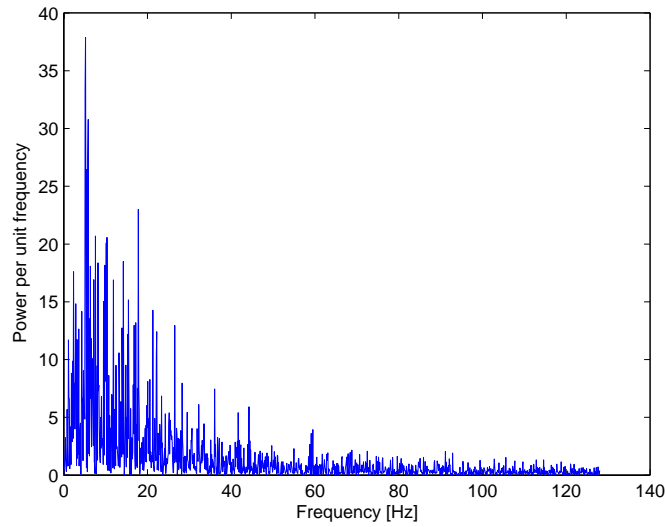


Figure 4.10: Vision based PSD of air-water flow for $G_{air} = 17 \text{ kg/m}^2\text{s}$ and a total mass flux of $250 \text{ kg/m}^2\text{s}$

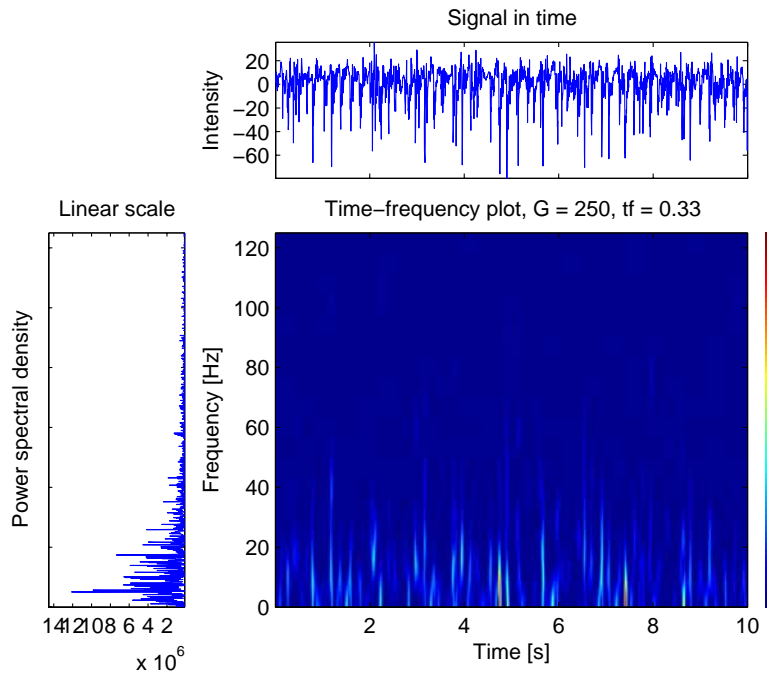


Figure 4.11: Vision based time-frequency analysis of air-water flow for $G_{air} = 17 \text{ kg/m}^2\text{s}$ and a total mass flux of $250 \text{ kg/m}^2\text{s}$

4.4 Preliminary air-water testing

time-fractional map was a classification of the flow into gravity-dominated and shear-dominated flows on a fractional time basis. This means that the map expressed the amount of time that a flow at a specific condition was likely to be shear dominant for a certain total amount of time. The data for individual mass flows are presented in Figure 4.12. These figures have the air mass flux, G_{air} , as x-axis and the y-axis is the time-fractional prediction that flow will be annular. The function used to fit the data was a general linear model with a binomial function which is generally used to present data that are a fraction of a total.

The data in Figure 4.12 were combined in a single figure (Figure 4.13). There was a general increase of annular flow as the mass flows increased. This followed from the obvious conclusion that higher mass flows of both air and water would result in more shear-stresses in the flows and thus increasing the occurrences of shear-dominated flow regime. There was also a tolerance band around each line and the predictions can thus vary with some amount. This was due to the accuracy of the method which was limited by the analysis method. For time-frequency analysis the window function was between 32 and 64 data points wide. This means that the analysis was not instantaneous and but rather an average over a short time. The window size used during analysis put more emphasis on time resolution than frequency resolution for this reason. Taking into account that these flows were highly stochastic and that the changes from one mass flow to the next brought about only extremely minor changes in the flow itself the method performed well in predicting these small changes. Therefore, the mass flows do not follow an exact order from top to bottom but the trend is certainly clear.

The findings were also plotted on the Baker map as contours of a surface (Figure 4.14). This figure indicates the time-fraction that gravity-dominated flow occurred in the tests done. During intermittent flows (slug and plug) the fraction of gravity-dominated flows were higher and there was a transition into shear-dominated flow, making up the total time-fraction, as the air flow rate increased. As the annular flow regime transition was crossed the shear-dominated regime took over as the dominating regime. As the air flow increased the the shear-dominated flow also increased. The fraction of gravity-dominated flow was higher at lower mass flows of water and air. As the water flow increased the shear

4.4 Preliminary air-water testing

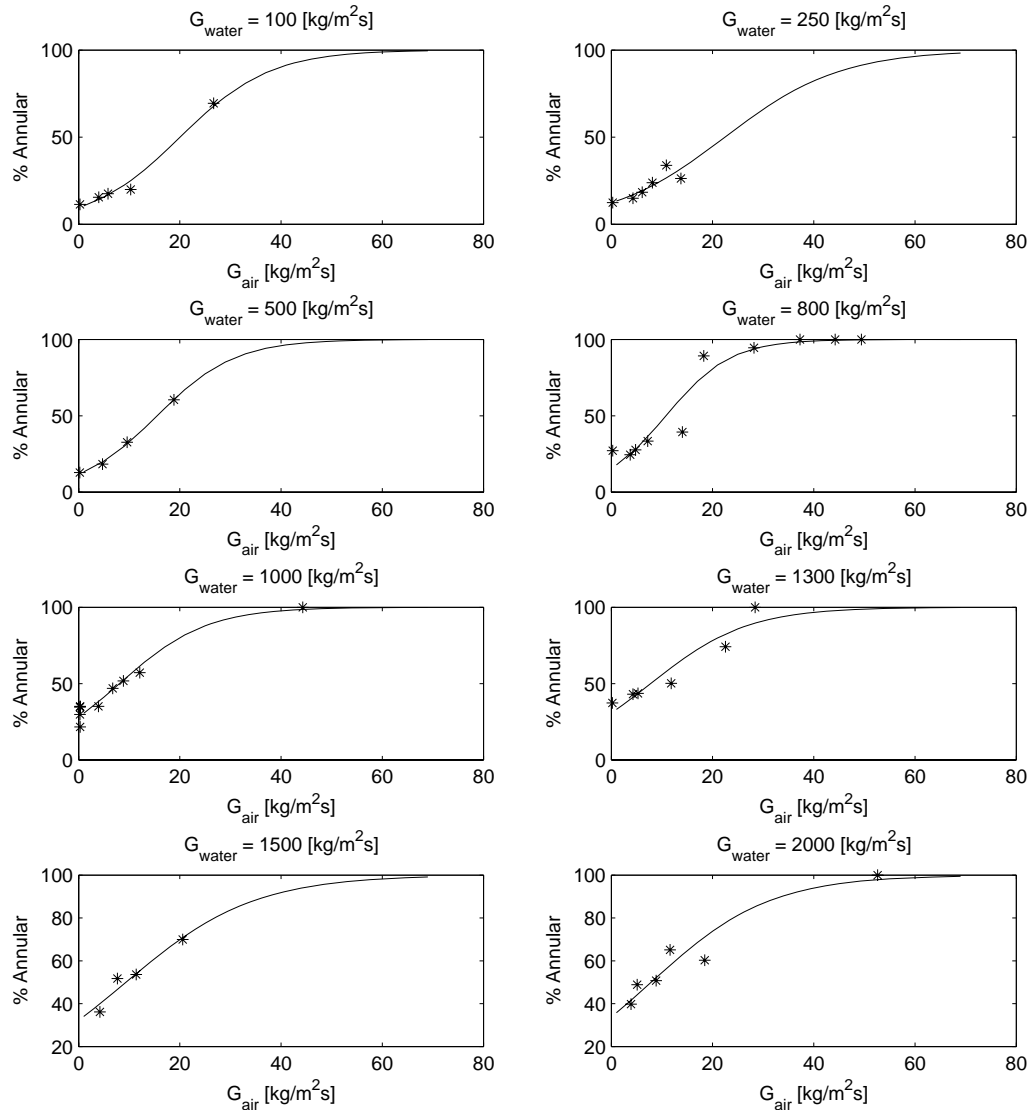


Figure 4.12: Separate plots of test points per air mass flux with time-fraction functions

component increased and the time-fraction decreased. This decrease coincided well with the annular transition line of the Baker map except at the lower water flows where the transition was at a later stage than predicted.

4.4 Preliminary air-water testing

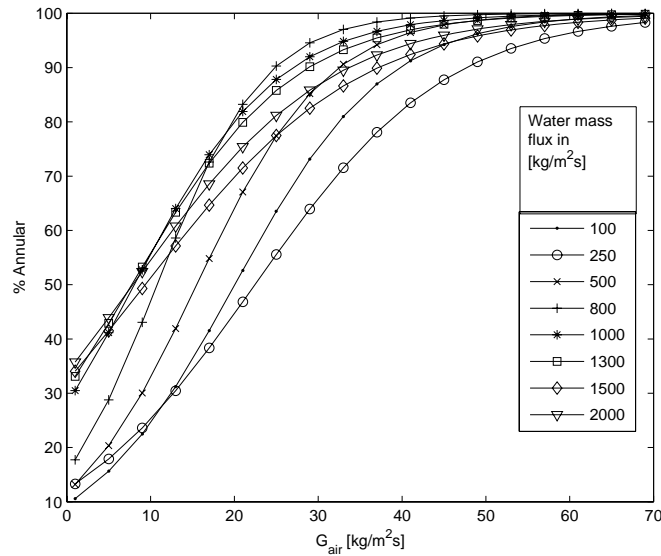


Figure 4.13: Function predicting the fractional time of annular flow at various total mass flows, for air-water flow

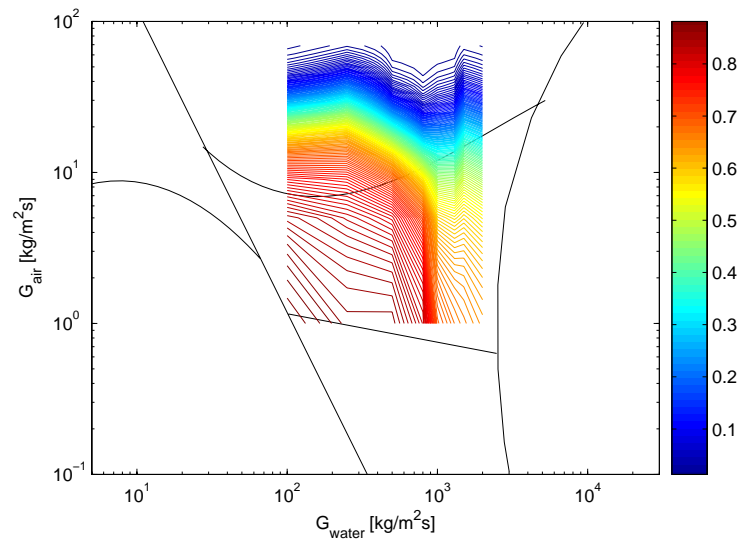


Figure 4.14: Time-fraction of gravity-dominated flow found during testing of air-water flow

4.4.3 Pressure and void fraction

It is known that the pressure signals of air-water systems at low pressure do not yield conclusive data for frequency analysis. This could be the result of the low pressure being too small a percentage of the full scale value of the pressure transducer or that the readings are erroneous. The sensor might also be producing too much noise. Interference from other devices could be contributing to this effect. A time-frequency analysis of pressure signals could not yield a significant discriminating frequency on which to base decisions.

4.5 Conclusion

The air-water tests were done to validate the vision based light intensity analysis in the time-frequency domain. The results of these tests indicated that the method could be used to successfully and accurately identify small differences in the flows. The method was, however, strongly dependent on the user input, but had the advantage that results could be verified by examining the image corresponding to the exact time on a time-frequency plot. Taking into account the nature of these flows and the small differences in appearance and other variables it is noteworthy that a method of analysis can detect such small variations. After analysis of the air-water data and complete development of the technique to its present state refrigerant tests were planned.

Chapter 5

Smooth tube refrigerant flow patterns

5.1 Refrigerant experimental test matrix

The testing done in this study involved a smooth 9.55 mm tube and a test section as described in Chapter 3. The test matrix included 101 data points ranging in mass flux from 250 kg/m²s up to 650 kg/m²s, and with a vapour quality varying between 0.05 and 0.65. The majority of the test matrix was in intermittent flow, while some points were recorded in the annular regime and in the stratified-wavy regime (Figure 5.1). This was done in order to investigate the transitions.

The data points were each a mean of a 1000 samples taken continuously at steady operation. The criteria for testing are given in Table 5.1 and this was strictly adhered to for consistency and quality data.

Table 5.1: Experimental testing criteria

Condition	
T_{sat}	40°C
EB	<1%
\dot{m}_{ref}	±5 kg/m ² s max

A summary of the conditions during testing is given in Table 5.2 and this describes the general test conditions of saturation temperature, pressure energy

5.1 Refrigerant experimental test matrix

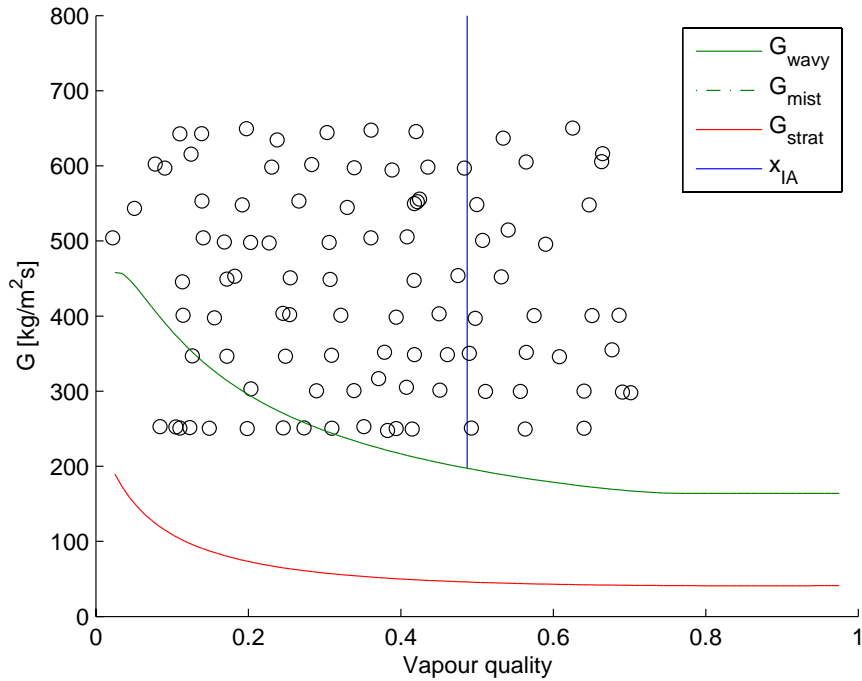


Figure 5.1: Experimental test points for R-22 condensing at 40°C

balance and mass flux.

Table 5.2: Mean testing point information

Measurand	Mean	Standard deviation
T_{sat}	39.7°C	±1.9°C
P_{sat}	1449 kPa	±65 kPa
EB	0.65%	±0.26%
\dot{m}_{ref}	Test dependent	max: 2 kg/m ² s

The system performed well in terms of accuracy, stability, repeatability and most of all controllability. Table 5.3 lists the required mass fluxes, the mean testing mass fluxes and their standard deviations.

The oil concentration in the refrigerant was tested using ASHRAE (2006) which described the correct procedure to analyze the oil content of the refrigerant circulating in the system. The oil concentration was found to be 2.3% in

5.2 Refrigerant in smooth tubes

Table 5.3: Mean testing point information

Required $G \text{ kg/m}^2\text{s}$	Mean obtained $G \text{ kg/m}^2\text{s}$	Standard deviation
250	250.83	± 1.36
300	299.98	± 0.99
350	349.28	± 1.97
400	400.23	± 1.86
450	450.05	± 1.51
500	499.53	± 1.68
550	550.23	± 1.71
600	600.43	± 1.98
650	648.10	± 1.18

conditions that would maximize oil flow. Several other samples were taken and the oil concentration was found to be a function of the operating condition. At lower mass fluxes and liquid flow the oil concentration was as low as 0.5%. The effect of oil concentrations on heat transfer was fully discussed in Christians-Lupi (2007). From a flow pattern perspective the oil film would have an effect when annular flow was observed that was in reality only an oil film. Overall the oil concentration was very low and did not influence the flow patterns severely.

The uncertainties of measurements taken and the propagation of uncertainty in values used for calculating the conditions in the system was important to quantify the quality of predictions. As part of the development of the system an uncertainty analysis was done and the uncertainties are presented in Appendix A. A detailed and in-depth uncertainty analysis of refrigerant flow parameters is presented in Christians-Lupi (2007).

5.2 Refrigerant in smooth tubes

The experiments done for this dissertation were set up to capture the data necessary to accept or reject the hypothesis proposed in the previous chapter. The experiment was conducted with R-22. The test section and data acquisition pro-

5.2 Refrigerant in smooth tubes

cedure were designed to maximize the accuracy and the quantity of data captured. The data capture was done in two parts while maintaining constant conditions and an energy balance error of less than one percent. In the first part the heat transfer and pressure drop data were captured whereas data suitable for frequency analysis were captured in the second part. The frequency data included a high-speed video and a timed capture of pressure transducer signals and the void fraction sensor signal. The threefold nature of the frequency data and the results from each will be discussed.

5.2.1 Vision

As mentioned earlier in the dissertation a method of flow pattern classification was developed for analysis of intermittent flow in a more objective manner. The analysis of the light intensity captured through the flow by a high-speed camera proved successful on air-water flow and was indeed not limited to intermittent flow only. After the validation tests on the air-water system were performed and the positive results were obtained, this method was applied to refrigerant flow. The expectation was that condensing refrigerant flow would be more difficult to analyse because of the similarity of flow patterns in the annular to intermittent flow regimes.

5.2.2 Experimental data capture and data reduction

In order to speed up the frame rate of the camera the pixel size of the image had to be reduced. This reduced the data per image and because the bandwidth of the cable was constant more images could be taken. The resolution of the images that were analysed was about 160 by 150 pixels and this was found to be a good resolution without overrunning the buffers and well within the capabilities of the camera. The images captured were saved in *.avi* format for easy viewing and analysis. Over 700 000 images were analysed with this method. Each sequence included 2500 images of the flow. The analysis program used a user-defined area, set to include the diameter of the tube and a length in the direction of flow that would result in a continuous intensity signal. The mean light intensity of the signal for each image was stored in an array that made up the signal. The

5.2 Refrigerant in smooth tubes

sampling frequency was added to complete the time domain characteristic of the signal. The statistics, signal conditioning and signal analysis of the signal were then done. The time-frequency analysis or spectrogram settings for the basic method used included the window type, window length, frequency bins and time step scale. A Gaussian window and a window length of 32 was used for the refrigerant allowing for a good time and frequency resolution combination. The data reduction step to evaluate the time-frequency data and to get a time-fraction was done by setting and evaluating a single frequency over the time of a capture. The frequency could be chosen to represent the activity in the flow and a threshold level was set. The flow only had to be classified into one of two groups and thus the flows with frequency activity and a resulting high value of amplitude or energy density at the selected frequency were grouped. The time-fraction over a sample that was large enough to represent the flow under the particular conditions was then used to calculate the time-fractional probability that a particular flow would occur.

The videos of all the recorded data points were analysed and the time-fractions were saved with the flow properties. The data were presented in various forms and combined into the final model.

The general flow observations in flow condensation observed in the experiment will be discussed from the annular regime and through to very low vapour qualities. The flow patterns observed can be followed on the superposition of the experimental data points captured on the Thome and El Hajal (2003) flow pattern map (Figure 5.1). The annular flow was uniform and easily identifiable with the annulus of liquid around the perimeter with clear interfacial waves and the vapour core sheared past the inside. As the vapour quality dropped this liquid annulus became thicker and more unstable. The liquid layer at the bottom of the tube also thickened with intermittent waves (not washing the top of the tube) passing. The flow remained like this at high mass flows but at low mass flows there was also the occurrence of more stable flows where periodic stratification tended to happen for very short time intervals. This type of flow occurred for most of the intermittent flow regime. As the vapour quality dropped further, below 10% to 15% classical slug and plug flow occurred with waves washing the top of the tube and sections of liquid with entrained bubbles also occurred as stated in

Chapter 2. Tests at the higher mass flows tended to be annular at a lower vapour quality than x_{ia} because of the strong shear forces present. The transition from annular to intermittent was however sufficiently accurate to predict where shear forces are less dominant.

5.2.3 Vision results

The data points captured with the refrigerant system included heat transfer and pressure drop data. The second data set of timed captures for time-frequency analyses was intended for analysis into a time-fractional map that could be applied to the heat transfer data. The discussion of the final results where the time-fractions have been applied to the data is given later (Figure 5.4).

The optical method of analysis was found to be the most productive and this section discusses the results. Similar to the air-water analysis, the refrigerant was analysed point for point and the program was used to set the appropriate thresholds. For the refrigerant the area of the image used was the same as with the air-water analysis. There was a difference in the signal if the area chosen for analysis was biased to only one section of the tube and the best results were for an analysis of the entire tube diameter and a short length in the direction of flow. The combination of different areas and the analysis of multiple signals that could be generated with this method could lead to more accurate and generalized flow pattern identification methods. This would be helpful if a vision based time-fractional map of the entire flow regime map is generated.

The flow passed the sight glass with high velocity and it was only barely possible to make out the detail with the naked eye. The intermittent nature was, however, visible with the naked eye. The use of a high-speed camera to slow down the action helped to investigate the flow and the time-frequency analysis added a powerful method of discriminating between the flows. Some samples of the types of flow present during intermittent flow indicated the intermittent change to flow with a thicker annulus. The flow direction in the sequence was from left to right and time steps also increased from left to right (Figure 5.2 through Figure 5.5). The stratified liquid pool was always present and had interfacial waves for most of the mass flows tested. The flows in the following figures were taken in

5.2 Refrigerant in smooth tubes

the intermittent regime but not at the low vapour qualities where slug flow is present. The interfacial waves washed up the side of the tube, but did not close the tube off by reaching the top of the tube yet. The variation in thickness of the annular film was clearly visible. The effects mentioned above should all have an effect in the overall heat transfer in the flow regime.



Figure 5.2: Intermittent flow at $G = 250 \text{ kg/m}^2\text{s}$

As the vapour quality decreased the interfacial waves became larger and washed higher up the sides of the tube (Figure 5.3). A further decrease in vapour quality resulted in the slug flow part of intermittent flow being reached. Slug flows only occurred at the very low vapour qualities of less than 15%. The end of a vapour slug followed by a liquid flow with entrained bubbles and the beginning of the next vapour slug was recorded in Figure 5.4. At this flow rate the time-frequency method used did not distinguish between the prevailing flow regimes in an ideal manner. The entrained bubbles between slug were classified as shear-dominated or annular flow. The model did not yet include the low vapour qualities.

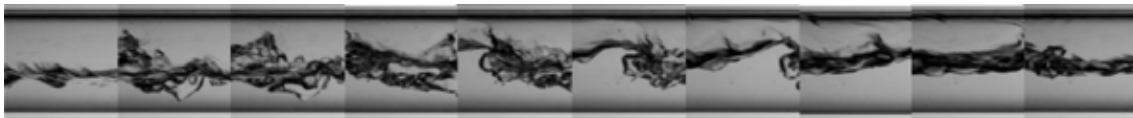


Figure 5.3: Intermittent flow at $G = 250 \text{ kg/m}^2\text{s}$ with a periodic wave passing

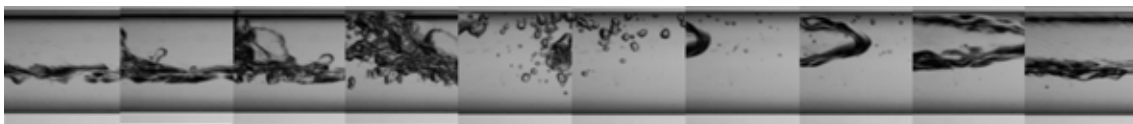


Figure 5.4: Intermittent flow at $G = 250 \text{ kg/m}^2\text{s}$ with a slug and entrained bubbles

5.2 Refrigerant in smooth tubes

At higher mass flows shear-dominated flow was more common. The effect of gravity was lower and there was almost always an annular film with interfacial waves on it (Figure 5.5). The layer of liquid that was pulled to the bottom of the tube by gravity thickened as the vapour quality decreased and at the lowest vapour quality slug flow occurred.

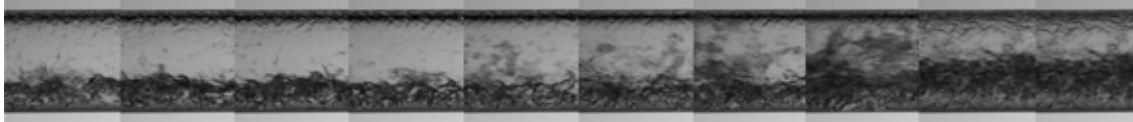


Figure 5.5: Intermittent flow at $G = 400 \text{ kg/m}^2\text{s}$

The time-fractional plots presented in this dissertation for refrigerant flow are only a sample of representative data. The mass fluxes used for these cases were 250 and $300 \text{ kg/m}^2\text{s}$. The method of analysis used for refrigerant flow was similar to that described for air-water data. The time-fractional plots are presented in an order with increasing vapour quality. The PSD of flow with a vapour quality of 0.25 had low energy densities compared to the other samples (Figure 5.6). The time-frequency plot indicated levels of low activity with intermittent high frequency activity. These flows appeared similar to the images in Figure 5.3.

Most activity in the frequency domain occurred at frequencies of less than 20 Hz for the flow at a vapour quality of 0.28 in the mass flux range of $300 \text{ kg/m}^2\text{s}$ (Figure 5.8). The time-frequency analysis also indicated the low frequency activity (Figure 5.9). There was little activity visible at higher frequencies for this case but the time-fraction of shear-dominated flows doubled from the previous sample. The reason for this increase was the higher mass flux and also that flow between vapour qualities of 0.25 to 0.50 appeared similar in the annular flow in general. The major difference being the effects of gravity that were visible in the amount of liquid at the bottom of the tube and the appearance of periodic waves.

For the flow with a vapour quality of 0.40 the PSD was similar to that of Figure 5.8 with most of the frequency activity at less than 20 Hz and of the same magnitude (Figure 5.10). The time-frequency plot indicated the increase in periodic high frequency activity (Figure 5.11). This high frequency activity

5.2 Refrigerant in smooth tubes

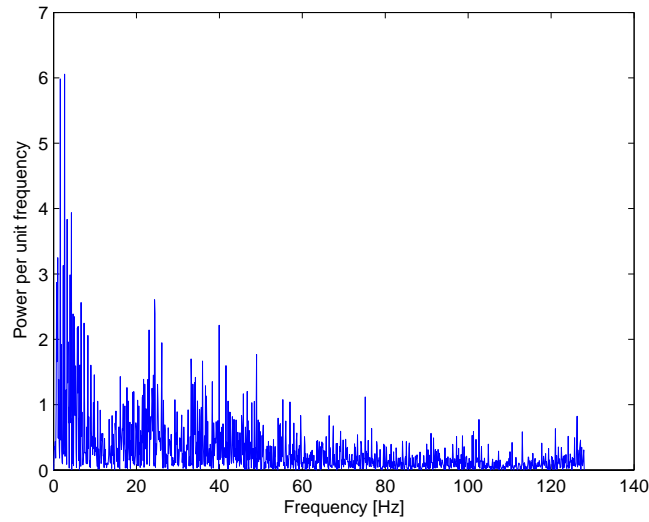


Figure 5.6: Intensity PSD during condensation at a mass flux of $250 \text{ kg/m}^2\text{s}$ and a vapour quality of 0.15

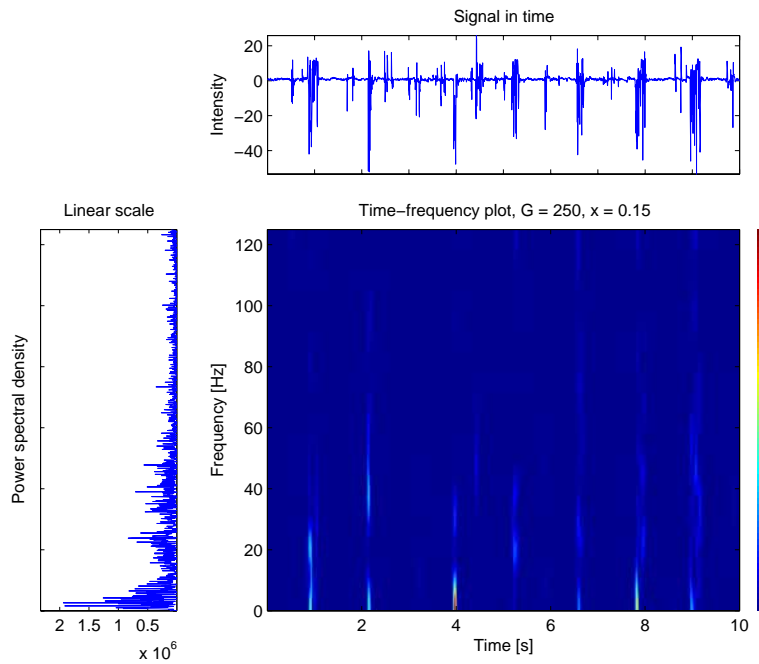


Figure 5.7: Time-frequency analysis of condensing refrigerant at $G = 250 \text{ kg/m}^2\text{s}$ and $x = 0.15$

5.2 Refrigerant in smooth tubes

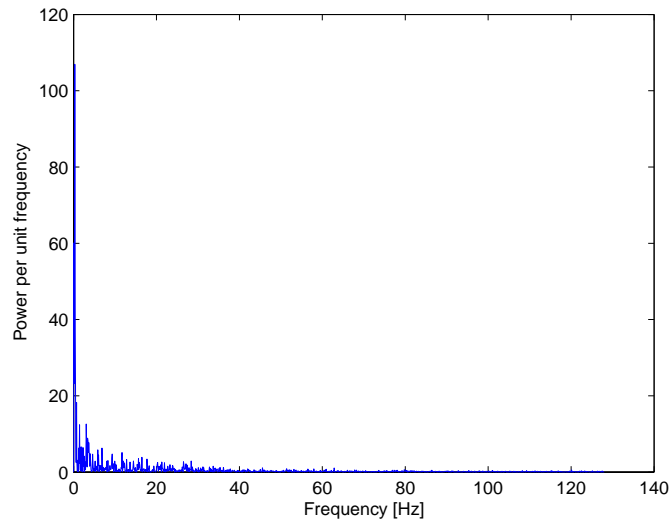


Figure 5.8: Intensity PSD during condensation at a mass flux of $300 \text{ kg/m}^2\text{s}$ and a vapour quality of 0.28

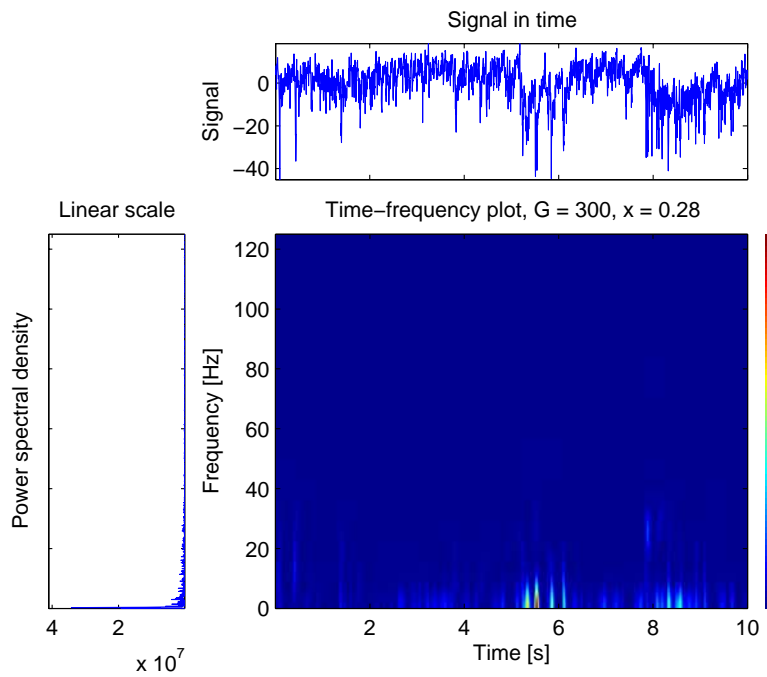


Figure 5.9: Time-frequency analysis of condensing refrigerant at $G = 300 \text{ kg/m}^2\text{s}$ and $x = 0.28$

5.2 Refrigerant in smooth tubes

was associated with shear-dominated flows and the high time-fraction allocated to shear-dominated flow is indicative of the increase in shear-dominated flow as the vapour quality increases. The appearance of this type of flow was similar to annular flow with short time periods of calmer flow.

As the transition line between intermittent flow and annular flow was approached the range of frequency activity again increased (Figure 5.12). The appearance of this flow was very similar to annular flow and the sections of calmer flow were few and far between. The gravity-dominated flows occurred when the vapour velocity dropped for a short time interval.

In the annular flow regime the magnitude of energy density dropped again (Figure 5.14). This was due to the constant low variation in the intensity signal caused by the small interfacial waves on the annulus. The range of the signal was also smaller because there was no periodic wave in the flow patterns that darkened the image. The time-frequency analysis was characterized by a large amount of activity over the entire range in time and frequency. The time-fraction at this time was 100% and the flow was annular (Figure 5.15).

It is clear that a PSD alone is deceptive because it indicates the energy levels of activity but not the time or fraction of total time that they are present in the signal. The time-frequency analysis clearly identifies the time duration that the flow has high frequencies and low frequencies and can thus be used to classify the flow for a time-fractional map.

5.2 Refrigerant in smooth tubes

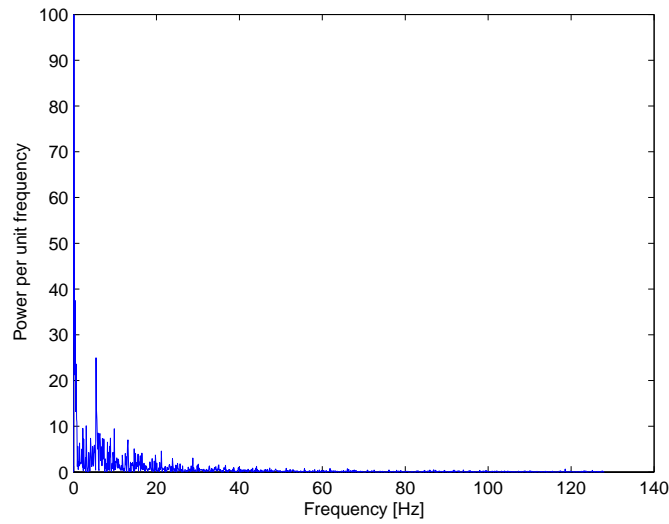


Figure 5.10: Intensity PSD during condensation at a mass flux of $300 \text{ kg/m}^2\text{s}$ and a vapour quality of 0.40

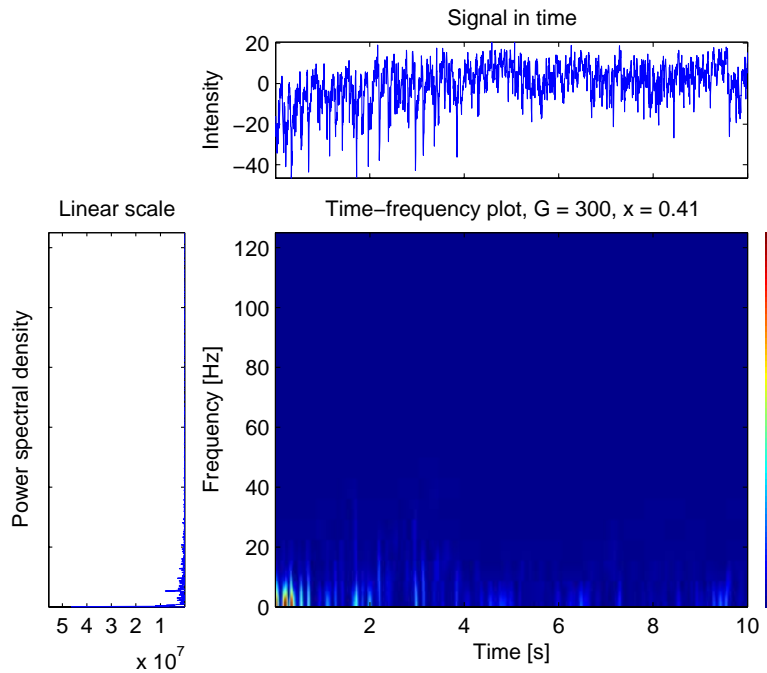


Figure 5.11: Time-frequency analysis of condensing refrigerant at $G = 300 \text{ kg/m}^2\text{s}$ and $x = 0.40$

5.2 Refrigerant in smooth tubes

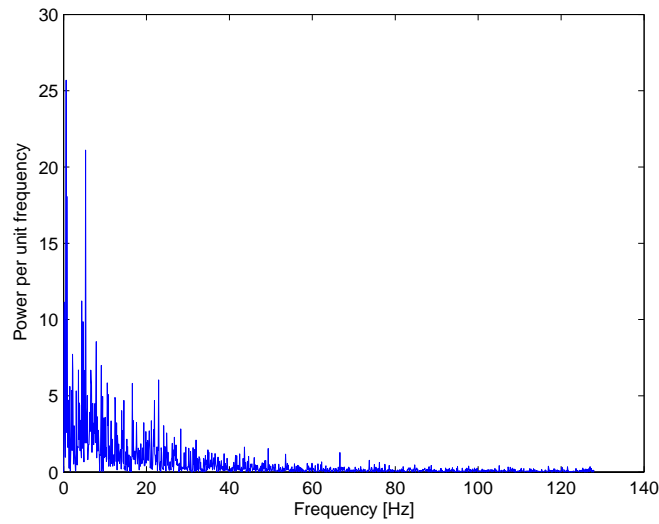


Figure 5.12: Intensity PSD during condensation at a mass flux of $300 \text{ kg/m}^2\text{s}$ and a vapour quality of 0.45

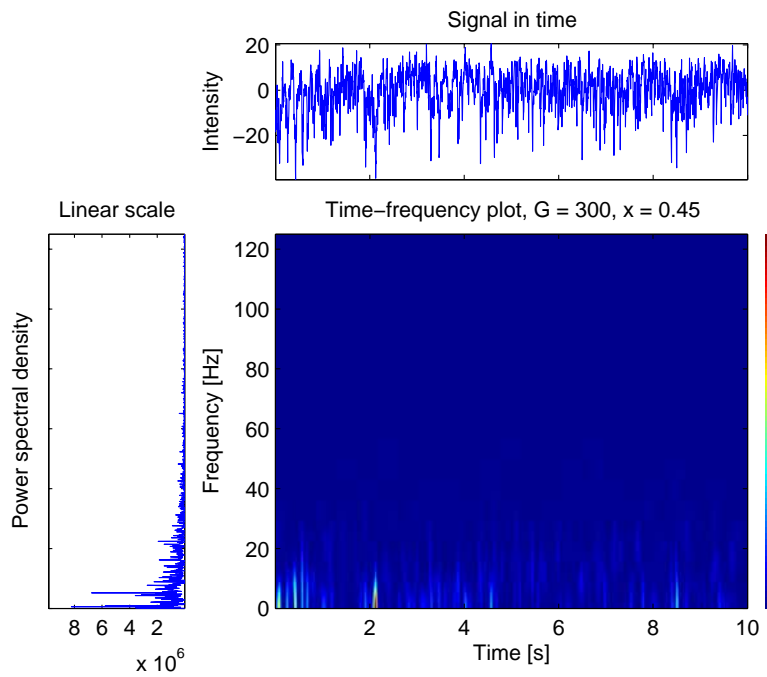


Figure 5.13: Time-frequency analysis of condensing refrigerant at $G = 300 \text{ kg/m}^2\text{s}$ and $x = 0.45$

5.2 Refrigerant in smooth tubes

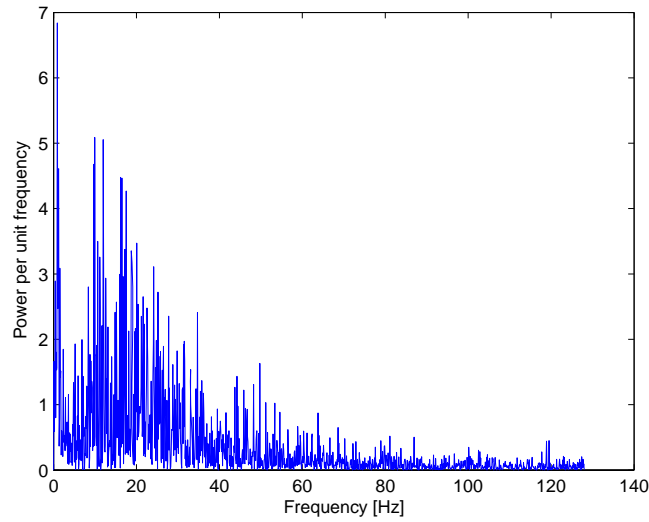


Figure 5.14: Intensity PSD during condensation at a mass flux of $300 \text{ kg/m}^2\text{s}$ and a vapour quality of 0.69

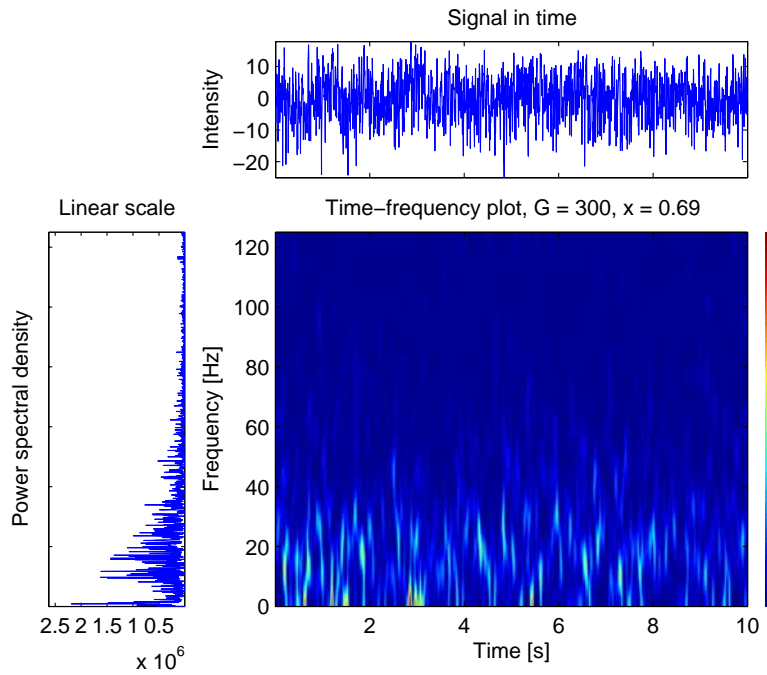


Figure 5.15: Time-frequency analysis of condensing refrigerant at $G = 300 \text{ kg/m}^2\text{s}$ and $x = 0.69$

5.2.4 Time-fractional results

The analyses of all the *.avi* video files were linked with the testing conditions and the time-fractions functions could be mapped (Table 5.4). For this analysis the logical choice of axis was vapour quality since the flow pattern map used was also a function of vapour quality. The function used to fit the data that suited the nature of the data best was a generalized linear model with binomial distribution, because this function is suited for populations that are sampled as a fraction of a total. The generalized linear model uses a binomial function to adjust for the non-linearity of the data. The link function for a binomial distribution is given in equation 5.1. In this case the total was 100% shear-dominated flow and this tended to $tf = 1$ in annular flow. The data points with the functions are presented for the individual mass fluxes (Figure 5.16). The coefficients for the binomial functions for every mass flux are given in Table 5.5. The uncertainty in the time-fractional method produced the spread in data points and the most important effect captured here was the trend of the time-fractions and not the exact values. In general, the low vapour qualities and mass fluxes resulted in the lower time-fractions and thus more gravity-dominated flows. The higher mass fluxes did not result in very low time-fractions and the persistence of the annular flow regime was noted at the transition vapour quality between annular and intermittent flow.

$$\begin{aligned}
 y^* &= a + bx \\
 \text{so that } y &= g'(y^*) \\
 \text{where } g(\mu) &= \ln \frac{\mu}{1 - \mu}
 \end{aligned}
 \tag{5.1}$$

The magnitudes of time-fractional numbers between the different mass fluxes and the functions are presented together. The trend did not follow in chronological order of mass flux as expected but were close together. This was the result of variations in the flow and the precision of the method. The trends were repeatable and followed an increasing trend in time-fractional number as mass flux increased (Figure 5.17).

5.2 Refrigerant in smooth tubes

Table 5.4: The time-fraction results for R-22 condensing at 40 °C

G	x	tf	G	x	tf	G	x	tf
247.43	0.38	0.78	645.45	0.42	0.85	504.13	0.14	0.35
249.46	0.42	0.80	647.48	0.36	0.72	505.21	0.41	0.85
250.72	0.31	0.42	649.58	0.20	0.62	514.58	0.54	1.00
650.04	0.63	1.00	396.91	0.50	1.00	543.42	0.05	0.54
250.95	0.49	0.87	397.48	0.16	0.32	250.80	0.11	0.56
252.37	0.10	0.42	250.42	0.20	0.36	544.65	0.33	0.73
251.16	0.25	0.44	398.51	0.39	0.70	548.20	0.65	1.00
252.89	0.08	0.48	400.54	0.65	1.00	549.61	0.42	0.90
253.02	0.35	0.45	401.23	0.32	0.65	548.31	0.50	1.00
298.69	0.69	1.00	400.56	0.57	1.00	548.16	0.19	0.65
299.66	0.51	1.00	400.91	0.69	1.00	552.15	0.42	0.92
299.57	0.56	1.00	401.89	0.25	0.56	553.32	0.14	0.61
300.43	0.29	0.41	403.11	0.45	0.86	553.32	0.14	0.61
249.56	0.56	0.97	403.84	0.25	0.56	552.97	0.27	0.64
300.81	0.34	0.46	400.84	0.11	0.46	555.86	0.42	0.91
300.11	0.64	1.00	445.45	0.11	0.34	251.71	0.12	0.20
298.14	0.70	1.00	250.42	0.39	0.78	594.19	0.39	0.79
301.38	0.45	0.83	447.64	0.42	0.81	598.06	0.23	0.65
303.00	0.20	0.40	449.10	0.17	0.39	596.99	0.48	1.00
305.25	0.41	0.75	448.54	0.31	0.65	597.16	0.09	0.46
316.71	0.37	0.71	453.02	0.18	0.30	598.46	0.44	0.94
346.39	0.25	0.39	450.80	0.25	0.50	597.36	0.34	0.68
345.76	0.61	1.00	453.87	0.47	0.93	616.15	0.66	1.00
346.85	0.13	0.29	452.03	0.53	1.00	601.71	0.28	0.68
250.69	0.15	0.30	495.67	0.59	1.00	602.42	0.08	0.46
346.66	0.17	0.29	497.38	0.23	0.52	605.18	0.56	1.00
347.86	0.31	0.61	497.88	0.31	0.60	251.16	0.27	0.44
348.42	0.42	0.81	250.54	0.64	1.00	605.45	0.66	1.00
348.52	0.46	0.89	498.62	0.17	0.46	615.59	0.12	0.49
350.30	0.49	0.92	497.87	0.20	0.52	634.61	0.24	0.64
351.64	0.56	1.00	500.83	0.51	1.00	636.94	0.53	1.00
351.97	0.38	0.74	504.14	0.02	0.35	642.60	0.11	0.48
355.28	0.68	1.00	504.13	0.36	0.64	642.75	0.14	0.56

5.2 Refrigerant in smooth tubes

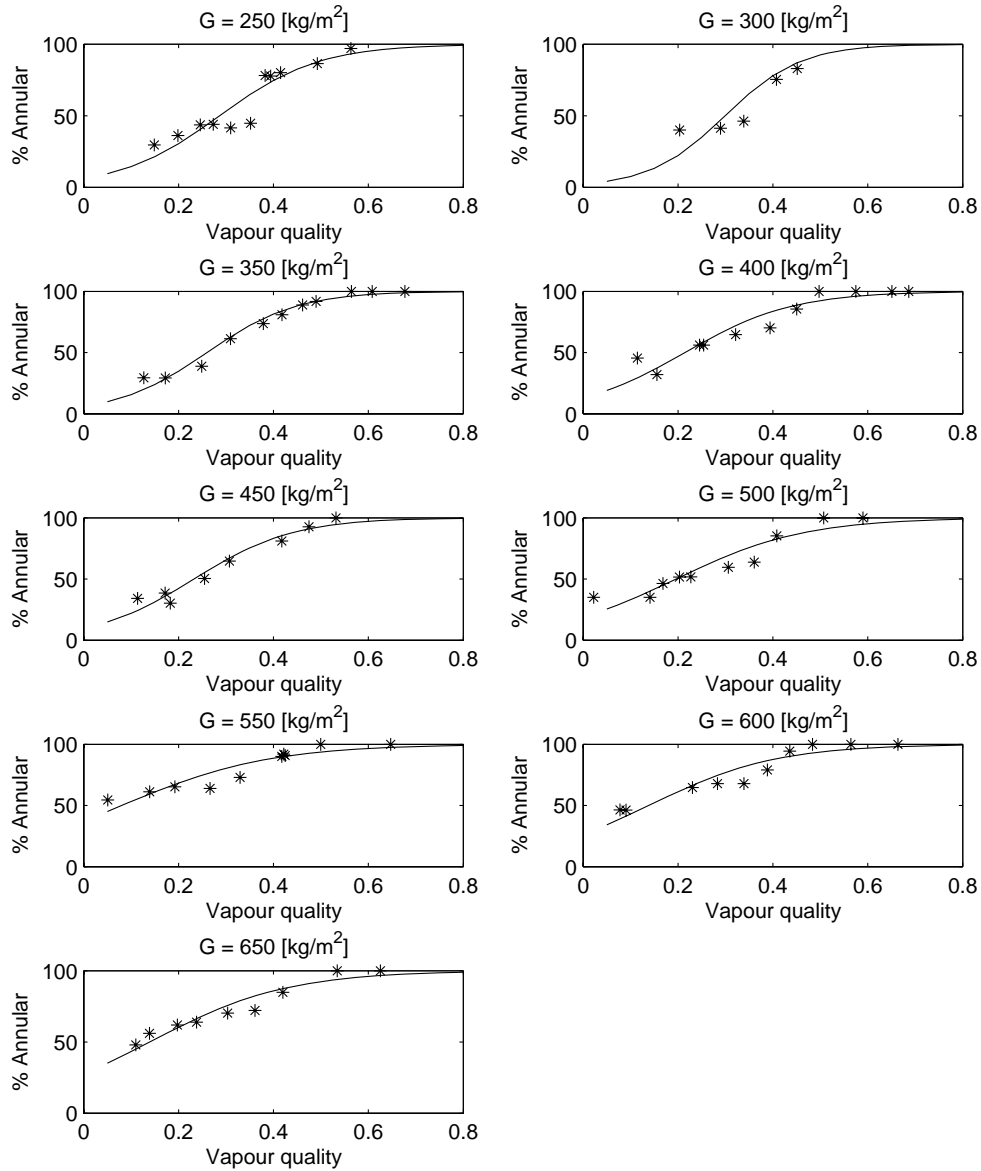


Figure 5.16: The analysis results for all mass fluxes tested with R-22

The time-fractional map of two-phase flow was superimposed on a El Hajal *et al.* (2003) flow pattern map over the intermittent flow regime (Figure 5.18).

5.2 Refrigerant in smooth tubes

Table 5.5: Binomial function coefficients for all mass fluxes of condensing refrigerant tested

Mass flux kg/m^2s	a	b
250	-2.7284	9.5330
300	-3.7793	12.6279
350	-2.7472	10.5808
400	-1.8879	8.7990
450	-2.2216	9.5526
500	-1.4423	7.3697
550	-0.5159	6.4147
600	-1.0283	7.4399
650	-0.9613	6.9042

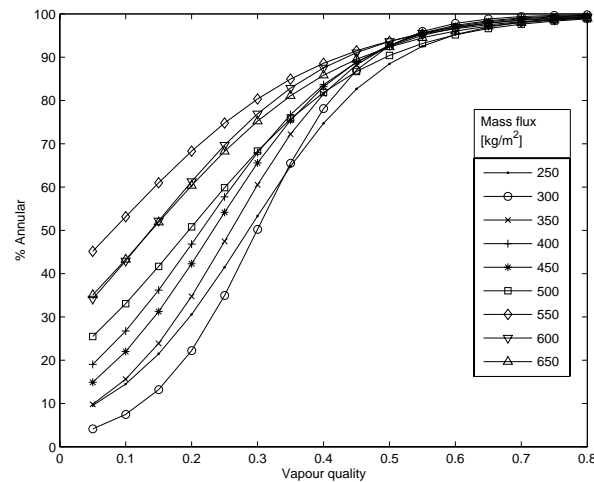


Figure 5.17: Combined time-fractional results for condensing R-22 at 40°C

The fraction of time that shear-dominated flows occurred, increased with vapour quality over the range of intermittent flow towards annular flow. The surface was also sloped positively in the direction of higher mass flux.

Based on the time-fractions and visual observations it was noted that there was a change in the dominant flow patterns from a shear-dominated annular film

5.2 Refrigerant in smooth tubes

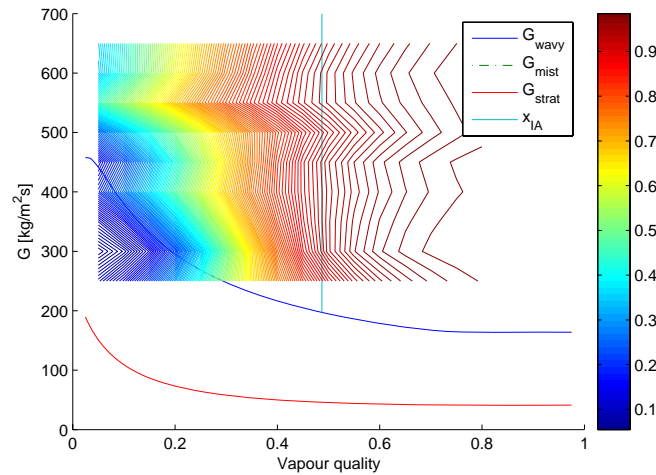


Figure 5.18: Time-fractional map superimposed on a El Hajal *et al.* (2003) flow pattern map for condensing refrigerant

type of flow to a gravity dominated stratified type of flow at lower vapour qualities. Most specifically this was at vapour qualities less than 0.25 and is an intermittent occurrence that becomes very strongly noticeable in the region from 0.10 to 0.25 vapour quality. This occurrence at lower vapour qualities is most likely the reason for many flow pattern maps, when compared with the El Hajal *et al.* (2003) flow map, to have a transition line defined at about this location (El Hajal *et al.*, 2003). The Cavallini *et al.* (2002) flow pattern map defines a transition through the intermittent flow regime. According to their transition annular flow is more persistent at high mass fluxes during condensation. The transition zone used by Cavallini *et al.* (2002) is not well defined but it is based on flow correlations and heat transfer behaviour. The Tandon *et al.* (1982), Soliman (1982) and Dobson and Chato (1998) flow pattern maps have similar transitions. The transition line that these methods predict is not consistent because of their large room for interpretation in the ambiguous intermittent flow regime.

These flow pattern maps all attempt to predict a transition that is based on stochastic behaviour that is difficult to classify. The subjectivity in discriminating between these flow patterns leads to the variation of the predicted transition. The time-fractional method does not attempt to define this boundary with a single function but rather to represent the actual flow behaviour and to model the flow

based on a continuous function of statistical origin.

5.3 Pressure signal and void fraction

The test section was instrumented with pressure transducers for measuring the pressure drop over the test section. These pressure transducers were also used to collect data for a frequency and time-frequency analysis. The same can be said for the void fraction sensor data. The data were captured at a hardware timed and set frequency of 256 Hz. This was done to coincide with the sampling frequency of the video camera and the void fraction sensor that had a limit on its maximum sampling frequency. Both these signals were sampled with the intent of comparing the time-frequency analysis and time-fractional results between the various methods. The results of both these methods were not as ideal as expected and a discussion of the data and conclusions follows.

5.3.1 Pressure signal

The pressure signal used for analysis was the raw milliamp signal from the transducer because the signal was merely scaled for pressure reading. The frequency domain analysis of the signals coincided well with the predictions given in Liebenberg (2002) for the flow regimes observed in the experiments. Figure 5.19 is a typical result for annular flow and shows the wide range of frequency activity. The unique frequency range for annular flow was the range of frequencies above 100 Hz.

Intermittent flow was characterized by activity at many frequencies over the range of flow conditions that could be classified as intermittent (Figures 5.20 and 5.21). The time frequency analysis of these signals could not provide a strong indicator of the nature of the flow. The intermittent flow regime is chaotic in nature and in order to successfully classify the intermittent regime into two sub regimes as proposed in this dissertation required a good indicator. The second drawback of using the pressure signal, if there was no strong frequency or other signal characteristic present that could be identified, was the lack of a method to verify the results and relating the signal to flow patterns. For the reasons given

5.3 Pressure signal and void fraction

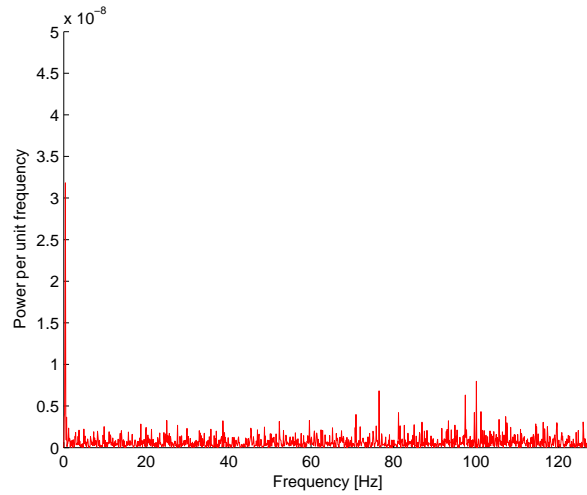


Figure 5.19: Annular flow pressure PSD during condensation at a vapour quality of 0.65

above the signal analysis of pressure signals in the time-frequency domain was not pursued further. This does not rule out the possibility of successful analysis of pressure signals with this method using more accurate methods and improved conditioned signals.

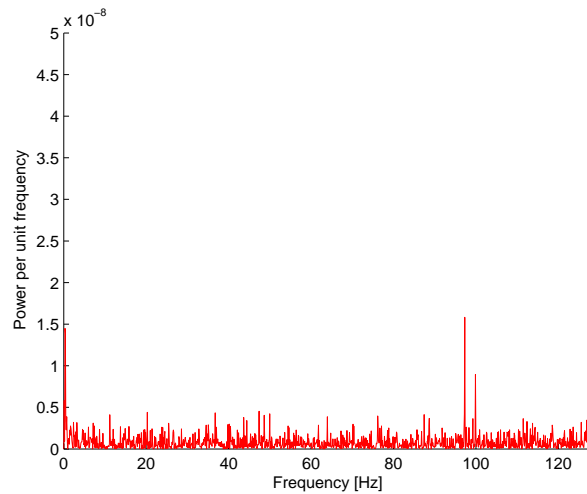


Figure 5.20: Intermittent flow pressure PSD during condensation at a vapour quality of 0.45

The low vapour qualities were made up of slug and plug flow and had fluctuat-

5.3 Pressure signal and void fraction

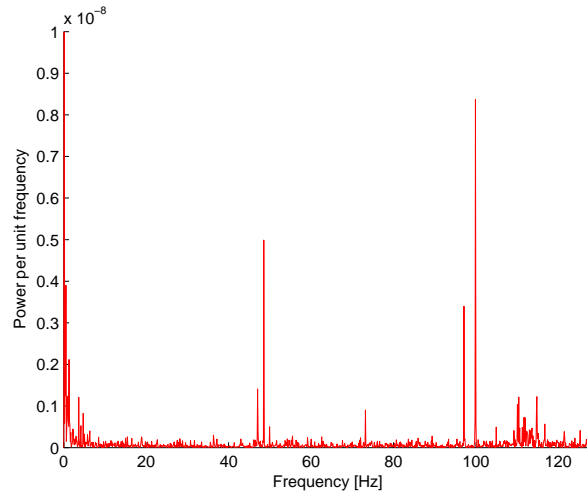


Figure 5.21: Intermittent flow pressure PSD during condensation at a vapour quality of 0.25

ing pressures (Figure 5.22). The PSD of this signal had stronger energy densities at more frequencies than intermittent flow at higher vapour qualities. The high peaks at 50 Hz and 100 Hz was assumed to be noise from electronic equipment.

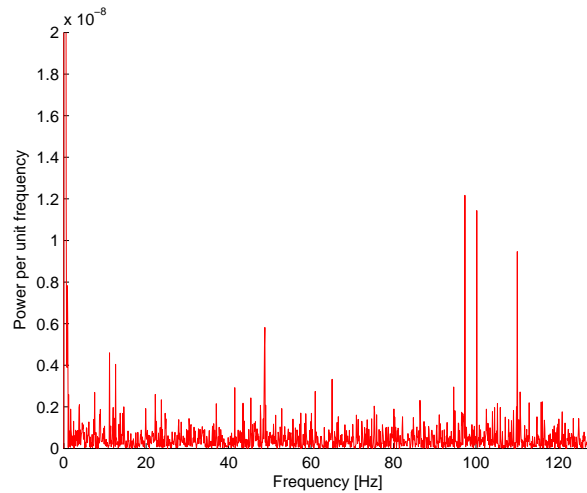


Figure 5.22: Slug flow pressure PSD during condensation at a vapour quality of 0.13

5.3 Pressure signal and void fraction

5.3.2 Void fraction

The void fraction sensor was also employed in the experiment even though it is still under development in Belgium at University of Gent. The sensor had been tested extensively in air-water systems with encouraging results. The application of the sensor to refrigerant flow has, however, not been as well tested. The first drawback to take note of is the low dielectric coefficients of refrigerants. Compared to water and air which produce a difference of 7 to 10 Volts refrigerant will result in a 3 Volt difference between liquid and vapour at best. The dynamic characteristic of the signal is the component used in the analysis and thus the difference just mentioned should not influence the results. It should be noted that these are the first experimental results from the capacitive void fraction sensor for refrigerant flow and that the device is still under development.

The signal analysis done on the void fraction voltage signal usually includes normalising the signal by the full scale liquid to gas difference. The effects of oil and the thin annular film always present in refrigerant condensation are also unknown. The conduction effect that is obtained from using water that contains minerals and that strongly influences the sensor should be minimal in the refrigerant (Canière, 2007). The dynamics of the signal were used for analysis in this study. The setup and operation of the sensor in refrigerant flow will need more development.

The PSD of the void fractional signal did not change much for different flow conditions. It was clear that the noise present at 120 Hz and higher came from the sensor electronics and was a function of the gain setting. The origin of frequency activity at 30 Hz to 50 Hz is not clear and could be a result of the flow patterns (Figure 5.23). The time-frequency analysis did not produce any conclusive results.

At a vapour quality of 0.34 in the middle of the intermittent flow regime the PSD only showed slight changes (Figure 5.24). The noise at 120 Hz had a large energy density and the band between 30 and 50 Hz had higher energy activity compared with the rest of the signal.

In the annular flow regime the magnitude of energy density dropped in the 30 to 50 Hz band (Figure 5.25). The peak at 50 Hz was suspected to be a result of electric noise picked up by the cables. The reason for a drop in energy levels

5.3 Pressure signal and void fraction

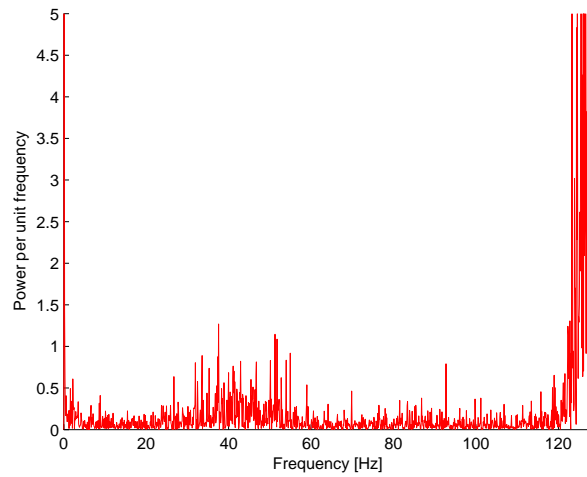


Figure 5.23: Intermittent flow void fraction PSD during condensation at a vapour quality of 0.20

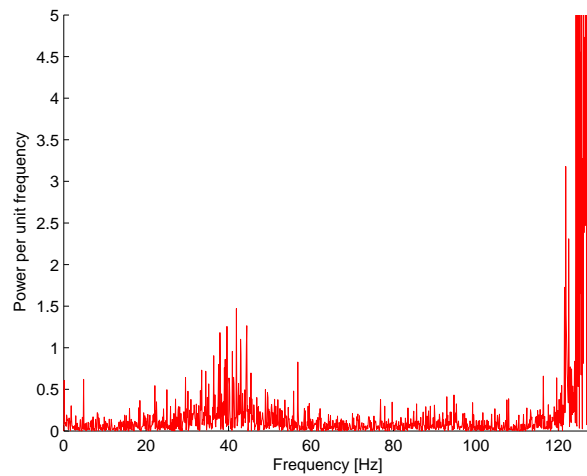


Figure 5.24: Intermittent flow void fraction PSD during condensation at a vapour quality of 0.34

could be the result of annular flow. Annular flow was difficult to detect because of the film around the perimeter of the tube that resulted in a false signal.

5.3 Pressure signal and void fraction

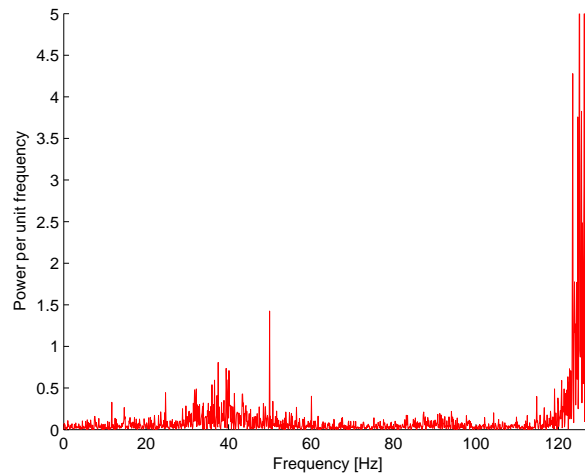


Figure 5.25: Intermittent flow void fraction PSD during condensation at a vapour quality of 0.65

5.3.3 Conclusion

The signals from the pressure transducers did not perform as expected based on the unclear differences in the PSD analysis of these signals. The use of these signals were, however, not studied in depth and should not be neglected in future. The milliamp pressure transducers are sensitive to noise and the methods of analysis used in this study remain crude. An improvement on both these aspects could result in better signal with the necessary characteristics for the application of time-frequency analysis.

The void fraction sensor is still under development and the signal amplification device used is still of the first generation. The sensor performed well in delivering a dynamic signal and the possibility that an accurate void fraction sensor with correct settings and use can contribute to flow pattern recognition will be a helpful tool in the analysis of intermittent flow. Using the void fraction sensor correctly will surely result in improvement of the signal if the negative effects of annular films and oil are negligible.

5.4 Results on correlations

The purpose of time-fractional mapping is to investigate the possibility that such a factor, when applied to the correct heat transfer equation can lead to better predictions of heat transfer coefficients. If this is not possible the contribution of time-fractional mapping to the understanding of intermittent two-phase flow physics and transitions in flow patterns is the secondary goal. The experiment conducted resulted in quality heat transfer data being collected and the heat transfer aspect of this study is dealt with in full detail in the dissertation by Christians-Lupi (2007). The figures presented in this section are courtesy of Christians-Lupi (2007). The general heat transfer model used for intermittent flow is an extension of the annular flow correlation into low vapour qualities. The method proposed here adjusts this correlation by taking into account the drop in shear force dominated flow and subsequent gravity dominated flows.

Figure 5.26 is a validation that the heat transfer data collected compares well with Thome *et al.* (2003), which is an established and well used correlation set.

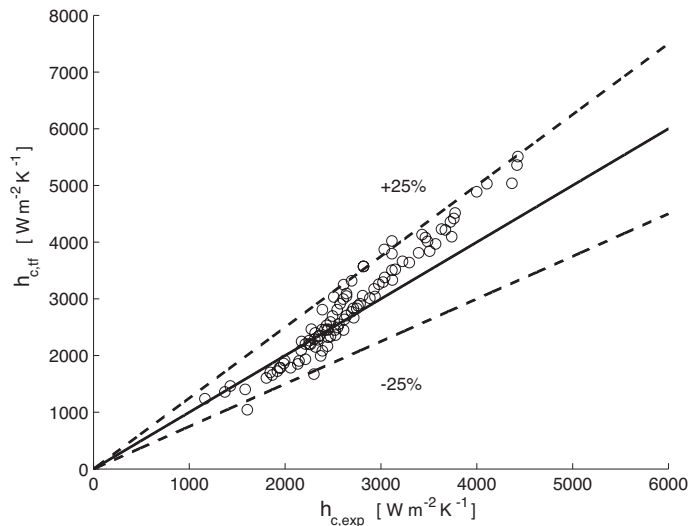


Figure 5.26: Comparison of experimental heat transfer measurements and the Thome *et al.* (2003) correlations

The time-fractional correction applied to the data set resulted in a definite improvement. The standard deviation between the experimental data and the Thome *et al.* (2003) correlation dropped from 13% to 10% (Figure 5.27). This

5.4 Results on correlations

deviation indicates that the heat transfer model of Thome *et al.* (2003) can be modified with the present suggested model and the result is a better correlation with actual measured heat transfer coefficients. For a detailed discussion of heat transfer data see Christians-Lupi (2007). The heat transfer at low vapour qualities had the largest improvement. This was expected where the shear-dominated model does not predict heat transfer phenomena present in the flow at all times.

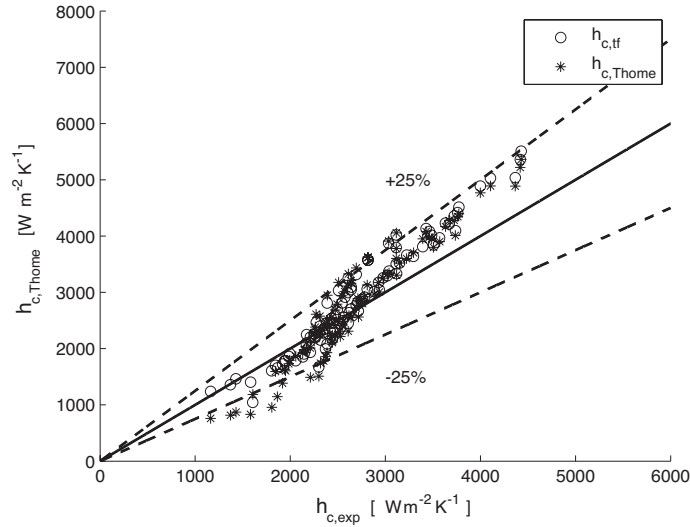


Figure 5.27: Heat transfer measurements after time-fractional correction

A sample case of the magnitudes of heat transfer correlations for mass flux $300 \text{ kg/m}^2\text{s}$ indicated the relative effect of time-fractions (Figure 5.28). The stars indicate the gravity dominated heat transfer correlation. The gravity dominated, stratified flow, correlation has a positive slope and drops below the shear-dominated, annular flow, correlation at the x_{ia} transition line. The triangles indicate the time-fractional total heat transfer coefficient and the time-fractional effect becomes less as the tf number approaches one and the shear-dominated correlation becomes the only effective correlation in annular flow.

The time-fractional map was applied to pressure drop predictions in Christians-Lupi (2007) based on the data from this study. The correlations used are described in Christians-Lupi (2007) and include the latest results for annular and intermittent flow. The Müller-Steinhagen and Heck correlation is used for annular flow and the Grönnerud correlation for intermittent flow. The pressure

5.5 Conclusion of this chapter

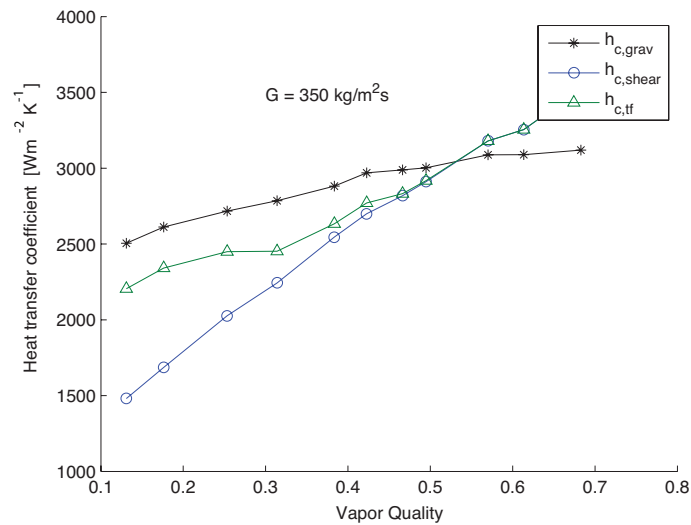


Figure 5.28: The heat transfer correlations used in the time-fractional correction at $G = 350 \text{ kg/m}^2\text{s}$

data collected during the experimental testing were not accurate enough for correlation purposes but could be used for this thought experiment. The problem with pressure drop correlations in two-phase flow is the discontinuity between the models. Applying the time-fractional correction to pressure drop data removes this discontinuity (Figure 5.29). A complete discussion of the pressure data and correlations can be found in Christians-Lupi (2007).

5.5 Conclusion of this chapter

The methods to analyse and predict time-fractions in intermittent flow were developed and applied to intermittent refrigerant flows with success. The methods used worked and valuable insight was gained on intermittent flow and analysis techniques. The time-fractional map developed was applied to heat transfer and pressure drop data by Christians-Lupi (2007). The results were an improvement in heat transfer prediction and the elimination of a step discontinuity in pressure drop predictions. The pressure drop data cannot be used for correlations but changes in measurement devices will solve the problem. The validation of time-fractional mapping on other data sets will prove the usefulness of this method.

5.5 Conclusion of this chapter

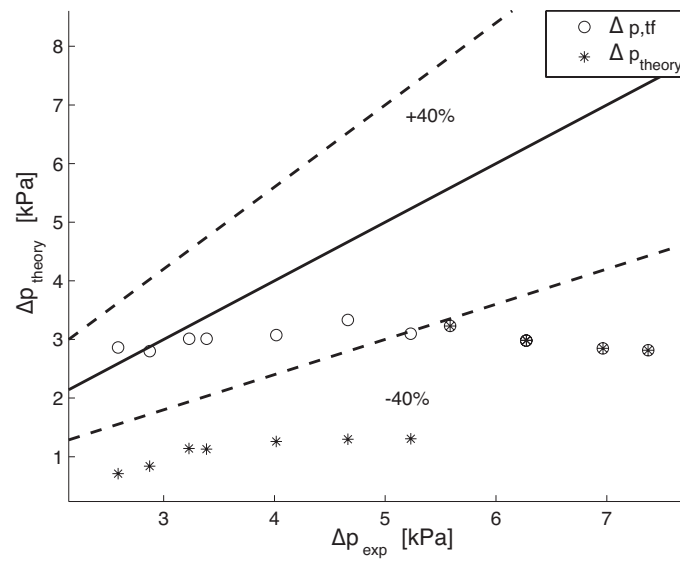


Figure 5.29: Results of time-fraction on pressure drop prediction at $G = 400 \text{ kg/m}^2\text{s}$ (Christians-Lupi, 2007)

Chapter 6

Conclusions

6.1 Introduction

The conclusions made in this section apply to the methods developed and applied during the course of the study. The investigation focussed on refrigerant testing and the time-fractional mapping of intermittent flow. The correction of heat transfer and pressure drop correlations with time-fractions and the findings with respect to the hypothesis in Chapter 4 are presented here.

6.2 Consolidation of work done

Initially air-water tests were carried out and did not require significant financial investment. Air-water was found to be ideal for validation purposes. The air-water test section was instrumented with pressure transducers and a void fraction sensor. The frequency data from all these measurements were analysed for potential time-frequency to time-fraction conversion.

The conceptual design of the refrigerant testing facility was conducted in collaboration with Christians-Lupi (2007). The building and detailed design was commissioned to M-Tech Industrial, a company that specialises in heat pump design and manufacture. After delivery of the system it was instrumented and debugged. A software program was written to control the system and to give real-time feedback of the overall state of the system. The supervision and installation

6.2 Consolidation of work done

of the water-side pipe network and dual function heat pump to run the system independently from other laboratory activities was done. Several test sections (including air-water, refrigerant and Wilson plot test sections) were designed and built. The test sections were instrumented with thermocouples, pressure transducers, coriolis flow meters, void fraction sensors and high-speed cameras.

The oil concentration was measured at various operating conditions and the highest percentage of oil found in the refrigerant was 2.3%. This was found at high mass flow and lower mass flows produced lower oil concentrations in the order of 0.6%. The oil concentration in the refrigerant was a function of operating conditions, but remained low overall.

The shortcomings expected in signal analysis with conventional methods led to the development of an objective vision based method that was validated by air-water testing and applied to refrigerant flow with successful results in both. This method involved the programming of a National Instruments Vision program to configure the camera and buffering of data. The video sequences were then analysed in LabView to investigate the frequency, amplitude and time-frequency domains. The flow patterns were observed in the sight glass with reference to the El Hajal *et al.* (2003) flow patterns map. The annular transition predicted by x_{ia} was found accurate with slight delay at higher mass fluxes. The vapour quality range from x_{ia} to 0.25 had a strong annular appearance with the addition of larger waves and an unstable, thickening annular film as the vapour quality decreased. As the vapour quality decreased the appearance of intermittent behaviour increased. The nature of intermittent occurrences in the flow included waves, liquid entrainment, increasing stratification and eventually the tube was closed off by liquid waves at the lowest of vapour qualities. The vapour qualities between 0.25 and 0.15 consisted of distinct flow pattern changes between shear-dominated and gravity-dominated conditions. The vapour qualities of less than 0.15 consisted of slug flow and plug flow with increasing liquid fractions and entrained vapour bubbles.

The experimental work was done with R-22 and the testing involved calculation of heat transfer coefficients, pressure drop, void fraction and high-speed videography. The analysis of the signals for time-fractional purposes involved high-speed video, pressure and void fraction signals. The video analysis was

6.3 Final conclusion and future suggestions

found most productive for the purposes of discriminating flow patterns. The other methods applied in this study suffered from data acquisition and signal conditioning problems. The time-fractions of shear versus gravity-dominated flow were mapped out over the test range and curve fit coefficients are provided.

The time-fractional map was applied with success to heat transfer and pressure drop predictions. This resulted in an improvement in predictions of both correlations. Thus the hypothesis stating that the sub classification of flow regimes into compositional flow patterns and adapting the correlations can be accepted on these grounds. The heat transfer model used the annular flow correlation for shear-dominated flow and the stratified flow correlation without the stratified to stratified-wavy multiplier term for gravity-dominated flow. The pressure drop model was improved by using the Müller-Steinhagen and Heck correlation for annular flow and the Grönnerud correlation for intermittent flow.

6.3 Final conclusion and future suggestions

The study involved a wide range of aspects concerning two-phase flow experimentation. Included were the design of an experimental system, the instrumentation of a system with measurement devices of a wide range, the programming of a complex control and calculation program and the development of a unique measurement technique. Various experimental systems and experimentation techniques were used during parts of the study including validation of a capacitive void fraction sensor in an air-water system and later in a refrigeration system, Wilson plot techniques, air-water validation of optical measurement techniques and extensive testing and development with the refrigeration test equipment.

The optical method proved accurate for detecting frequencies when applied to two-phase flow pattern detection. The method proved to be invaluable for the work done in this study related to the subclassification of two-phase flows in the intermittent regime. The method is however still crude and further development should be done. Such development could include a study with a faster frame rate and then the use of different analysis areas. The analysis of a visual signal or image itself could also lead to different and hopefully more accurate or descriptive methods (Jassim, 2007). This type of work could involve wavelet transforms,

6.3 Final conclusion and future suggestions

different time-frequency analysis, amplitude domain analysis and many more. The amount of work on the signal analysis side is limitless and could include more advanced techniques or just simple signal normalization. The analysis of signals with different statistical methods and in the amplitude domain may result in even simpler and easier analysis methods based on statistical distributions. If accurate and repeatable results can be achieved the method may even help define transition boundaries between other flow regimes more accurately. This would also assist in adapting flow pattern maps for enhanced tubes and a variety of other conditions. The analysis of unstationarity in signals can also assist in defining transition boundaries and may be used to identify subtleties in flow patterns that are difficult to detect.

The use of a laser with a light sensitive diode as pick-up can also be investigated for macro scale tubes. The advantage of such a system being high sample rates and reduced costs compared to a high-speed camera.

The time-fractional map, although proven as a method to improve the heat transfer and pressure drop predictions is also a very crude model and needs to be expanded into a unified map or function that can be applied to the correlations based on the physical properties of the fluids. The model can also with significant work and the use of good flow regime descriptors, be applied to a wide range of flow patterns and the entire flow pattern map. If this option is investigated and found suitable a flow pattern map based on time-fractions can be set up without discrete transitions but with statistical functions that continuously flow from one regime to the next.

The time-fractional mapping method should also be applied to other data sets as validation. This is easily done for the refrigerants tested but the model also needs to be improved by testing more refrigerants and developing a unified map based on physical properties. This model can then be validated on a wide range of refrigerants and data from many laboratories.

It can be noted that most researchers define flow pattern transitions with similar functional outcomes. The only discrepancy comes from the transitions of intermittent flow. Some separate and define multiple regimes (Baker, 1954; Tandon *et al.*, 1982) within intermittent flow. Others find a separation parameter in heat transfer data that defines the transition (Cavallini *et al.*, 2006). The

6.3 Final conclusion and future suggestions

intermittent transition is also defined by the transition from a shear-dominated regime to a gravity dominated regime (Cavallini *et al.*, 2002). All these transitions can be observed in the flow patterns as the mass flux and vapour quality changes. The large variation is testament to the subjective nature of flow pattern prediction. The method presented in this study, and the study of Jassim (2007), is not to define a transition function for intermittent flow but to use statistical samples, analysed so that the most probable composition of the flow can be predicted accurately. Because the heat transfer and pressure drop models are a strong function of the prevailing flow pattern, this probabilistic result can then be incorporated into the models to improve their accuracy.

References

- S. Abu-Eishah. Correlations for the thermal conductivity of metals as a function of temperature. *Int. Journal of Thermophysics*, 22:1855–1868, 2001. 157
- AFEAS. Montreal Protocol on Substances that Deplete the Ozone Layer. www.afeas.org/montreal_protocol.html, Arlington, 2002. 2
- W. Akers and H. Rosson. Condensation inside a Horizontal Tube. *Chemical Engineering Progress Symposium Series*, 56:145–150, 1960. 19
- W. Aoudi, H. Liebgott, A. Needles, V. Yang, F. Foster, and D. Vray. Estimation methods for flow imaging with high frequency ultrasound. *Ultrasonics*, 44:135–140, 2006. 17
- ASHRAE. Ashrae standard 41.4: Method for measurement of proportion of lubricant in liquid refrigerant. Technical report, ASHRAE, 2006. 109
- O. Baker. Simultaneous Flow of Oil and Gas. *The Oil and Gas Journal*, 53:185–195, 1954. 5, 18, 20, 140
- G. Breber, J. Palen, and J. Taborek. Prediction of Horizontal Tubeside Condensation of Pure Components using Flow Regime Criteria. *Journal Heat Transfer*, 102:471–476, 1980. ix, 18, 22, 23, 40
- J. Bukasa, L. Liebenberg, and J. Meyer. Heat transfer performance during condensation inside spiralled microfin tubes. *Journal of Heat Transfer*, 126:321–328, 2004. ix, 26
- H. Canière. Void fraction sensor. Private e-mail conversation 16-March-07, March 2007. 130

- A. Cavallini, G. Censi, D. D. Col, L. Doretto, G. Longo, and L. Rossetto. In-tube Condensation of Halogenated Refrigerants. *Int. Journal HVAC&R Research*, 8:146 – 161, 2002. 18, 31, 42, 126, 141
- A. Cavallini, D. D. Col, L. Doretto, M. Matkovic, L. Rossetto, C. Zillio, and G. Censi. Condensation in Horizontal Smooth Tubes: A New Heat Transfer Model for Heat Exchanger Design. *Heat Transfer Engineering*, 27:31–38, 2006. 3, 30, 31, 42, 43, 140
- J. Cha, Y. Ahn, and M. Kim. Flow measurement with an electromagnetic flowmeter in two-phase bubbly and slug flow regimes. *Flow Measurement and Instrumentation*, 12:329–339, 2002. 16
- K. Cho, K. Sin, and Y. Lee. Impedance imaging of two-phase flow field with mesh grouping method. *Nuclear engineering and design*, 204:57–67, 2001. 17
- M. Christians-Lupi. Flow pattern-based heat transfer and pressure drop correlations for condensing refrigerants in smooth tubes. Master's thesis, University of Pretoria, Department of Mechanical and Aeronautical Engineering, 2007. xii, 5, 110, 133, 134, 135, 136, 137, 165, 168
- S. Coetsee. The Development of an Experimental set-up to investigate Heat Transfer Enhancement in tube-in-tube Heat Exchangers. Master's thesis, Rand Afrikaans University, Department of Mechanical Engineering, 2000. 151
- J. Collier and J. Thome. *Convective Boiling and Condensation*. Clarendon Press, Oxford, 3rd edition, 1994. ix, 11, 88
- M. De Paepe, H. Canière, C. T'Joel, H.-J. Steeman, A. Willockx, M. Christians, E. van Rooyen, L. Liebenberg, and J. Meyer. Refrigerant flow regime detection with a capacitance void fraction sensor. *9th AIAA/ASME Joint Thermophysics and Heat Transfer Conference, 3-8 June, San Francisco, California*, 1:12, 2006. 16, 68, 82
- P. de Vos. *Condensation and evaporation of R410a in internally grooved enhanced tubes*. M Tech industrial, 2005. 69

- M. Dobson. *Condensation in horizontal tubes*. PhD thesis, University of Illinois at Urbana-Champaign, 1994. ix, 12, 21, 22, 26, 40, 42, 43
- M. Dobson and J. Chato. Condensation in Smooth Horizontal Tubes. *Journal of Heat Transfer*, 120:193–213, 1998. xiii, 9, 12, 19, 22, 27, 28, 29, 40, 41, 42, 43, 46, 89, 126
- J. El Hajal, J. Thome, and A. Cavallini. Condensation in Horizontal Tubes, Part 1: Two-Phase Flow Pattern Map. *Int. Journal Heat Mass Transfer*, 46(18): 3349–3363, 2003. doi: 10.1016/S0017-9310(03)00139-X. ix, xii, 3, 4, 15, 18, 19, 29, 34, 37, 38, 39, 40, 41, 43, 46, 69, 124, 126, 138, 168
- K. Elkow and K. Rezkallah. Void fraction measurements in gas-liquid flows using capacitance sensors. *Measurement Science Technology*, 7:1153–1163, 1996. 16
- GAW. Scientific assessment of ozone depletion. *Scientific Assessment Panel of the Montreal Protocol on Substances that Deplete the Ozone Layers*, August: 1–3, 2006. ix, 2, 3
- K. Hashizume. Flow Pattern and Void Fraction of Refrigerant Two-phase Flow in Horizontal Pipe. *Bulletin of JSME*, 26:1597 – 1602, 1983. 18
- E. Hervieu and P. Seleglim. An objective indicator for two-phase flow pattern transition. *Nuclear Engineering and Design*, 184:421–435, 1998. 47, 92, 94
- M. Hubbard and A. Dukler. The Characterization of Flow Regimes for Horizontal Two-phase Flow: Statistical Analysis of Wall Pressure Fluctuations. *Proceedings of the 1966 Heat Transfer and Fluid Mechanics Institute*, 39:100–121, 1966. 16
- E. Jassim. *Probabilistic flow regime map modelling of two-phase flow*. PhD thesis, University of Illinois at Urbana-Champaign, 2007. 33, 139, 141
- O. Jones and Z. Zuber. Statistical Methods for Measurement and Analyses of Two-Phase Flow. *Heat transfer 1974: Proceedings of the 5th Int. Heat Transfer Conference*, 5:200 – 204, 1974. 16

- A. Jowarek and A. Krupa. Gas/liquid ratio measurements by rf resonance capacitance sensor. *Sensors and actuators*, 113:133–139, 2004. 16
- N. Kattan, D. Favrat, and J.R.Thome. Flow Boiling in Horizontal Tubes. part 1; Development of a Diabatic Two-Phase Flow Pattern Map. *Journal of Heat Transfer*, Vol. 120, N° 1, pp. 140-147., 120(1):140–147, 1998a. doi: NA. xiii, 9, 18, 34, 35, 38, 39, 41
- N. Kattan, D. Favrat, and J. Thome. Flow Boiling in Horizontal Tubes. part 2; New Heat Transfer Data for Five Refrigerants. *Journal of Heat Transfer*, Vol. 120, N° 1, pp.148-155., 120(1):148–155, 1998b. doi: NA. 18, 38
- J. Keska, M. Smith, and B. Williams. Comparison Study of a Cluster of Four Dynamic Flow Pattern Discrimination Techniques for Multi-phase Flow. *Flow Measurement and Instrumentation*, 10:65–77, 1999. 16, 17
- F. Klein, P. Seleglim, and E. Hervieu. Time-frequency analysis of intermittent two-phase flows in horisontal piping. *Journal of the Brazilian Society of Mechanics Science & Engineering*, XXVI:174–179, 2004. 17, 47, 93
- S. Kline and F. McClintock. Describing uncertainties in single-sample experiments. *Mechanical Engineering*, 75:3–8, 1953. 150
- P. Kosky and F. Staub. Local heat transfer coefficients in the annular flow regime. *AIChE Journal*, 17:1037–1045, 1971. 12
- E. Lemmon. Refprop 7 enthalpy uncertainty. Private e-mail conversation 08-Nov-06, November 2006. 154
- L. Liebenberg. *A Unified Prediction Method for Smooth and Microfin Tube Condensation Performance*. PhD thesis, Rand Afrikaans University, Department of Mechanical Engineering, 2002. 3, 4, 16, 36, 40, 47, 56, 79, 82, 88, 93, 127, 151
- L. Liebenberg, J. Thome, and J. Meyer. Flow Visualization and Flow Pattern Identification with Power Spectral Density Distributions of Pressure Traces during Refrigerant Condensation in Smooth and Micro-Fin Tubes. *Heat Transfer*, 2005. doi: NA. 18

- J. Lienhard and J. Lienhard. *A Heat Transfer Textbook*. Phlogiston Press, 3rd edition, 2005. 8, 83
- J. Mandhane, G. Gregory, and K. Aziz. Flow Pattern Map for Gas-Liquid Flow in Horizontal Pipes. *Int. Journal of Multiphase Flow*, 1:537–553, 1974. ix, 18, 20, 21, 29, 40
- F. U. Manual. *Sensotec*. <http://www.sensotec.com>, Columbus, OH. 79, 154
- Matlab R15. <http://www.mathworks.com>. Mathworks, Reading, MA. 49, 70
- National Institute of Standards and Technology. *NIST Thermodynamic Properties of Refrigerants and Refrigerant Mixtures Database*. ver 7.0, Gaithersburg, MD, 2002. xiii, 7, 8, 71, 154
- National Instruments. *Labview 8 Academic Edition*. Austin, Texas, 2006. 60
- V. Niño, P. Hrnjak, and T. Newell. Characterization of two-phase flow in microchannels. *Air conditioning and refrigeration center*, Project 107:1–97, 2002. ix, 32, 93
- J. Olivier. Pressure Drop during Condensation inside Smooth, Helical Microfin, and Herringbone Microfin tubes. Master's thesis, Rand Afrikaans University, Department of Mechanical Engineering, 2003. 7
- OpenCourseWare. Short-time fourier analysis. OpenCourseWare 2006, November 2006. 50
- R. Revellin, V. Dupont, T. Ursenbacher, J. Thome, and I. Zun. Characterization of diabatic two-phase flows in microchannels: Flow parameter results for r-134a in a 0.5 mm channel. *Int. Journal of Multiphase flow*, 32:755–774, 2006. 15, 94
- R. Sardesai, R. Owen, and D. Pulling. Flow regimes for condensation of a vapour inside a horizontal tube. *Chemical Engineering Science*, 36:1173–1180, 1981. ix, 19, 30, 31, 42
- M. Shah. A General Correlation for Heat Transfer during Film Condensation inside Pipes. *Int. Journal of Heat and Mass Transfer*, 22:547–556, 1979. 19, 89

- H. Soliman. On the Annular-to-Wavy Flow Pattern Transition during Condensation inside Horizontal Tubes. *The Canadian Journal of Chemical Engineering*, 60:475–481, 1982. ix, 18, 25, 27, 41, 126
- H. Soliman and N. Azer. Flow Patterns during Condensation inside a Horizontal Tube. *ASHRAE Transactions*, 1:210–224, 1974. 18
- D. Steiner. *Heat Transfer to Boiling Saturated Liquids*. Verein Deutscher Ingenieure, VDI-Gesellschaft Verfahrenstechnik und Chemieingenieurwesen (GCV), Düsseldorf, 1993. 18, 34
- Y. Taitel and A. Dukler. A model for Predicting Flow Regime Transitions in Horizontal and Near-horizontal gas-liquid flow. *American Institute of Chemical Engineering (AIChE) Journal*, 22:47–55, 1976. 5, 18, 24, 31, 34, 41
- N. Takenaka and H. Asano. Quantitative void fraction measurement method by neutron radiography and application of two-phase flow researches. *Experimental thermal and Fluid science*, 29:393–402, 2005. 17
- T. Tandon, H. Varma, and C. Gupta. A New Flow Regimes Map for Condensation Inside Horizontal Tubes. *Journal Heat Transfer*, 104:763–768, 1982. 18, 41, 126, 140
- Thermal Analysis Partner XPROPS. <http://www.thermalanalysispartners.com>, University of Maryland, MD. 70, 168
- J. Thome. Update on Advances in Flow Pattern Based Two-Phase Heat Transfer Models. *Experimental Thermal and Fluid Science*, 29(3):341–349, 2005. doi: 10.1016/j.exptthermflusci.2004.05.015. 4, 9, 34
- J. Thome and J. E. Hajal. Two-Phase Flow Pattern Map for Evaporation in Horizontal Tubes: Latest Version. *Heat Transfer Engineering*, 24(6):3–10, 2003. 9, 34
- J. Thome, J. El Hajal, and A. Cavallini. Condensation in Horizontal Tubes, Part 2: New Heat Transfer Model Based on Flow Regimes. *Int. Journal Heat Mass Transfer*, 46(18):3365–3387, 2003. doi: 10.1016/S0017-9310(03)00140-6. ix, xii, 4, 11, 12, 18, 19, 39, 89, 90, 133, 134, 168

- J. Tollefsen and E. Hammer. Capacitive sensor design for reducing errors in phase concentration measurements. *Flow Measurement and Instrumentation*, 9:25–32, 1998. 16
- UNEP. Montreal Protocol on Substances that Deplete the Ozone Layer. *United Nations Environmental Program*, Kenya, 2000. 2
- T. Ursenbacher, L. Woljtan, and J. Thome. Dynamic Void Fractions in Stratified Types of Flow, part i: New Optical Measurement Technique. *Int. Journal of Multiphase Flow*, 31, 2004. 15
- C.-C. Wang, C.-S. Chiang, and D.-C. Lu. Visual Observation of Two-Phase Flow Pattern of R-22, R-134a, and R-407c in a 6.5-mm smooth tube. *Experimental Thermal and Fluid Science*, 15:395–405, 1997. 28
- K. Watanabe. Uncertainties in enthalpy for the iapws formulation 1995 for the thermodynamic properties of ordinary water substance for general and scientific use (iapws-95) and the iapws industrial formulation 1997 for the thermodynamic properties of water and steam (iapws-if97). Technical Report 1, The International Association for the Properties of Water and Steam, 2003. 155
- J. Wattlelet, J. Chato, B. Christofferson, J. Gaibel, M. Ponchner, P. Kenney, R. Shimon, T. Villaneuva, N. Rhines, K. Sweeney, D. Allen, and T. Hershberger. Heat transfer flow regimes of refrigerants in a horizontal-tube evaporator. *ACRC Technical Report*, 1994. 21
- J. Weisman, D. Duncan, J. Gibson, and T. Crawford. Effects of fluid properties and pipe diameter on two-phase flow patterns in horizontal lines. *Int. Journal of Multiphase Flow*, 5:437–462, 1979. 5, 16, 18, 20, 21, 28
- Wolverine Tube Inc. *Wolverine Product Brochure*. Wolverine, Hunstville, AL, 1999. 156
- www.engineeringtoolbox.com. <http://www.engineeringtoolbox.com/refrigerants-properties-d-145.html>, 2006. 6, 7

REFERENCES

- O. Zürcher, D. Favrat, and J. Thome. Development of a Diabatic Two-Phase Flow Pattern Map for Horizontal Flow Boiling. *Heat Mass Transfer*, 45:291–303, 2002. doi: NA. 36

Appendix A

Uncertainty analysis

A.1 Introduction

The measuring equipment in experimental facilities provide information describing the system. These devices measures with a bias or drift from the actual condition. This can be controlled but what happens when we do calculation based on these measurements that are never exact. If there is any error in an original reading, this error is carried forward into the equation, which, in turn, introduces error into an otherwise exact equation.

Uncertainty analysis is the process utilized to establish how accurately the measurements are predicting the measured quantities and the calculations based on these quantities. The experiment-specific uncertainties are derived and calculated in the rest of this Appendix.

The test data used in this study is based on averaging. The individual samples are averaged and the uncertainty is based on the average uncertainty of a calibrated device. Thus the uncertainties derived in this section is all for single-sample data based on data measured at the sampling rates and conditions.

A.2 Generalized uncertainty analysis methods

The term *uncertainty* refers to 'a possible value than an error may have' (Kline and McClintock, 1953). The terms *uncertainty* and *uncertainty interval* both

A.2 Generalized uncertainty analysis methods

refer to the interval around a measured value, in which the true value is expected to lie.

The uncertainty of a measurement is typically given in terms of percentages, and is shown as $\delta(\text{measurand})$. If we consider a variable X_1 , its uncertainty would be represented as δX_1 . Uncertainties are also shown, usually, with a confidence level; this value, in terms of percentage, refers to a confidence that X_1 will not deviate by more than δX_1 .

The uncertainty is made up of the Bias, which is a fixed error (B_1), and the Precision (P_1), which can be a random error in the measurement. The uncertainty is calculated as the Euclidian norm of the two.

$$\delta X_1 = \{(B_1)^2 + (P_1)^2\} \quad (\text{A.1})$$

While some researchers deal with Bias and Precision separately (as was done in Coetzee (2000)), others deal with the uncertainty directly. In this case, we will only deal with the uncertainty, except in the rare cases where assumptions are made which necessitate the use of both Bias and Precision.

Let us take a quantity R , function of n variables, X_0 through X_n , each with uncertainty δX_i . So,

$$R = f(X_0, X_1 \dots X_n) \quad (\text{A.2})$$

Then, the effect of the uncertainty of a single variable on quantity R is the partial derivative of R with respect to that single variable (*i.e.* X_i), times that variable's uncertainty (δX_i). That is,

$$\delta R_{X_i} = \frac{\partial}{\partial X_i} (R) \delta X_i \quad (\text{A.3})$$

By summing the uncertainties of R in terms of its variables, the maximum uncertainty is found. It is however unlikely that such a value can be obtained (Liebenberg, 2002), and thus the Euclidian norm of the individual uncertainties is taken.

$$\delta R = \left\{ \sum_{i=1}^n \left(\frac{\partial}{\partial X_i} (R) \delta X_i \right)^2 \right\}^{\frac{1}{2}} \quad (\text{A.4})$$

A.3 Uncertainty in temperature measurements

This equation is valid only when:

- The errors and uncertainties of each variable are independent of one another
- The distribution of errors or uncertainties is Gaussian, for all X_i
- All the X_i s are quoted at the same odds.

It is customary to normalize Equation A.4 with respect to the full value of R , with percentage units.

A.3 Uncertainty in temperature measurements

Temperatures in this experimental system are measured using type-T thermocouples. Type-T thermocouples use constantin and copper as the two metals. The cold junction utilized is built-in into National Instruments' SCXI-1303 card. The thermocouples are calibrated in two temperature baths, one at 5°C and the other at 60°C, against a Pt-100 resistance temperature detector (RTD).

The temperatures were calibrated using a linear scale. As they were calibrated using a precise RTD, the thermocouples' Bias was taken to be that of the Pt-100 RTD used. Furthermore, the precision of each thermocouple measurement is known to be the standard deviation from the steady-state value it measures. Then, the uncertainty in each thermocouple's reading is

$$\delta T_i = \sqrt{B^2 + P^2} \quad (\text{A.5})$$

where the precision P is directly equal to the standard deviation of the reading, σ . There are several sections of the experimental set-up that utilizes the average of several thermocouples (up to four) to find the mean temperature. It follows that

$$T_m = \frac{T_1 + T_2 + \dots + T_n}{n} \quad (\text{A.6})$$

And, the partial differential in this mean temperature per averaged temperature is

A.4 Refrigerant mass flow rate uncertainty

$$\frac{\partial T_{m,T_i}}{\partial T_i} = \frac{1}{n} \delta T_i \quad (\text{A.7})$$

Taking the Euclidian norm, and assuming that the thermocouples have the same uncertainty,

$$\begin{aligned} \delta T_m &= \left\{ \sum_{i=1}^n \left(\frac{1}{n} \delta T_i \right)^2 \right\}^{\frac{1}{2}} = \left(\frac{n}{n^2} \delta T_i^2 \right)^{\frac{1}{2}} \\ &= \left(\frac{1}{n} \right)^{\frac{1}{2}} \delta T_i \end{aligned} \quad (\text{A.8})$$

A.4 Refrigerant mass flow rate uncertainty

The Coriolis flow meters have an accuracy of 0.1% of the nominal reading. Thus, the uncertainty in the Coriolis CMF-010 is

$$\delta \dot{m} = \frac{0.1}{100} \dot{m}_{reading} \quad (\text{A.9})$$

A.4.1 Mass flux uncertainty

The mass flux is defined as

$$G = \frac{\dot{m}}{A_c} \quad (\text{A.10})$$

From the uncertainty of cross-sectional area, and that of the flow rate,

$$\delta G = \left(\left(\frac{\partial}{\partial \dot{m}} G \delta \dot{m} \right)^2 + \left(\frac{\partial}{\partial A_c} G \delta A_c \right)^2 \right)^{\frac{1}{2}} \quad (\text{A.11})$$

and the partial differentials are

$$\frac{\partial G}{\partial \dot{m}} = \frac{1}{A_c} \quad (\text{A.12})$$

$$\frac{\partial G}{\partial A_c} = -\frac{\dot{m}}{A_c^2} \quad (\text{A.13})$$

A.5 Water mass flow rates uncertainty

The Coriolis flow meters have an uncertainty of 0.1% of the actual reading, when in the nominal flow regime. Thus, the uncertainty in the Coriolis CMF-010 and the CMF-025 is

$$\delta\dot{m} = \frac{0.1}{100}\dot{m}_{reading} \quad (\text{A.14})$$

The Bürkert flow meters, models *DIN*–015 and *DIN*–025, have an uncertainty of 0.2% of the full scale reading. Then, the uncertainty is

$$\delta\dot{m} = \frac{0.2}{100}\dot{m}_{reading} \quad (\text{A.15})$$

A.6 Pressure measurement uncertainty

The pressure transducers, Sensotec FP-2000s (Manual, Columbus, OH), with a full-scale value of 500 psi (± 3447 kPa) have an uncertainty of 0.1% of full-scale. This gives

$$\delta P_j = \pm \frac{0.1}{100} 3447 \quad (\text{A.16})$$

$$= \text{reading} \pm 3.447 \text{ kPa} \quad (\text{A.17})$$

A.7 REFPROP uncertainty analysis

National Institute of Standards and Technology (2002)'s REFPROP uses user inputs of pressure and temperature to calculate the correct property. The main thermo-physical properties of the fluid in question, the average uncertainties in terms of percentages, are available in the `texttt.fld` fluid files in the Refprop directory. However, for such properties as enthalpy and entropy, it is not possible to directly garner the uncertainty from the fluid files. This is due to the fact that these are calculated using the governing equation of state. However, the governing equations are complicated, and it is time-consuming to properly calculate the required derivatives. Lemmon (2006) in a private e-mail communication with the

A.7 REFPROP uncertainty analysis

author states that the accepted practice is to take the uncertainty of the enthalpy as half of that of the isobaric specific heat.

Thus, from the REFPROP fluid files, and the private conversation held with Dr. Lemmon, the following typical uncertainties are found.

$$\delta h = 0.375\% \quad (\text{A.18})$$

$$\delta k_{l,v} = 5\% \quad (\text{A.19})$$

$$\delta \mu_l = 3\% \quad (\text{A.20})$$

$$\delta \mu_v = 4\% \quad (\text{A.21})$$

$$\delta \rho_l = 0.05\% \quad (\text{A.22})$$

$$\delta \rho_v = 0.05\% \quad (\text{A.23})$$

$$\delta \sigma = 0.05\% \quad (\text{A.24})$$

$$\delta c_p = 0.75\% \quad (\text{A.25})$$

The water side uncertainties are found in the water fluid file from REFPROP and the IAPWS Advisory Note (Watanabe, 2003) regarding uncertainties of enthalpy, thermal conductivity and surface tension. The uncertainties are summarized as

$$\delta h = 0.05\% \quad (\text{A.26})$$

$$\delta k_{l,v} = 0.001\% \quad (\text{A.27})$$

$$\delta \mu_l = 0.5\% \quad (\text{A.28})$$

$$\delta \mu_v = 0.5\% \quad (\text{A.29})$$

$$\delta \rho_l = 0.001\% \quad (\text{A.30})$$

$$\delta \rho_v = 0.001\% \quad (\text{A.31})$$

$$\delta \sigma = 0.1\% \quad (\text{A.32})$$

$$\delta c_p = 0.1\% \quad (\text{A.33})$$

A.8 Temperature difference uncertainty

The temperature difference between inlet and outlet of any of the heat exchangers is a function, evidently, of the inlet and outlet temperatures. Each temperature has its own uncertainty (though, because of prior calibration, and method of manufacturing, which is the same, for correctly working thermocouples, the uncertainty should be of the same order, at the least), and taking a difference will only increase the uncertainty. Thus, for a generic temperature difference, the uncertainty is

$$\delta\Delta T = (\delta T_1^2 + \delta T_2^2)^{\frac{1}{2}} \quad (\text{A.34})$$

A.9 Uncertainty in measurement of tube diameters

The inside tube diameters were measured by the manufacturers Wolverine Tube Inc. (1999) to a total uncertainty of $25 \cdot 10^{-6}m$, that is $\delta D_i = 25 \cdot 10^{-6}m$.

A.10 Uncertainty in measurement of heat exchanger length

The precision limit was taken as twice the smallest increment of the tape measure, *i.e.* 0.5 mm, and a bias limit of 1 mm was assumed. Thus, the uncertainty in the measurement of the exchanger length is

$$\delta L = \sqrt{1^2 + 0.5^2} = 1.11 \text{ mm} \quad (\text{A.35})$$

This gives an uncertainty of $\delta L = 1.11 \text{ mm}$.

A.11 Uncertainty in measurement of surface area

The tube surface area is calculated from

A.12 Uncertainty in the value of thermal conductivity of the copper tubing

$$A_i = \pi D_i L, \quad A_o = \pi D_o L \quad (\text{A.36})$$

Then, the uncertainty in A is

$$\delta A = \left[\left(\frac{\partial}{\partial L} A \delta L \right)^2 + \left(\frac{\partial}{\partial D_i} A \delta D_i \right)^2 \right]^{\frac{1}{2}} \quad (\text{A.37})$$

The partial differentials are

$$\frac{\partial A}{\partial L} = \pi D_i \quad (\text{A.38})$$

$$\frac{\partial A}{\partial D_i} = \pi l \quad (\text{A.39})$$

A.12 Uncertainty in the value of thermal conductivity of the copper tubing

Abu-Eishah (2001) performed a detailed analysis of the uncertainty of the copper tube thermal conductivity. He found the total uncertainty in the conductivity to be,

$$\frac{\delta k_{Cu}}{k_{Cu}} \cdot 100 = \frac{4}{400} \cdot 100 = 0.01\% \quad (\text{A.40})$$

in the temperature region of this study (*i.e.* 0-100°C).

A.13 Heat balance, Refrigerant side

The heat transferred from the refrigerant is calculated by multiplying the refrigerant mass flux by the change in enthalpy (from inlet of precondenser to the outlet of the postcondenser). This is

$$\dot{Q}_{ref} = \dot{m}_{ref} \Delta h \quad (\text{A.41})$$

And the uncertainty is

A.14 Heat balance uncertainty, water side

$$\delta\dot{Q}_{ref} = \left(\left[\frac{\partial}{\partial \dot{m}}(\dot{Q})\delta\dot{m} \right]^2 + \left[\frac{\partial}{\partial \Delta h}(\dot{Q})\delta\Delta h \right]^2 \right)^{\frac{1}{2}} \quad (\text{A.42})$$

where,

$$\delta\Delta h = \left(\left(\frac{\partial}{\partial h_{in}}\Delta h\delta h_{in} \right)^2 + \left(\frac{\partial}{\partial h_{out}}\Delta h\delta h_{out} \right)^2 \right)^{\frac{1}{2}} \quad (\text{A.43})$$

A.14 Heat balance uncertainty, water side

The water side heat transferred is,

$$\dot{Q}_{water} = \sum \dot{Q}_{i,H_2O} \quad (\text{A.44})$$

Where the total heat transferred from the water is equal to the sum of the individual heat exchangers' water side heat balance. This entails that the uncertainty in the water side of the heat balance is

$$\delta\dot{Q}_{H_2O} = \left(\sum_{i=1}^3 \left(\frac{\partial}{\partial \dot{Q}_i}\dot{Q}_{H_2O}(\delta\dot{Q}_i) \right)^2 \right)^{\frac{1}{2}} \quad (\text{A.45})$$

The individual heat exchangers' water side heat balance uncertainty can be calculated using

$$\dot{Q}_i = \dot{m}_{H_2O,i}c_{p,i}\Delta T_i \quad (\text{A.46})$$

Thus, the uncertainty in the water-side energy transfer, knowing what the uncertainties in the water mass flow rate, isobaric specific heat and temperature difference, are

$$\delta\dot{Q}_i = \left[\left(\frac{\partial}{\partial \dot{m}}\dot{Q}_i\delta\dot{m} \right)^2 + \left(\frac{\partial}{\partial c_{p,i}}\dot{Q}_i\delta c_{p,i} \right)^2 + \left(\frac{\partial}{\partial \Delta T_i}\dot{Q}_i\delta\Delta T_i \right)^2 \right]^{\frac{1}{2}} \quad (\text{A.47})$$

A.15 Average heat transfer uncertainty

The average heat transferred, \dot{Q}_{avg} is

$$\dot{Q}_{avg} = \frac{\dot{Q}_{H_2O} + \dot{Q}_{ref}}{2} \quad (A.48)$$

Then, the uncertainty in the average heat transfer is

$$\delta\dot{Q}_{avg} = \left(\frac{1}{2}\right)^{\frac{1}{2}} \left[\delta\dot{Q}_{h_2O}^2 + \delta\dot{Q}_{ref}^2 \right]^{\frac{1}{2}} \quad (A.49)$$

A.16 Log mean temperature difference uncertainty analysis

The log mean temperature difference is

$$\Delta T_{LMTD} = \frac{(T_{w,in} - T_{r,sat}) - (T_{w,out} - T_{r,sat})}{\ln \frac{T_{w,in} - T_{r,sat}}{T_{w,out} - T_{r,sat}}} \quad (A.50)$$

We can define it as

$$\Delta T_{LMTD} = \frac{\Delta T_2 - \Delta T_1}{\ln \frac{\Delta T_2}{\Delta T_1}} \quad (A.51)$$

where $\Delta T_2 = T_{w,in} - T_{r,sat,out}$ and $\Delta T_1 = T_{w,out} - T_{r,sat,in}$.

The uncertainty in terms of the two temperature differences is

$$\delta\Delta T_{LMTD} = \left[\left(\frac{\partial}{\partial\Delta T_1} (\Delta T_{LMTD}) \delta\Delta T_1 \right)^2 + \left(\frac{\partial}{\partial\Delta T_2} (\Delta T_{LMTD}) \delta\Delta T_2 \right)^2 \right]^{\frac{1}{2}} \quad (A.52)$$

where

$$\frac{\partial\Delta T_{LMTD}}{\partial\Delta T_2} = \frac{1}{\ln \frac{\Delta T_2}{\Delta T_1}} - \frac{\Delta T_2 - \Delta T_1}{\left(\ln \frac{\Delta T_2}{\Delta T_1} \right)^2 \Delta T_2} \quad (A.53)$$

$$\frac{\partial\Delta T_{LMTD}}{\partial\Delta T_1} = \frac{1}{\ln \frac{\Delta T_2}{\Delta T_1}} - \frac{\Delta T_2 - \Delta T_1}{\left(\ln \frac{\Delta T_2}{\Delta T_1} \right)^2 \Delta T_1} \quad (A.54)$$

A.17 Inlet and outlet vapor quality uncertainty analysis

A.17.1 Inlet vapor quality uncertainty

The vapor quality at the inlet and outlet of the test section is calculated using measured data, including temperature, pressure and water-side heat transferred. This means, though that the inlet and outlet enthalpies are calculated. And,

$$h_{in,test} = h_{in,pre} - \left| \frac{\dot{Q}_{pre,H_2O}}{\dot{m}_{ref}} \right| \quad (A.55)$$

Thus, the uncertainty in test inlet enthalpy is

$$\delta h_{in,test} = \left[\left(\frac{\partial}{\partial \dot{Q}_{pre,H_2O}} (h_{in,test}) \delta \dot{Q}_{pre,H_2O} \right)^2 + \left(\frac{\partial}{\partial \dot{m}_{ref}} (h_{in,test}) \delta \dot{m}_{ref} \right)^2 + \left(\frac{\partial}{\partial h_{in,pre}} (h_{in,test}) \delta h_{in,pre} \right)^2 \right]^{\frac{1}{2}} \quad (A.56)$$

where the partial differentials above are,

$$\frac{\partial h_{in,test}}{\partial h_{in,pre}} = 1 \quad (A.57)$$

$$\frac{\partial h_{in,test}}{\partial \dot{Q}_{pre,H_2O}} = -\frac{1}{\dot{m}_{ref}} \quad (A.58)$$

$$\frac{\partial h_{in,test}}{\partial \dot{m}_{ref}} = \frac{\dot{Q}_{H_2O}}{\dot{m}_{ref}^2} \quad (A.59)$$

Then, knowing what the enthalpy at the point is, the quality can be calculated as

$$x_{in} = \frac{h_{in,test} - h_f}{h_v - h_l} \quad (A.60)$$

And from the above, the uncertainty in x_{in}

A.18 Overall heat transfer coefficient uncertainty analysis

$$\delta x_{in} = \left[\left(\frac{\partial}{\partial h_{in,test}}(x_{in})\delta h_{in,test} \right)^2 + \left(\frac{\partial}{\partial h_{f,test}}(x_{in})\delta h_{f,test} \right)^2 + \left(\frac{\partial}{\partial h_{v,test}}(x_{in})\delta h_{v,test} \right)^2 \right]^{\frac{1}{2}} \quad (A.61)$$

The partial differentials are

$$\frac{\partial x_{in}}{\partial h_{in,test}} = \frac{1}{h_{v,test} - h_{l,test}} \quad (A.62)$$

$$\frac{\partial x_{in}}{\partial h_{v,test}} = \frac{h_f - h_{in,test}}{(h_v - h_f)^2} \quad (A.63)$$

$$\frac{\partial x_{in}}{\partial h_{f,test}} = -\frac{1}{h_{v,test} - h_{f,test}} - \frac{h_{in,test} - h_{f,test}}{(h_{v,test} - h_{f,test})^2} \quad (A.64)$$

Where h_l and h_v are evaluated at the saturation pressure and temperature measured at the inlet of the test section, and are functions of REFPROP.

A.18 Overall heat transfer coefficient uncertainty analysis

The overall heat transfer coefficient is given as

$$UA = \frac{\dot{Q}_{avg}}{\Delta T_{LMTD}} \quad (A.65)$$

The uncertainty is

$$\delta UA = \left[\left(\frac{\partial}{\partial \dot{Q}_{avg}}(UA)\delta \dot{Q}_{avg} \right)^2 + \left(\frac{\partial}{\partial \Delta T_{LMTD}}(UA)\delta T_{LMTD} \right)^2 \right]^{\frac{1}{2}} \quad (A.66)$$

The partial differentials of the overall heat transfer coefficient with respect to the average heat transferred and the log mean temperature difference are

$$\frac{\partial UA}{\partial \dot{Q}_{avg}} = \frac{1}{\Delta T_{LMTD}} \quad (A.67)$$

A.19 Inner tube heat transfer coefficient

$$\frac{\partial UA}{\partial \Delta T_{LMTD}} = -\frac{\dot{Q}_{avg}}{\Delta T_{LMTD}^2} \quad (A.68)$$

A.19 Inner tube heat transfer coefficient

The overall heat transfer coefficient is

$$\frac{1}{UA} = \frac{1}{h_o A_o} + R_w + \frac{1}{h_i A_i} \quad (A.69)$$

Rearranging,

$$h_i = \frac{1}{A_i} \left(\frac{1}{UA} - \frac{1}{h_o A_o} - R_w \right)^{-1} \quad (A.70)$$

A.20 Frequency detection via high-speed camera

As validation that frequencies can be detected in a light source and therefore in the variation of light passing through flows that deflect light, a stroboscope was used. The stroboscope was set to emit a fixed frequency of light and a short recording was made of the light source. The frequencies detected by means of and FFT correspond well with the frequency of the light source (Figure A.1).

A.21 Uncertainty Results

The above equations were coded into a Matlab program that automatically calculated the uncertainties for all the data points during operation of the system. The uncertainties are summarized in Table A.1 and discussed thereafter.

The uncertainties presented here are representative of the extreme corners of the test matrix (Chapter 5). During the analysis of the data, it was found that the uncertainties varied, on both constant vapor quality and mass flux, between the boundary values presented in Table A.1.

Due to the fact that the inlets and outlets of the test section were instrumented using several thermocouples (three thermocouples were used to find the mean

A.21 Uncertainty Results

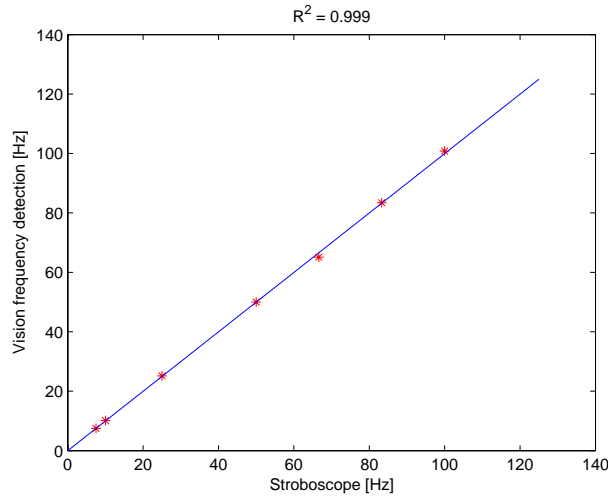


Figure A.1: Comparison of frequencies detected and emitted

Table A.1: Experimental uncertainties for condensation heat transfer

	Measurand Uncertainty (%)			
	G-250 – x-65%	G-250 – x-11%	G-650 – x-56%	G-650 – x-12%
$\delta T_{ref,m}$	0.0178°C	0.0208°C	0.0727°C	0.0117°C
$\delta P_{test,m}$	0.1314%	0.1351%	0.1424%	0.1316%
$\delta \dot{m}_{ref}$	0.1%	0.1%	0.1%	0.1%
δx_{in}	1.524%	4.661%	2.378%	8.238%
$\delta \epsilon_{in}$	0.061%	0.4386%	0.1191%	0.5710%
$\delta \Delta P_{f,L}$	60.43%	72.02%	38.47%	81.78%
$\delta h_{c,exp}$	0.2087%	3.2672%	0.5484%	4.023%

temperatures), the uncertainty in the saturation temperature was quite precise, nearing that of a high-precision Pt-100 RTD ($\pm 0.01^\circ\text{C}$).

The saturation pressure was also measured using the average of three gauge pressure transducers, which resulted in very certain saturation pressure readings. Although these transducers are normally rated as 0.1% accurate, this is relative

A.21 Uncertainty Results

to their full-scale value; averaging the readings of six of these transducers brought the uncertainty of the average saturation pressure back to a value near that of a single transducer reading a full-scale measurement. The uncertainty remained essentially constant over the entire test matrix.

Since the refrigerant mass flow was measured using a Micromotion CMF-010 flow meter (with MVD technology), it had a constant uncertainty of 0.1% over the entire mass flow range that was tested in this setup. The mass flow's uncertainty is not a constant once the flow drops to a mass flow of about 0.001 kg/s (these low flows were not reached in this experiment). The uncertainty remained constant over the test matrix.

The pressure drop over the test section was measured using two sets of absolute gauge pressure transducers (average of three signals each). The total pressure drop over the entire test range varied between 2 kPa at the lowest mass fluxes and vapor qualities and 12 kPa at the highest mass fluxes and vapor qualities. The uncertainties in pressure drop makes it clear that although gauge pressure transducers are necessary at the inlet and outlet of the test section to calculate thermal properties, an additional differential pressure transducer must be utilized for accurate pressure drop measurements. It is clear from these results that to obtain reasonable uncertainty in the pressure drop results in this system, at least one differential pressure transducer, instrumented between the inlet and outlet of the test section, is required.

The heat transfer coefficient uncertainty results are also tabulated in Table A.1. The maximum deviation that is found is on the order of 4%, with the best uncertainties on the order of about 0.2%. The highest uncertainties occur at lower vapor qualities, irrespective of mass flux; the fluctuations seen in Table A.1 are due to the fact that the qualities are not exactly the same. If a direct comparison could be made, it would be most probable that the uncertainties found at a constant quality, with varying mass flux (within limits of the flow meter and with a good enough temperature drop on the water side of the test heat exchanger) would compare well. This is evidenced in the case of the low vapor quality data, in which the vapor quality is almost the same.

A.22 Conclusion

The uncertainties presented here only serve to quantify the quality of data captured. For a complete and in-depth discussion of two-phase flow uncertainties including aspects of vapor quality, void fraction model, momentum pressure drop and heat transfer refer to Christians-Lupi (2007).

The uncertainties presented are only for the outlying corners of the test matrix but the uncertainty for every point is calculated and recorded. It was found to be within the limits presented here.

The recommendation for future work with the existing test setup based on uncertainty would be the use a differential pressure transducer over the test section. Higher accuracy can be achieved by averaging more thermocouples per location (limited by the availability of channels) and most importantly to calibrate all measuring equipment.

Appendix B

Programs

B.1 Main system control

The program written to control the system and all the activities surrounding operation and testing consists of a complex network of sections and subprograms. In this section the program and its main layout will be discussed.

The diagram represents the flow of information through the program (Figure B.1). The control inputs are given to the data acquisition system (DAQ) to send signals to the equipment for controlling the system. These signal can be identified as write tasks in the program. The measured parameters are collected from the DAQ by means of read tasks. These measured parameters include mass flows, pressures temperatures and void fraction.

The measurement devices have all been calibrated and the calibration adjustments are applied at different locations. The temperatures are calibrated in the program by linear functions calibrated against a Pt-100 (Chapter 3). There are also uncalibrated temperatures for the non-essential system properties. The pressure transducer calibration is applied in the DAQ program and by means of the ratio metric program. The mass flows are calibrated on the transmitters of the flow meter or in the program by means of an adjustment function defined by calibration against an accurate flow meter. The sequence of devices must be retained for the calibration to be applied to the correct measurement. The temperature measurements at locations where multiple thermocouples are used, are averaged in subprograms as final preparation for the calculation program.

B.1 Main system control

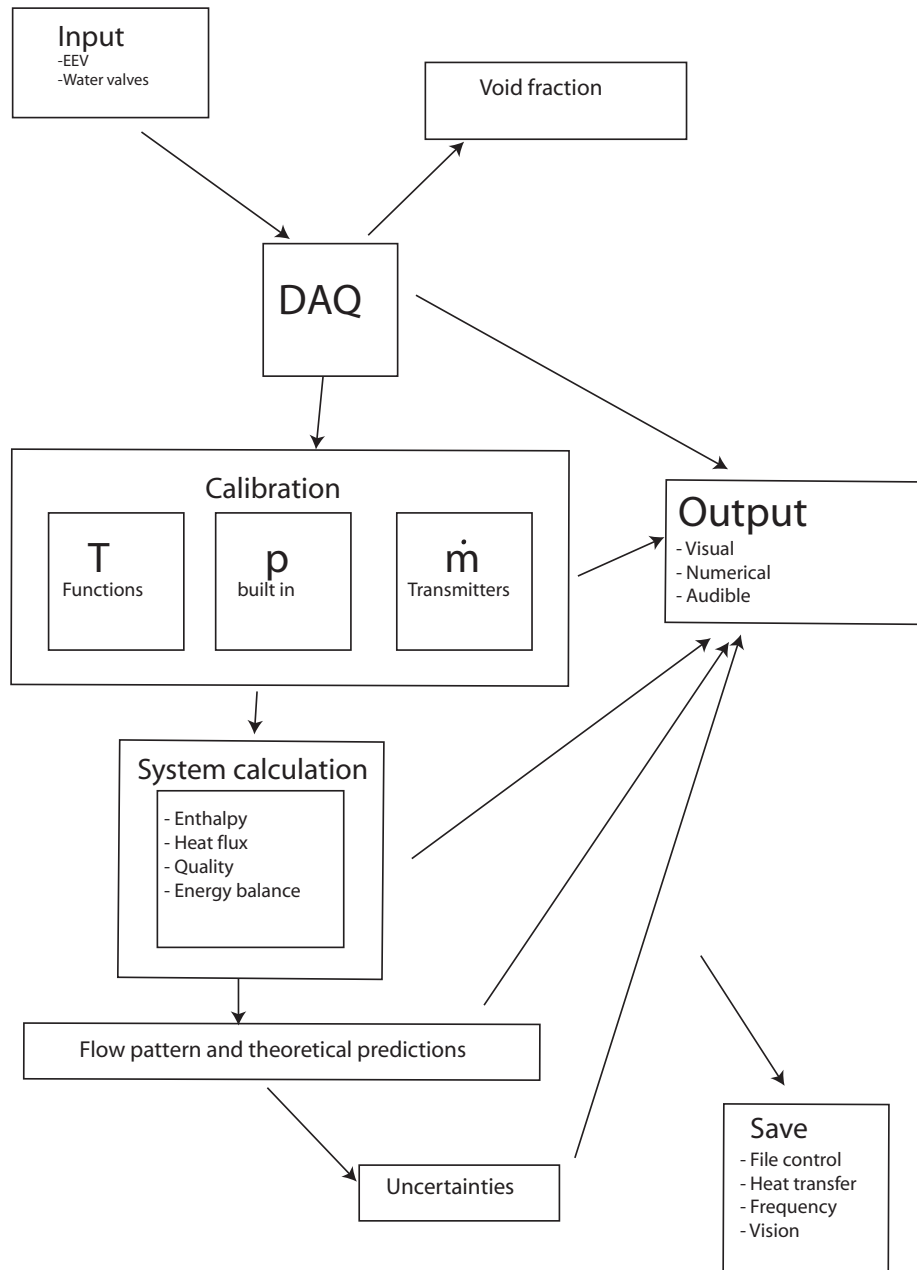


Figure B.1: Diagram of the processes during every cycle of the control program

B.1 Main system control

The error conditions of the measured quantities are checked for the safety of the system and operating condition. This involves checking pressures and temperature at the inlet and outlet of the compressor and heat exchangers. The compressor must be kept within normal operating conditions to prevent thermal overload or the intake of liquid. The heat exchangers are checked for sub-zero temperatures to prevent the freezing of water and subsequent blocking of flow. The mass fluxes through the Coriolis flow meters are monitored to be within the minimum for accuracy purposes and the Bürkert flow meters are checked for blockage. If the software protection fails, a set of hardware safeties is installed to trip the system in case of emergency.

The measured raw data are then fed to a Matlab code for more advanced calculations. This section of the code calculates the general condition of the system and all the properties in the cycle. The property calculations are performed using Xprops Matlab functions of that in turn reference the REFPROP database (Thermal Analysis Partner XPROPS, University of Maryland, MD). This section of Matlab code calculates enthalpies based on temperatures and pressures in the system. The heat fluxes over all the heat exchangers are then calculated and subsequently the energy balance error is calculated. The other calculated properties are treated as predictions until the energy balance error over the entire condensing section is less than 1%. The procedure of calculating properties and predicting saturation conditions is documented in Chapter 3.

The second major calculation intensive subprogram is responsible for the flow pattern prediction based on the El Hajal *et al.* (2003) flow pattern map. The theoretical heat transfer and pressure drop predictions based on the Thome *et al.* (2003) correlations are calculated in this program.

A subprogram with Matlab-coded uncertainty equations, based on the discussion in Appendix A, and the uncertainty analysis done in Christians-Lupi (2007) can be deactivated when not needed. The input for this subprogram is based on the statistical analysis of the measured and calculated properties and takes into account the full propagation of experimental uncertainties by all the function variables. The statistical analysis of measured variables includes sampling the latest 30 to 50 data points and calculating a mean, standard deviation and percentage deviation.

B.2 LabView videos capture program

All the functions mentioned are responsible for calculation of the system condition. The data are then combined and real time feedback is presented on the front panel to the user. The front panel is filled with digital outputs of the variables. The important properties that can be gauged on analogue indicators, like pressure, are easily visible. The error check activates a visible light on the front panel and in critical cases an audible warning is given to alert the operator. The history of some variables like heat flux, mass flux and energy balance is presented on the control panel to gauge the effectiveness of control inputs and the stability of the system. The user then makes decisions and adjustments to the system based on the feedback until a test point is reached. When a test point is reached the statistics and uncertainty will indicate if the system is stable and if testing can commence. The statistics and uncertainties are provided on separate tabs on the front panel of the program.

When a test is initialised the program keeps on running and executing all functions in the normal operational loop. The calculations are performed and saved with raw data in a file for as long as a test is set to continue. The saving of data is executed in two steps. The system data are saved as mentioned above for heat transfer and pressure drop analysis. The program then stops for the second step, a timed capture of data for frequency analysis. Since the test point is stable over the time of data capturing the data for the first step is valid for the second step. The test is aborted if for any reason the test conditions change during a test and the user has to wait for stable conditions to resume.

B.2 LabView videos capture program

The capture of videos and control of the camera is done using LabView and the Vision Assistant toolbox. The program can function independently or as a subprogram in any control program (Figure B.2).

The first step in this program is the file control for the video sequence. This creates a path to the hard drive location of the video. The camera settings can also be adjusted here. The brightness, gain, shutter speed, image size, buffer size, capture mode, image type, frame rate, video mode, time out, trigger, trigger mode and *.avi* save format must be set. This excludes other control functions not

used for this type of capture. The LabView and Vision environment use IMAQ, Vision Assistant and IEEE-1394a subprograms and protocols in unison.

The program then opens buffers in the memory of the computer to save the images while the capture is in progress and the data waits to be saved.

A trigger or timing function is then set up to control the speed for the capture. This determines how many frames will be captured per second. The frames are then captured in a timed loop that executes for the number of frames selected. The images are then saved in an *.avi* video sequence and the memory is cleared.

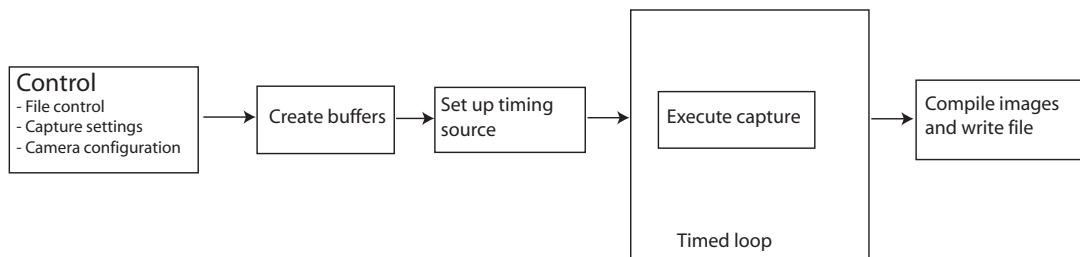


Figure B.2: Diagram with the sequence of events during a video capture

B.3 Video analysis

The video analysis program begins by reading the video file and the accompanying information about the image size, data type, number of images and other configuration settings that assists in the playback mode (Figure B.3). A region of interest can be defined by specifying the coordinates on the image. Each pixel has a coordinate (x,y) starting at (0,0) in the top left hand corner. A line can also be used as inspection zone. The video sequence is then recalled and each image is measured and the data are stored in an array. The time component is then calculated based on the timing specified when the capture was made. All sequences for frequency analysis were captured at 250 frames per second.

When the file reading is finished the program enters a loop where the analysis is carried out. The statistical and frequency domain analysis is executed in LabView. The same analyses were performed in Matlab to verify the output because LabView is not a powerful analysis tool and the algorithms are not optimised.

B.3 Video analysis

LabView was however used because of the simple user interface that was required for the analysis. The statistical data included a probability density function, cumulative density function and a histogram of the signal. The frequency analysis included a fast Fourier transform, power spectral density, peak detection and a time-frequency output.

The time-frequency analysis was used for the time-fraction prediction. The data can be analysed manually by inspecting the frequency content at different times. The semi-automated method was used in this case by selecting an inspection frequency and then adjusting the limits according to the energy content of the signal.

The raw signal data were saved together with the time-fractional results as final output of the program.

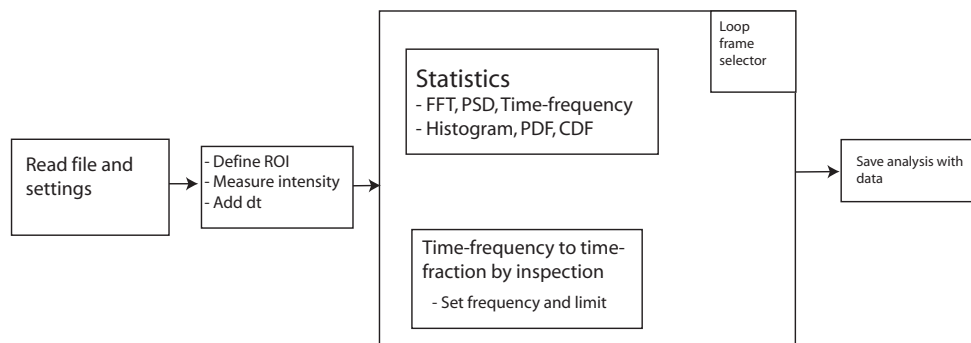


Figure B.3: Diagram of the sequence of programming during a video analysis run

Appendix C

Raw data